NASA CR-66787

UNSTEADY AIRFOIL STALL

By Lars E. Ericsson and J. Peter Reding

July 1969

Prepared under Contract NAS 1-7999 by
Lockheed Missiles & Space Company
Sunnyvale, California

for

NATIONAL AERONAUTICS AND SPACE ADMINISTRATION

JUL 1969 LMSC N-1F-69-1

UNSTEADY AIRFOIL STALL

FINAL REPORT

Prepared by

LARS E. ERICSSON
Senior Staff Engineer, Engineering Technology
and
J. PETER REDING
Research Specialist, Aero-Thermodynamics

Prepared under Contract NAS 1-7999

Lockheed

MISSILES & SPACE COMPANY
A GROUP DIVISION OF LOCKHEED AIRCRAFT CORPORATION
SUNNYVALE, CALIFORNIA

UNSTEADY AIRFOIL STALL

By Lars E. Ericsson and J. Peter Reding

July 1969

Prepared under Contract NAS 1-7999 by
Lockheed Missiles & Space Company
Sunnyvale, California

for

NATIONAL AERONAUTICS AND SPACE ADMINISTRATION

NASA CR-66787

UNSTEADY AIRFOIL STALL

By Lars E. Ericsson and J. Peter Reding

July 1969

Prepared under Contract NAS 1-7999 by
Lockheed Missiles & Space Company
Sunnyvale, California

for

NATIONAL AERONAUTICS AND SPACE ADMINISTRATION

ABSTRACT

An exploratory study has been made of the unsteady airfoil stall characteristics at low subsonic speeds. It is found that the adverse dynamic effects observed at airfoil oscillations through stall can be explained using quasi-steady separated flow concepts in which the time history is represented by one discrete past time event. Also the classical von Karman-Sears treatment below stall is found to be well approximated by this time-lagged quasi-steady theory permitting a unified treatment of the oscillatory airfoil characteristics at all angles-of-attack. The developed analytic theory can use static experimental data as an input, and the predictions made in this manner are found to agree well with experimental dynamic data and explains the so-called stall buffet problem. It is outlined how the analytic foundations made in this exploratory study can be used to formulate a theory that will account for all the facets of the unsteady airfoil stall problem.

SUMMARY

An exploratory study of unsteady airfoil stall at low subsonic speeds has revealed that the adverse dynamic characteristics can be explained using Quasi-Steady Theory in which time history effects are lumped into one discrete past time event. The dominant characteristic of dynamic stall is the accelerating flow on the leeward side of a pitching airfoil, delaying the adversity of the pressure gradient, thereby causing a delay of the stall. Pitch rate induced camber and vortex shedding are other characteristics that become important, especially at high oscillatory frequencies. The developed analytic theory can use static experimental data as an input. The problem is to define what static data to use.

CONTENTS

ILLUSTRATIONS

Section 1
INTRODUCTION

Unsteady airfoil stall is an old problem that recently has received renewed attention by the compressor and helicopter industry. Because of distortions in the circumferential velocity distribution, a compressor blade traveling at constant rotational speed will experience a periodic change in angle of attack, that on a high performance compressor will cause blade stall (Ref. 1). The periodic variation of blade angle of attack on a helicopter is caused by the difference in horizontal local velocity between an advancing and a receding blade of a helicopter in a forward flight (Ref. 2). It is well documented experimentally that dynamic instability results when the airfoil penetrates into the stall region (Refs. 3 and 4). The resulting stall flutter problems for helicopters have been enumerated recently (Ref. 5). Thus it is of great practical interest to be able to understand and predict unsteady airfoil stall characteristics. This is particularly so in view of the fact that even dynamically scaled model tests may not be applicable to full scale due to the problem of wind tunnel and support interference, and the sensitivity of airfoil stall to surface roughness, flow uniformity, Reynolds number, and air turbulence. Only if the unsteady stall mechanism is understood can an "analytic extrapolation" to full scale be made with confidence.

It is clear that neither theory nor experiments alone will provide a satisfactory solution. However, if the unsteady aerodynamics can be related theoretically to static aerodynamic characteristics which are readily available for a great number of airfoil shapes, a very substantial advancement of the state of the art will be accomplished. This has been attempted before without outstanding success. The present approach rests heavily on previously developed unsteady flow concepts for separated flow on launch vehicles (Ref. 6) and reentry bodies (Ref. 7). A conceptual flow picture is constructed and analytic relationships between dynamic and static characteristics are developed using quasi-steady separated flow theory in which time history effects are lumped to one discrete past time event.

Section 2
DISCUSSION

Airfoil stall is a complicated flow problem because it is sensitive to so many geometric and aerodynamic parameters. This is true already in stationary flow, and the difficulties are, of course, amplified in unsteady flow. Static stall data will be examined first, and the dynamic stall data will then be put in proper relation to the static data. Only low speed data for which compressibility effects are negligible ($M \leq 0.4$) will be discussed.

2.1 STATIC STALL

The "three representative types of airfoil-section stall" discussed in 1951 by McCullough and Gault (Ref. 8 and Fig. 1) are still basic. However, the interaction between the laminar separation bubble and the trailing edge separation, which was only mentioned as an interesting possibility in Ref. 8, is becoming of more practical concern if one wants to understand unsteady airfoil stall. Carrow (Ref. 9) has taken a closer look at these possibilities. Figure 2a shows how a 10% thick airfoil at a Reynolds number of $R_c = 6 \times 10^6$ has a short laminar bubble with turbulent reattachment if the surface is smooth, but turbulent trailing edge separation if distributed (so called standard) roughness at the leading edge is used. The loss in lift is due to the artifically thickened boundary layer. On a thin (6%) airfoil, however, leading edge roughness will actually increase $c_{l_{max}}$ as the separation changes from a long laminar bubble with transitional reattachment to turbulent trailing edge separation (Fig. 2b). This switch to turbulent separation occurs naturally (on the smooth airfoil) when R_c exceeds 9×10^6 (Ref. 10) and on NACA 64A006 when $R_c > 5.8 \times 10^6$ (Ref. 11).

The change from short bubble to turbulent separation (Fig. 2a) occurs naturally at $R > 15 \times 10^6$ on a NACA-0009 airfoil (Ref. 10) or at effective* Reynolds numbers

*Including effect of tunnel turbulence, $R_{eff} = K \cdot R_c$ where $K > 1$ (Ref. 12).

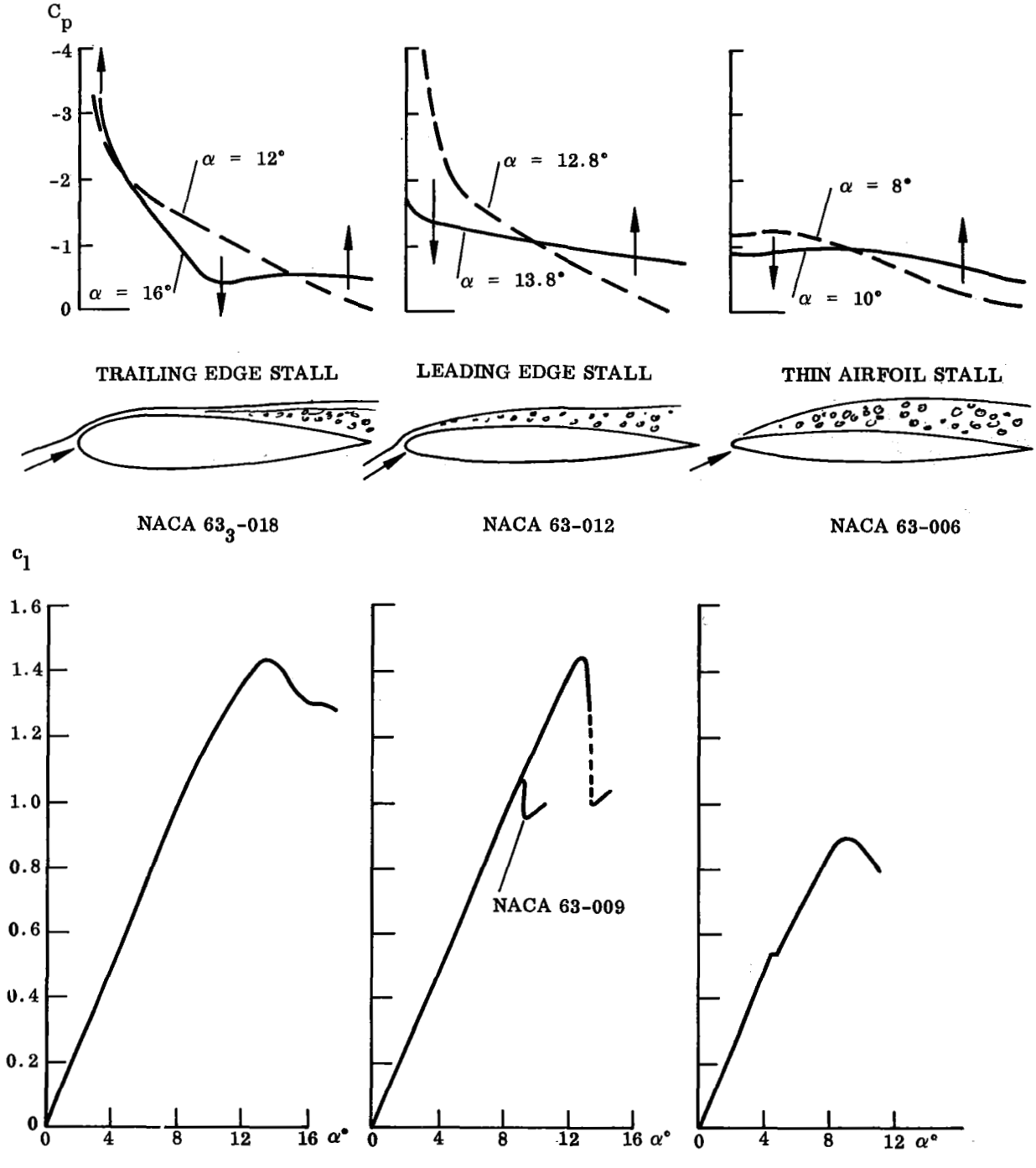

Fig. 1 Three Representative Types of Airfoil Stall

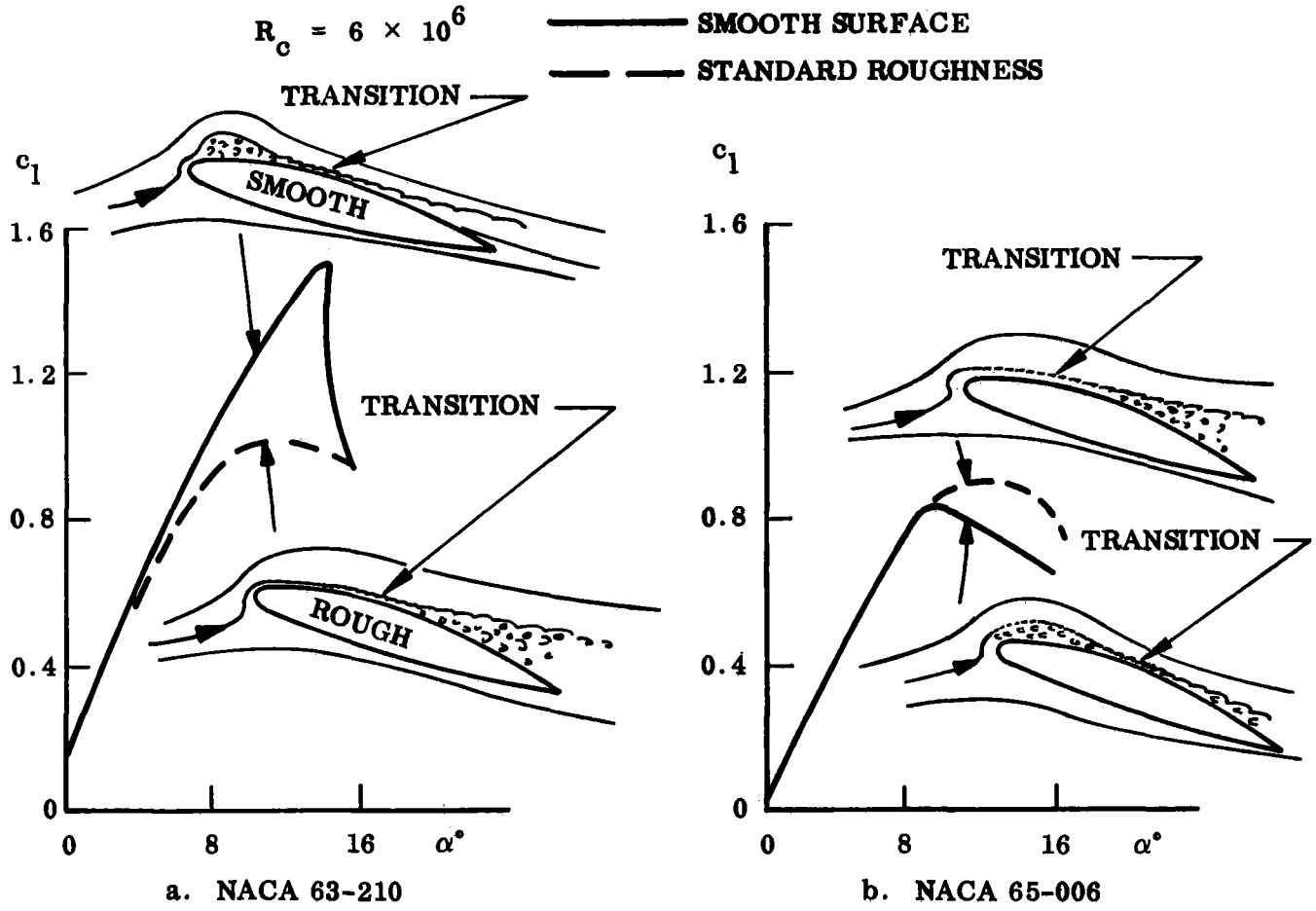

Fig. 2 Effect of Roughness on Stall Pattern

30×10^6 and 15×10^6, respectively, on NACA-0009 and NACA-0012 airfoils, according to the data in Ref. 12. At Reynolds numbers $R_c < 0.66 \times 10^6$ ($R_{eff} < 1.7 \times 10^6$) and $R_e < 0.33 \times 10^6$ ($R_{eff} < 0.9 \times 10^6$), respectively, the two airfoils have laminar trailing edge separation (Figs. 3a and 3b).

Available experimental data indicate that on a cambered airfoil the short laminar separation bubble at the leading edge can be present at the same time as turbulent trailing edge separation. On a NACA 4412 airfoil this has been observed at a Reynolds number $R_c = 0.34 \times 10^6$ or $R_{eff} = 0.9 \times 10^6$ (Refs. 9 and 13). On a RAF 28 airfoil it was observed that a long laminar separation bubble existed at the leading edge at the same time as turbulent trailing edge separation when the Reynolds number was somewhat lower, $R_c = 0.11 \times 10^6$ (Ref. 14). The result of this mixed separation is that the sharp lift stall associated with the leading edge separation is softened. The same is not necessarily true about the moment stall, as a statically stabilizing force couple results, regardless of type of separation (Fig. 1).

As the laminar separation bubble type of separation near the leading edge exists only on airfoils with rather sharp nose curvature, camber or nose droop will, of course, also accomplish this transfer to turbulent trailing edge stall (Ref. 12 and Fig. 4). It is the milder nose curvature and associated lessening of the adversity of the pressure gradient that produces the effect (Ref. 15 and Fig. 5 and also Ref. 16 and Fig. 6). Gault correlated all these stalling data (Ref. 17) and was able to present the results in normalized form (Fig. 7). The figure is very instructive and demonstrates that it will take very little camber to convert leading edge stall to trailing edge stall, and vice versa, if the camber and thickness combine to give values of the correlation parameter in the region $0.01 < (y_o \pm y_c)/c < 0.002$. The NACA 0.0012 airfoil with $y_o/c = 0.015$, is a prime candidate for this transition between stall types. Reynolds number variations below $R_c = 1.5 \times 10^6$ are apparently unimportant for this transition between stall types.

Recently another type of correlation has been made based upon approximating the forward airfoil shape by an ellipse. The correlation includes the effect of angle of attack

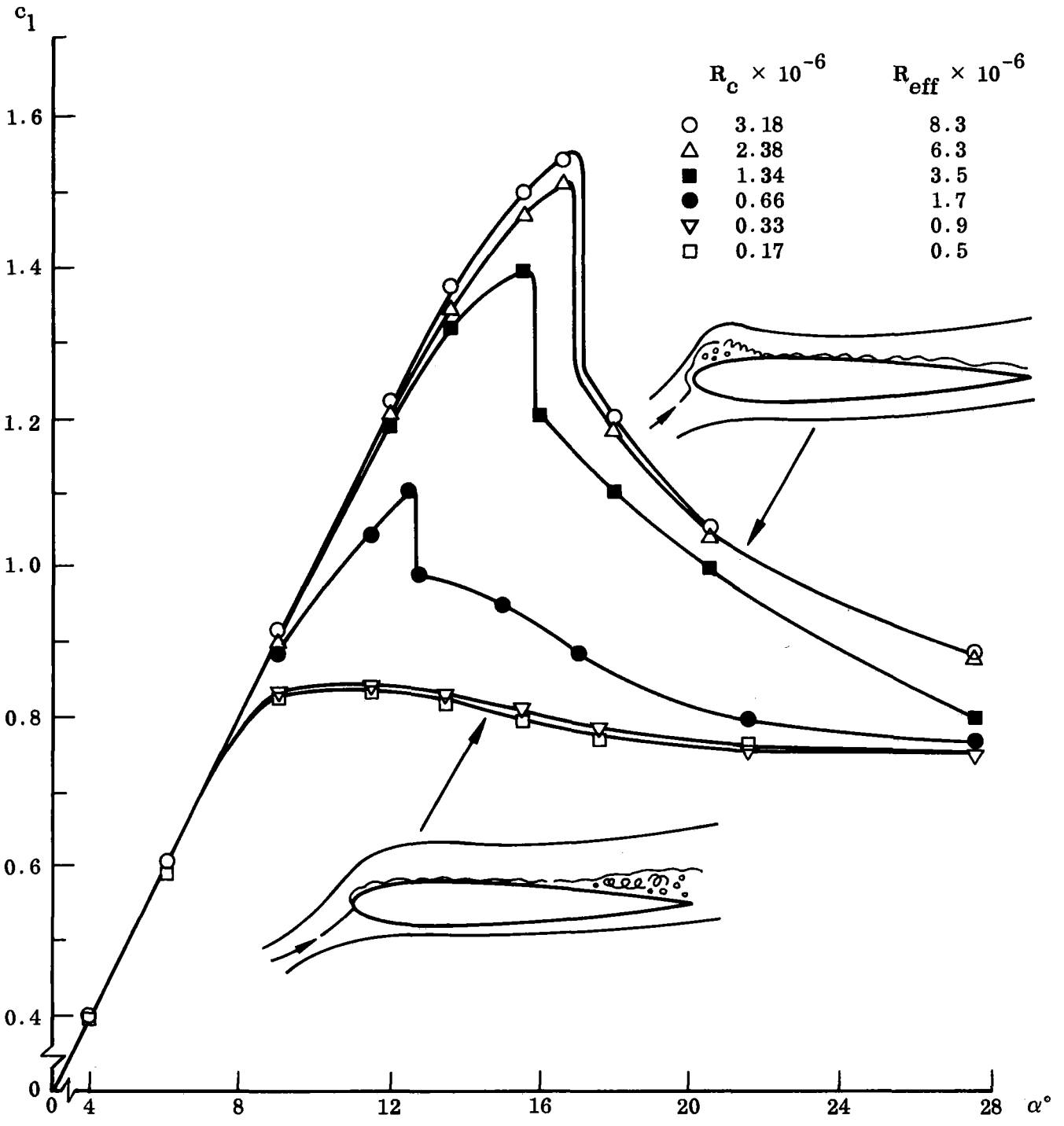

a. NACA 0012

Fig. 3a Effect of Reynolds Number on Airfoil Characteristics

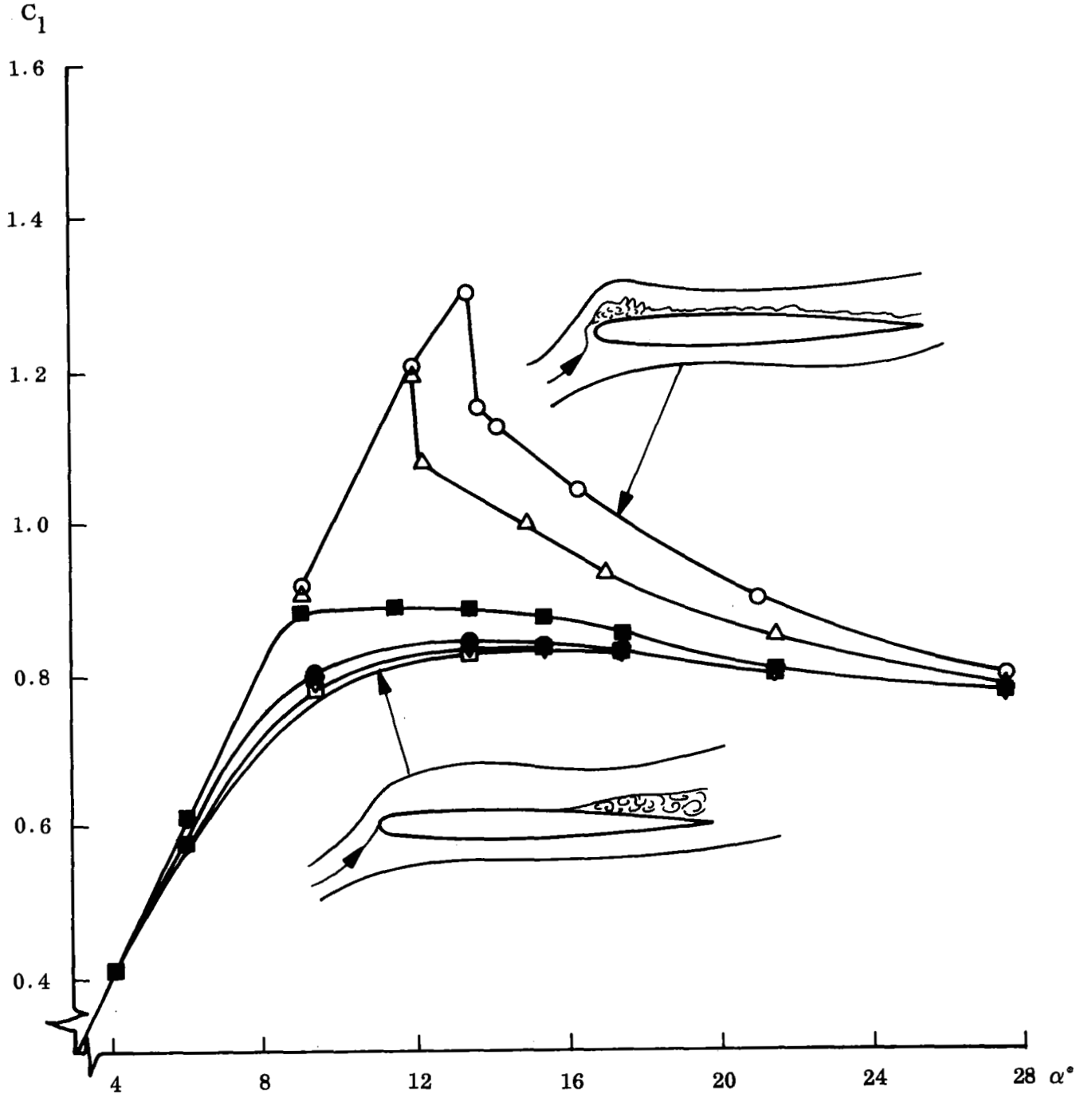

b. NACA 0009

Fig. 3b Effect of Reynolds Number on Airfoil Characteristics

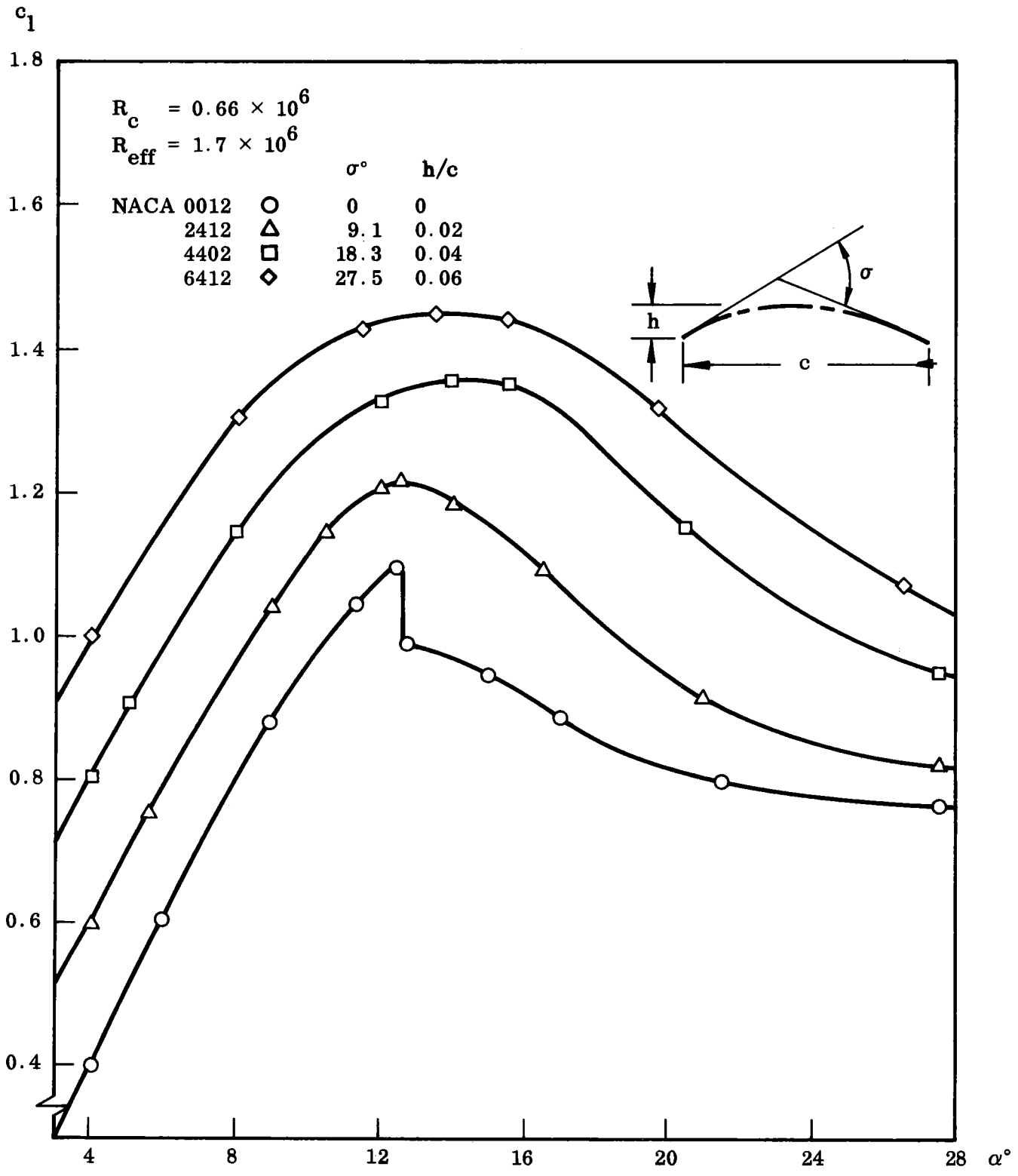

Fig. 4 Effect of Camber on Stall Pattern of NACA 0012 Airfoil Section

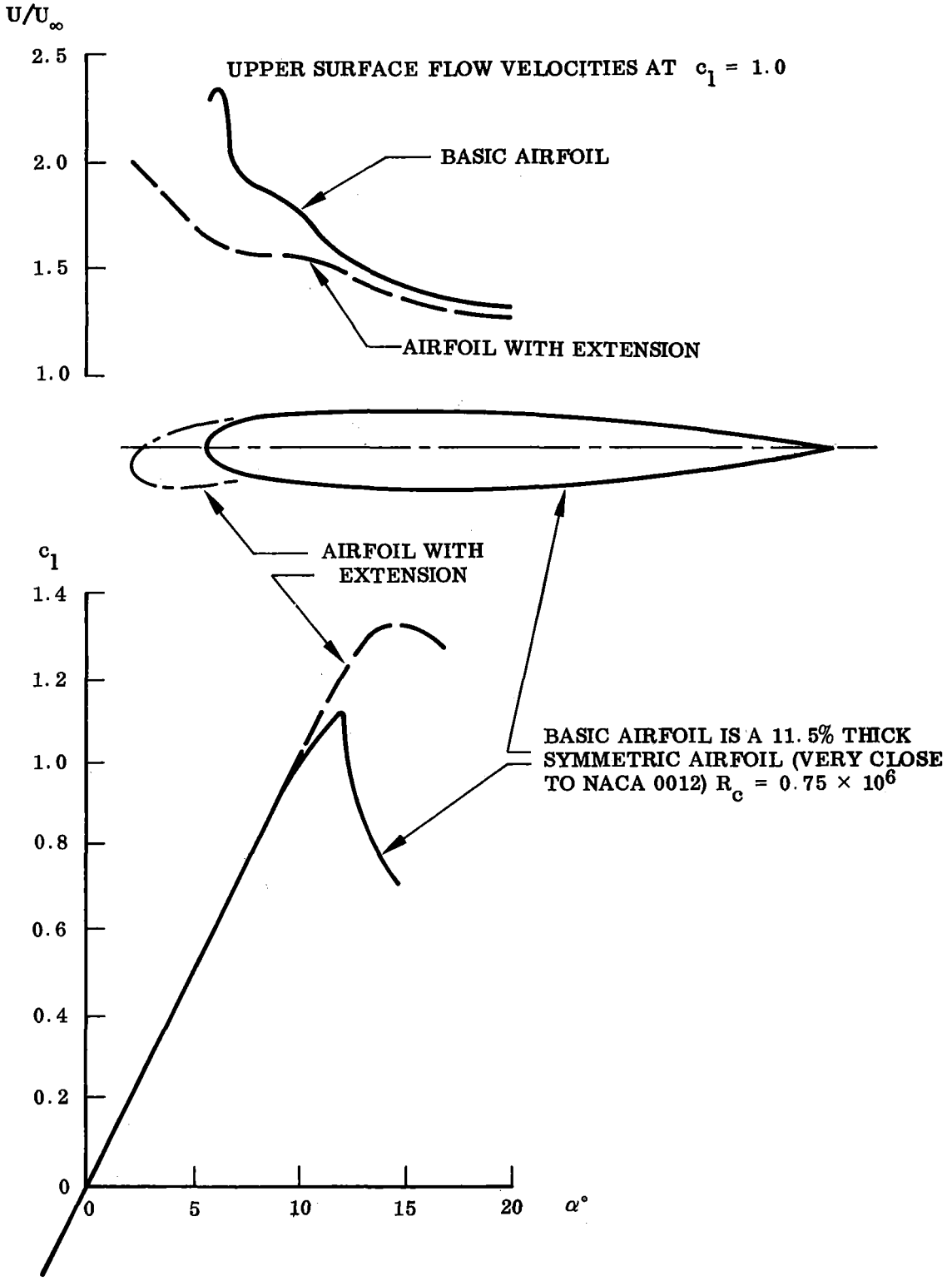

Fig. 5 Effect of Nose-Droop and Extension on $c_{l_{max}}$ and Top Surface Velocity Distribution Near Stall

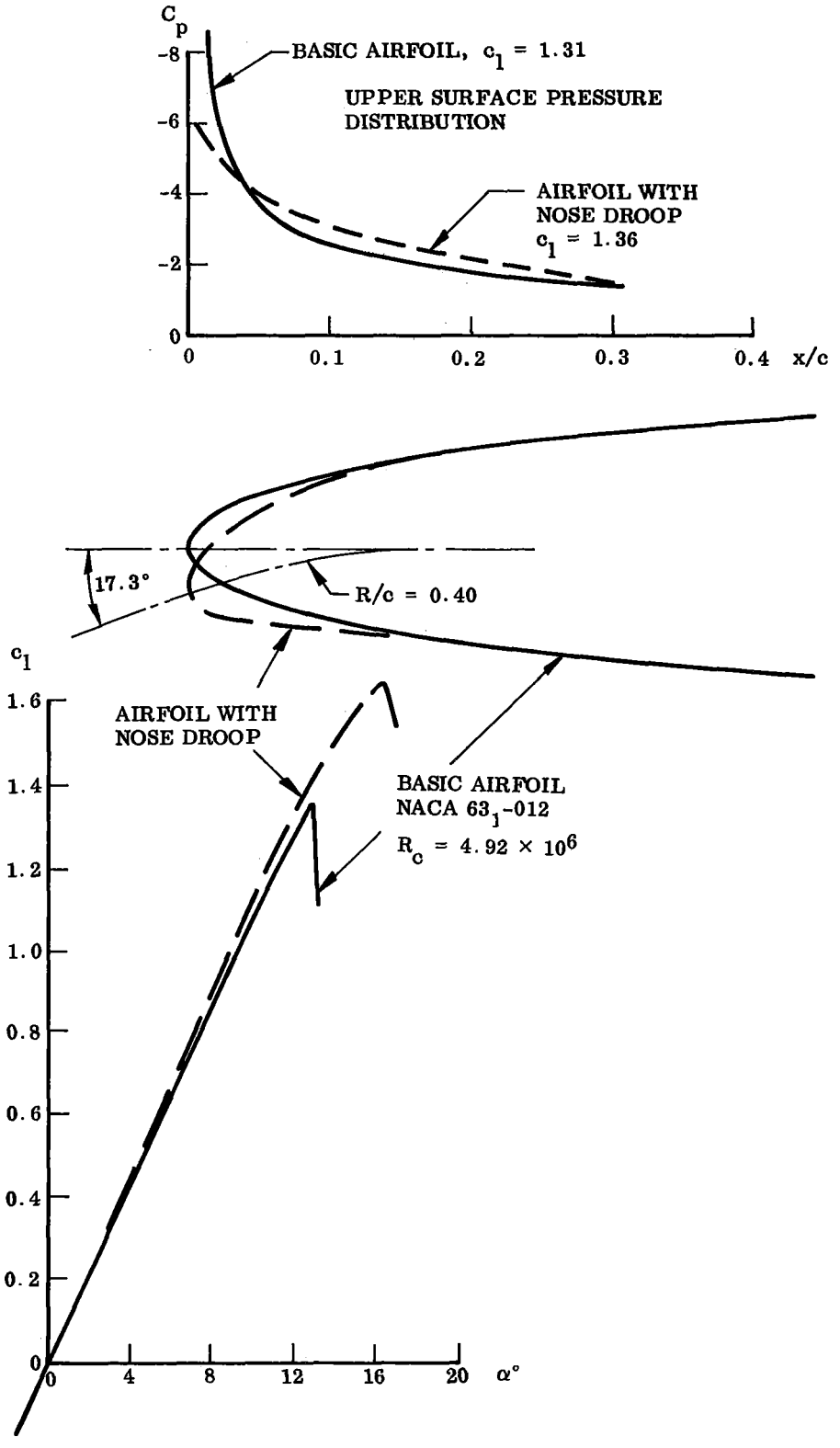

Fig. 6 Effect of Nose-Droop and Extension on $c_{l_{max}}$, α_{stall}, and Top Surface Pressure Distribution Near Stall

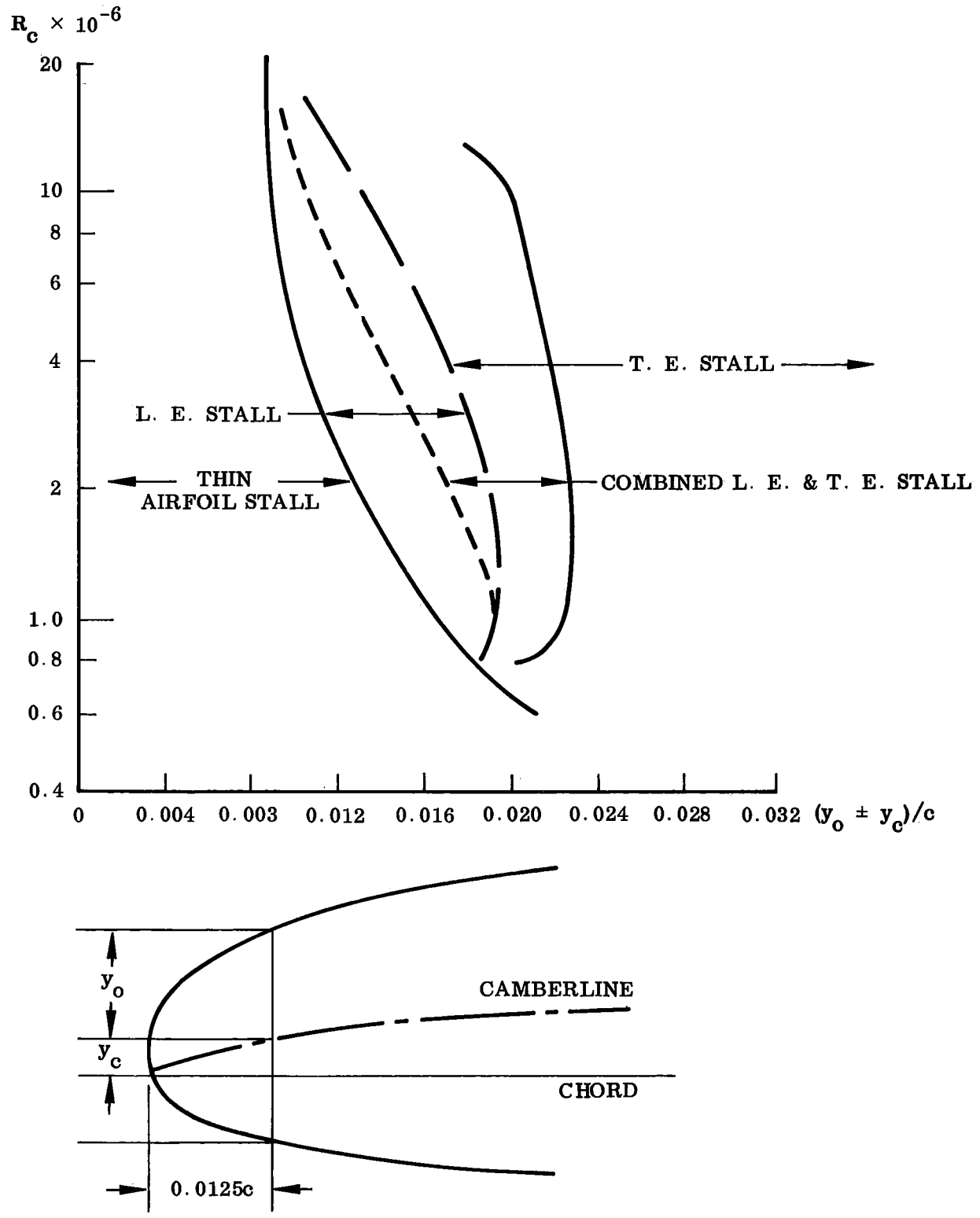

Fig. 7 Reynolds Number – Airfoil Thickness Map for Transition Between Stall Types

and Reynolds number normalized to the nose radius (Ref. 18 and Fig. 8). Again, camber can be included by considering top and bottom airfoil surfaces separately when selecting appropriate nose radii. The figure says that below a Reynolds number of 15,000 based upon nose radius a long laminar separation bubble with laminar or transitional reattachment is the separation pattern. (Only round-nosed airfoils that can be approximated by an elliptic nose shape are considered.) Again, as was demonstrated in Fig. 7, the transition between the short bubble or leading edge stall and the turbulent trailing edge stall is shown to be rather insensitive to Reynolds number and is determined mainly by effective nose radius (and angle of attack).

The abrupt leading edge stall can be expected to exhibit static α-hysteresis. That is, flow reattachment will not occur until the angle of attack has been decreased below the stall value (Ref. 19 and Fig. 9). The figure indicates that the lift-hysteresis starts well above the stall angle α_s. This is undoubtedly true in the region where the sudden leading edge separation has not reached its stable forward position ($\alpha_{reatt} < \alpha < 22°$). One can, of course, expect camber to have a large effect on the lift-hysteresis. Carrow has shown this to be true for laminar trailing-edge separation (Ref. 9 and Fig. 10). The low Reynolds number $R_c = 0.16 \times 10^6$ permits change to leading edge separation because of the large nose radius (giving a large R_{r_n} and low A, $A = \alpha/\sqrt{r_n/2c}$, Fig. 8). The lowest boundary for the lift-hysteresis would be the flat plate characteristics which correspond to the most forward separation off the leading edge (Refs. 15, 19, and Fig. 11). The effect of increasing the nose radius is well illustrated by the experimental data for the modified 18 percent thick NACA 0018 airfoil (Ref. 20 and Fig. 12).

The turbulent trailing edge separation is very different in nature from the leading edge separation and will, for instance, not exhibit any static hysteresis effects. Kline (Ref. 21) describes the turbulent separation very much the same way as boundary layer transition, i.e., the separation does not occur suddenly but is present down to low adverse pressure gradients or low angles of attack in form of transitory stall spots that originate in the laminar sublayer. Thus, the gradual loss of lift can be thought of as a measure of the intermittency factor for turbulent stall. As the pressure gradient grows more and more adverse (with increasing α) the spots grow in number and size, start to coalesce, and finally destabilize the entire flow to develop full stall.

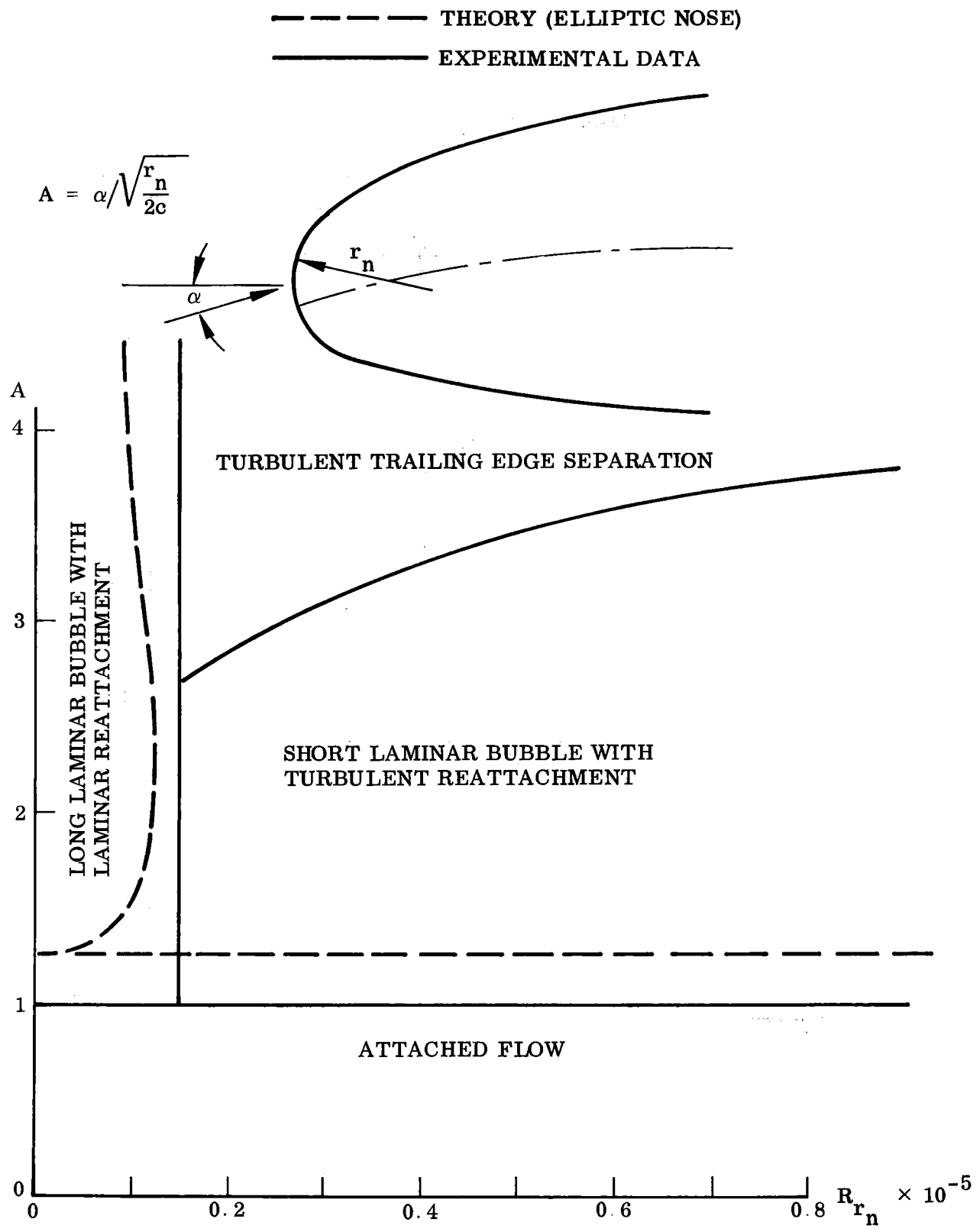

Fig. 8 Dependence of Stall Pattern on Angle-of-Attack, Nose Radius, and Reynolds Number

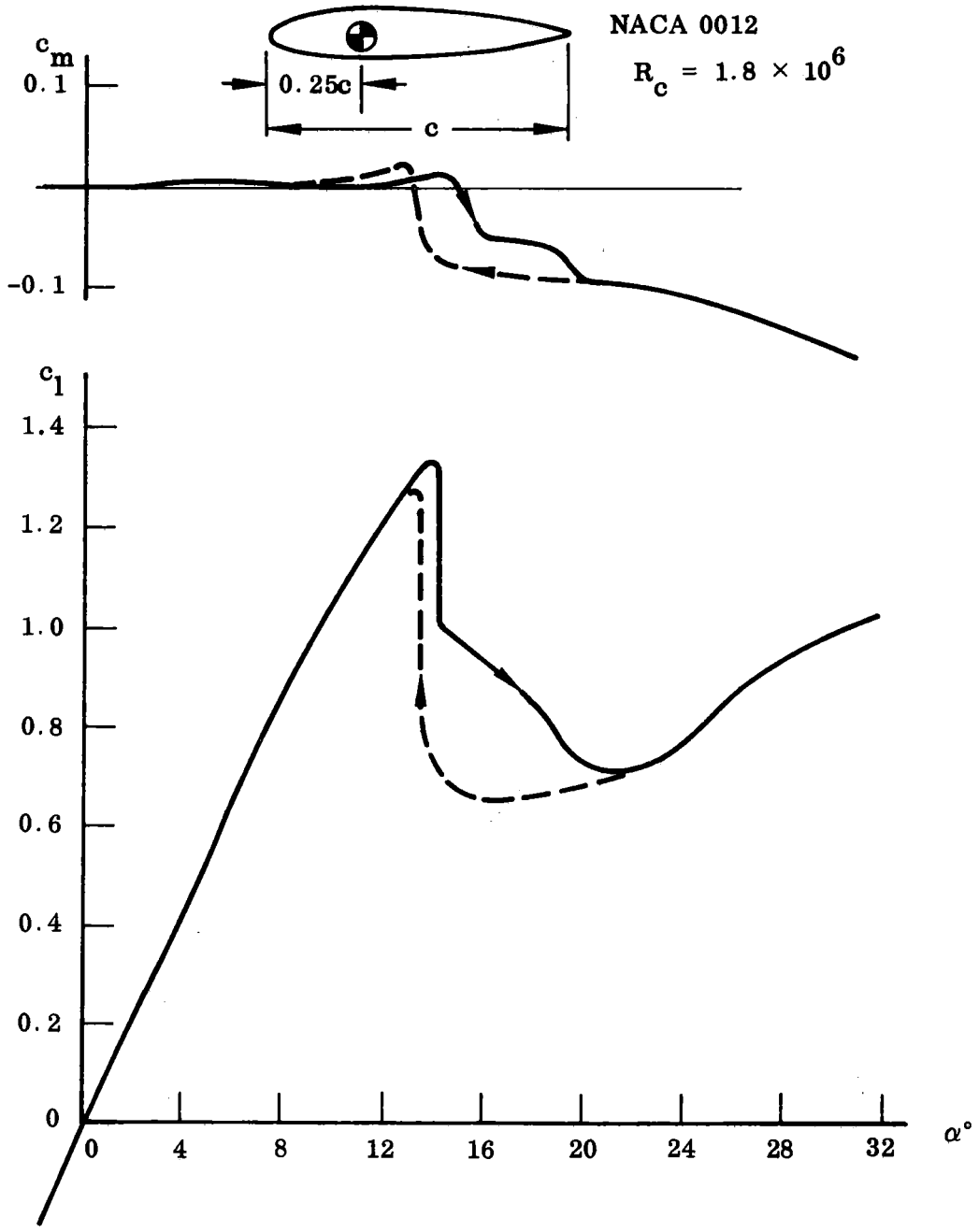

Fig. 9 Static Aerodynamic Hysteresis for Leading Edge Stall

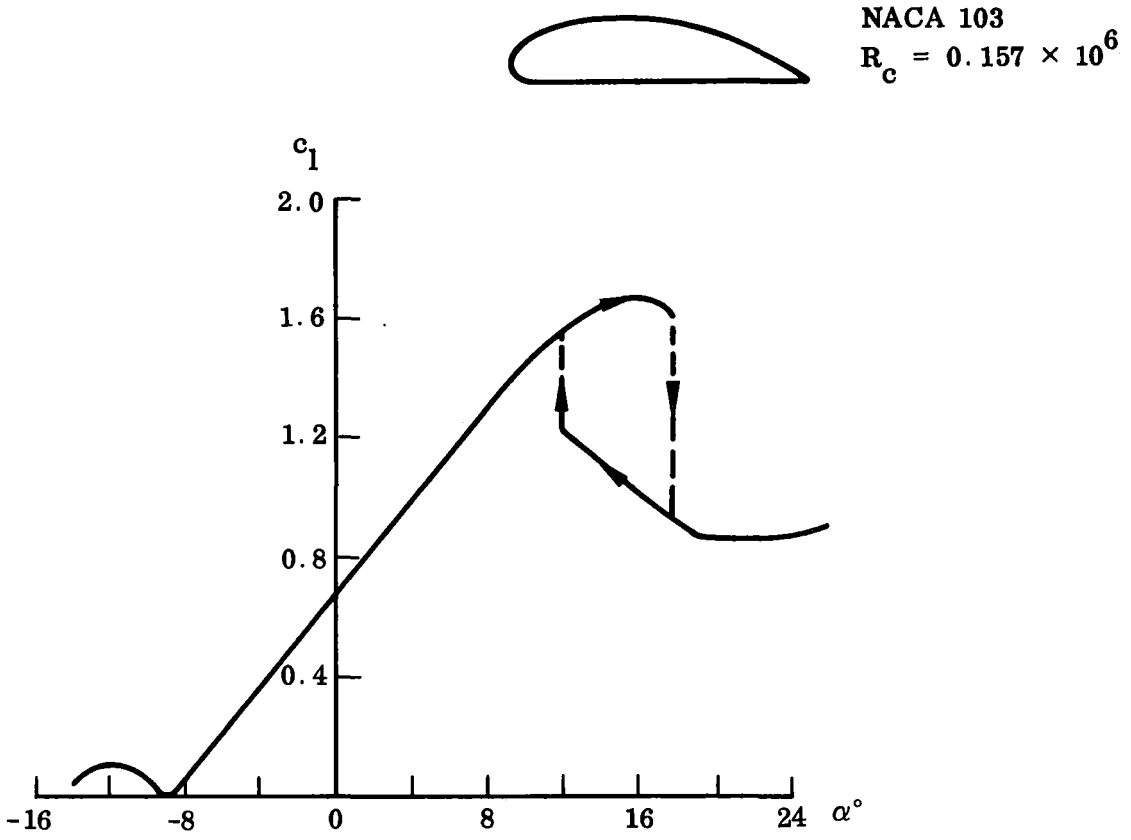

Fig. 10 Static Aerodynamic Hysteresis for Laminar Trailing Edge Separation

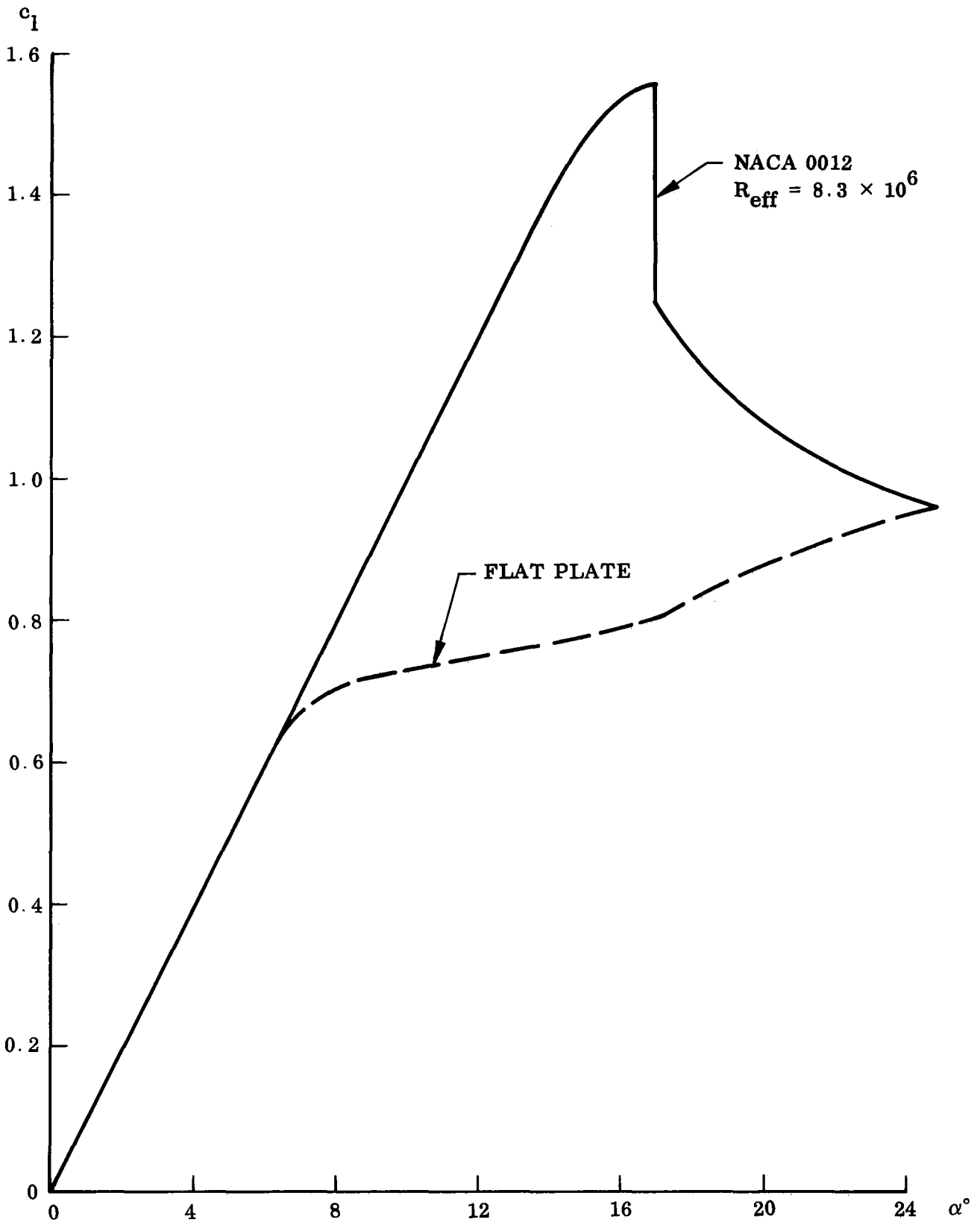

Fig. 11 Limiting Flat Plate Airfoil Characteristics

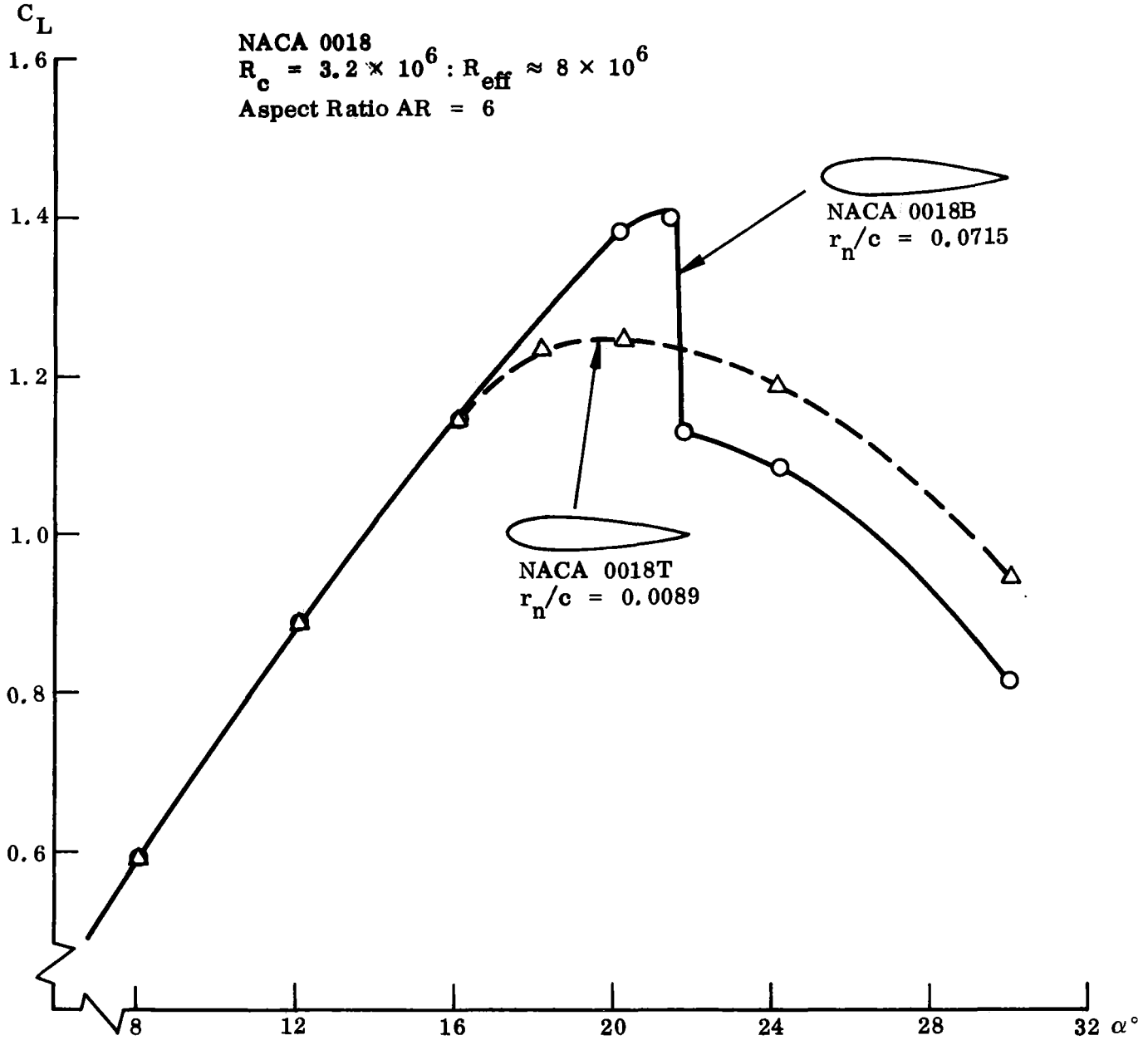

Fig. 12 Effect of Nose Radius on Stall Pattern

After having been exposed to this display of how small changes of geometry or environment can drastically change the static stall characteristics, one should be somewhat prepared to expect the unusual and apparently anomalous unsteady stall behaviors to be discussed next.

2.2 UNSTEADY STALL

Unsteady airfoil stall is encountered by aircraft penetrating the stall region (Ref. 22). However, it is today better known as the blade stall problem of high performance compressors and helicopters (Refs. 1 and 2). The aircraft problem is somewhat simpler, and will be discussed first in order to provide some basic insight before the more complicated problem of oscillatory stall is discussed.

2.2.1 Dynamic Stall Penetration

Substantial overshoot of the static $C_{L_{max}}$ has been observed on aircraft penetrating the stall at non-zero angle-of-attack rates (Ref. 23 and Fig. 13). One obvious reason for the overshoot, after seeing the large effects of nose-droop on static stall (Figs. 5 and 6), is the pitch rate induced apparent nose droop (Fig. 14). However, one finds that even for the high sensitivity found by Kelly (Ref. 16 and Fig. 6) the apparent nose droop only accounts for a few percent of the observed $\partial C_{L_{max}}/\partial (c\dot{\alpha}/U_\infty)$, both in wind tunnel tests and flight tests, with both leading edge and trailing edge type stall (Refs. 22-26, Figs. 15 and 16).

The overshoot of α_{stall} and corresponding overshoot of $C_{L_{max}}$ at low Mach numbers are almost entirely caused by the pitch rate induced flow acceleration and corresponding delay of the adversity of the leeward side pressure gradient, the "frequency induced plunging" described in Ref. 27. The decrease of the adversity of the pressure gradient is proportional to $(c\dot{\alpha}/U_\infty)$ – see Section 3 for details – and the overshoot of the stall angle of attack will also be proportional to $(c\dot{\alpha}/U_\infty)$ until the "saturation point" is reached, see Fig. 13. For leading edge type of stall the α_s-overshoot $\Delta\alpha_s$ gives

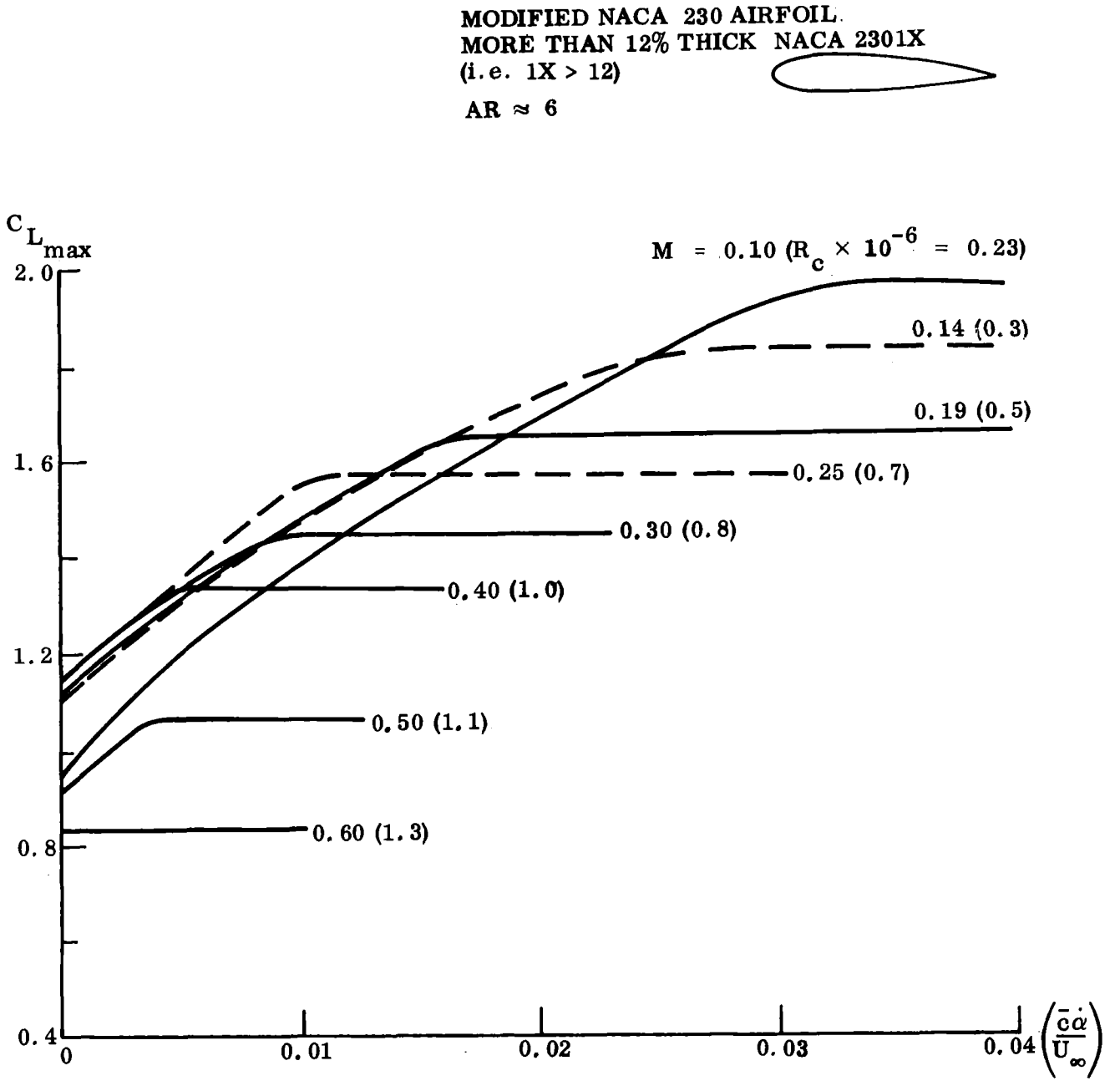

Fig. 13 Dynamic Stall and $C_{L_{max}}$ -Overshoot

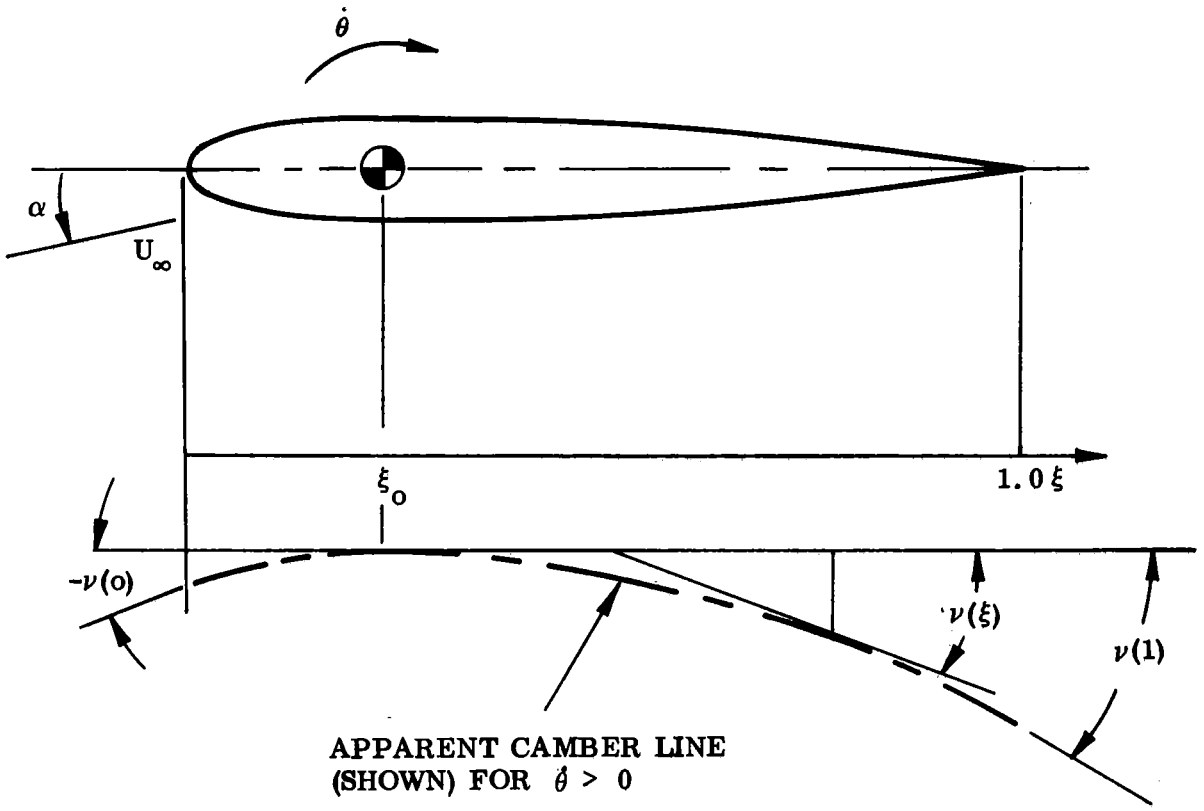

$$\nu(\xi) = (\xi - \xi_o)\frac{c\dot{\theta}}{U_\infty}$$

NOSE DROOP: $-\nu(o) = \xi_o \frac{c\dot{\theta}}{U_\infty}$

CAMBER ANGLE: $\sigma = \nu(1) - \nu(o) = \frac{c\dot{\theta}}{U_\infty}$

Fig. 14 Pitch Rate Induced Nose-Droop and Airfoil Camber

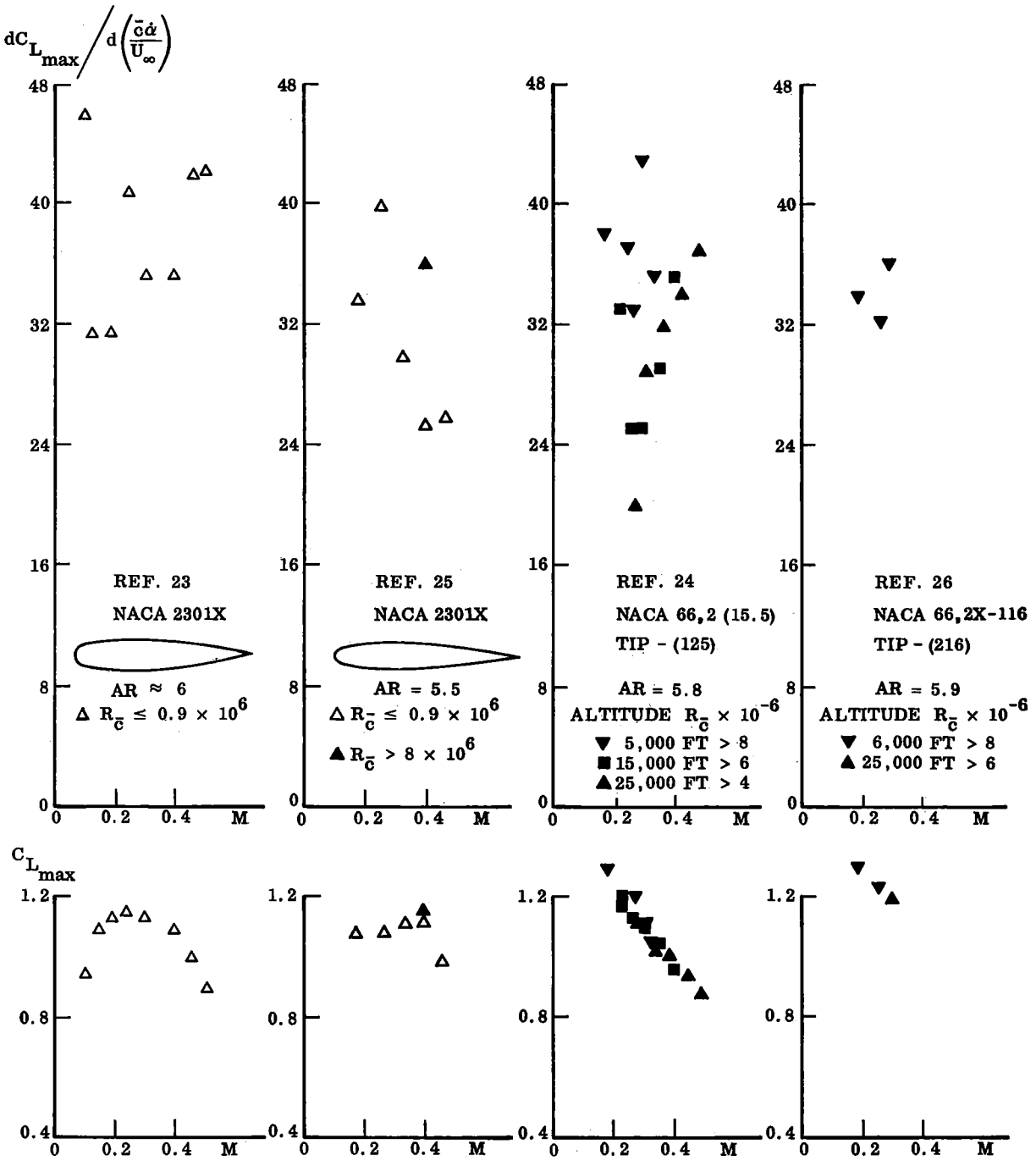

a. $C_{L_{max}}$ AND $C_{L_{max}}$ -OVERSHOOT DERIVATIVES AS FUNCTIONS OF MACH NUMBER

Fig. 15a $C_{L_{max}}$ -Overshoot Characteristics for Leading Edge Stall

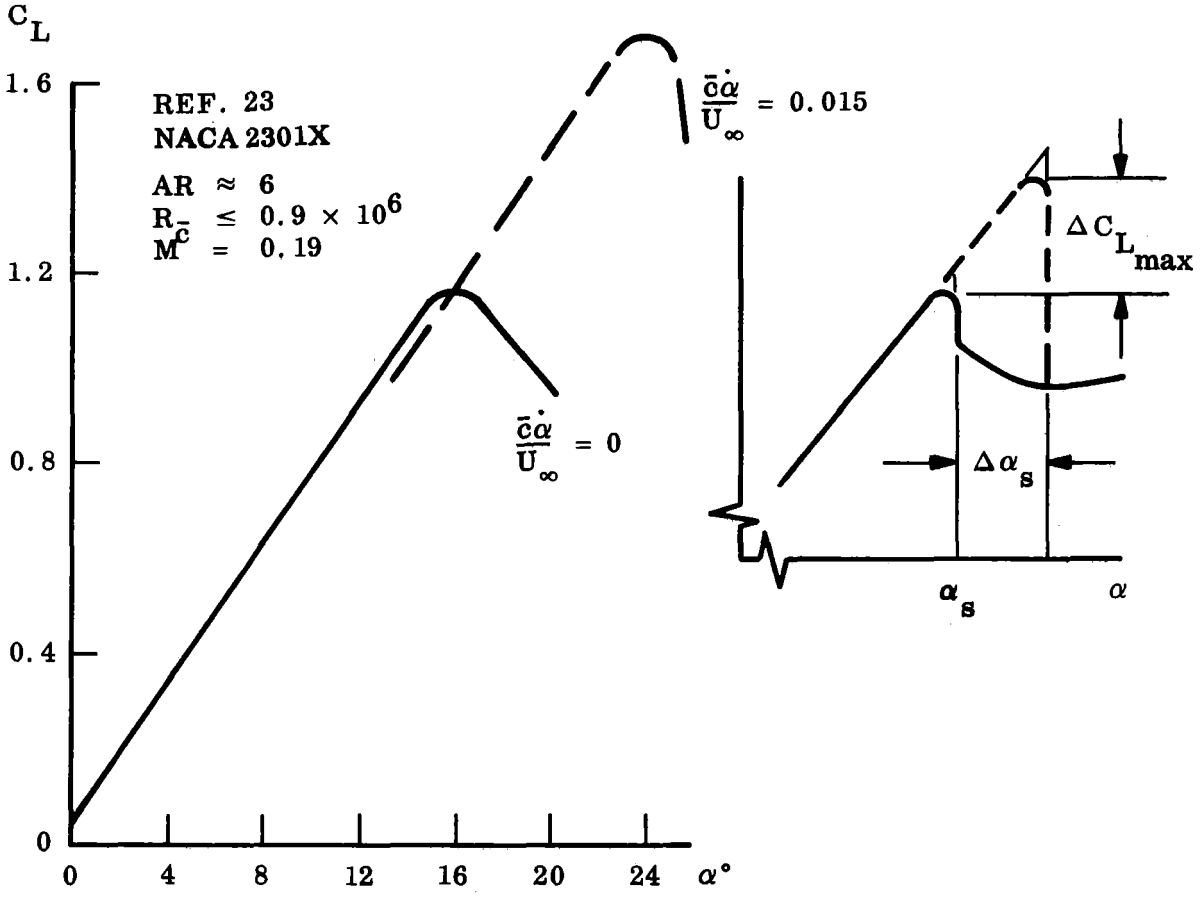

b. C_L AS FUNCTION OF α FOR VARIOUS PITCH RATES

Fig. 15b $C_{L_{max}}$ -Overshoot Characteristics for Leading Edge Stall

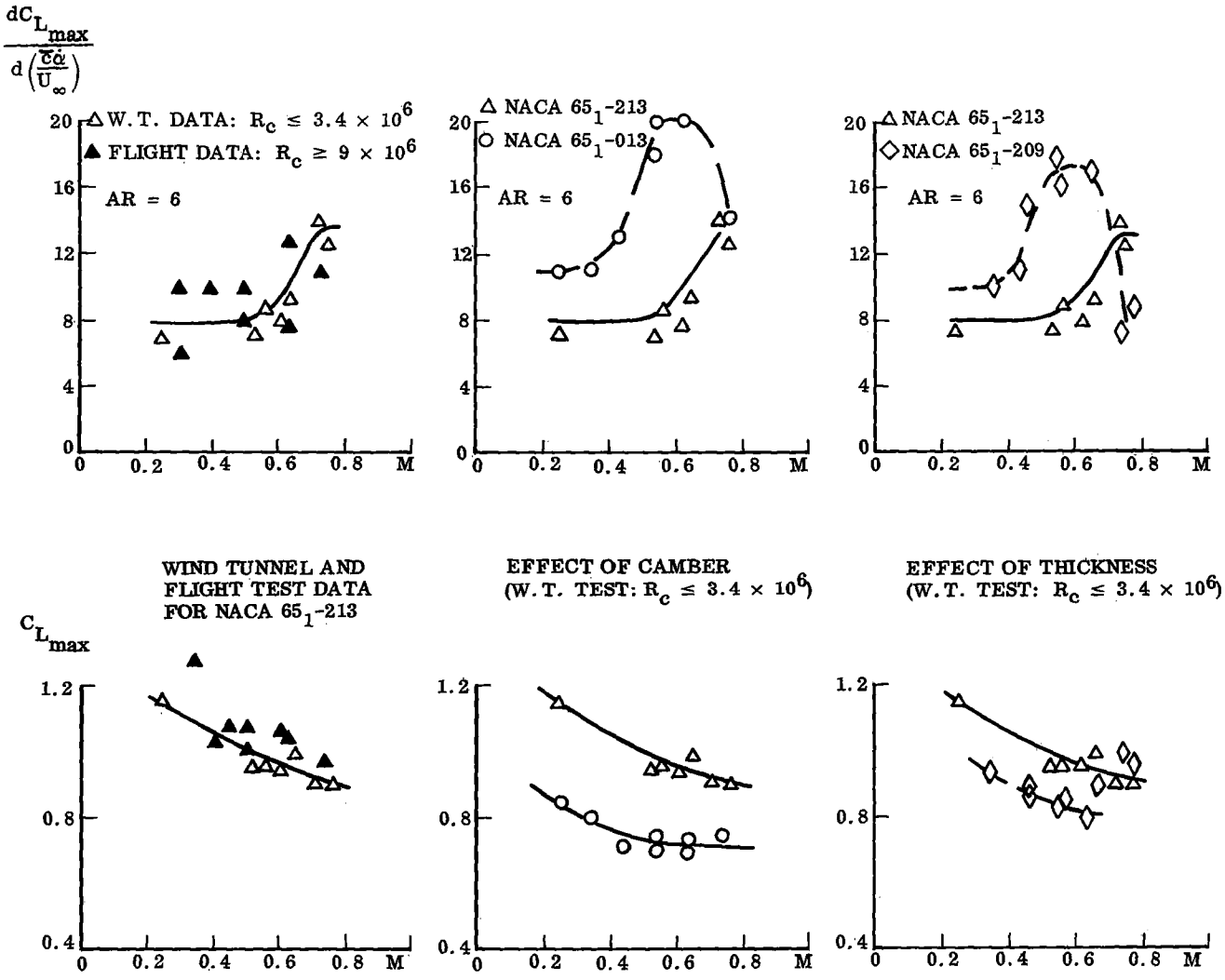

a. $C_{L_{max}}$ AND $C_{L_{max}}$ -OVERSHOOT DERIVATIVE AS FUNCTIONS OF MACH NUMBER

Fig. 16a $C_{L_{max}}$ -Overshoot Characteristics for Trailing Edge Stall (Ref. 22)

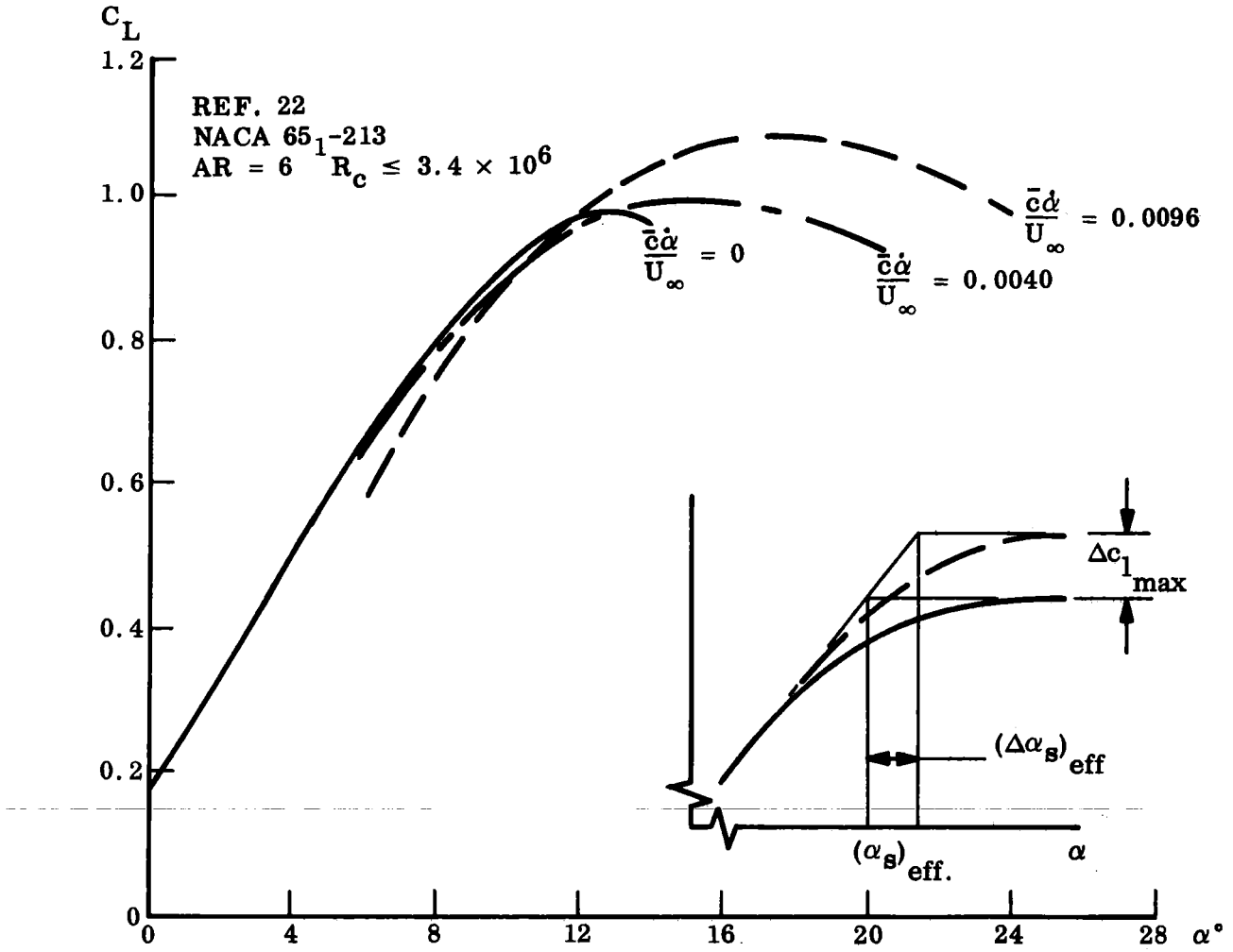

b. C_L AS FUNCTION OF α FOR VARIOUS PITCH RATES

Fig. 16b $C_{L_{max}}$-Overshoot Characteristics for Trailing Edge Stall (Ref. 22)

directly an overshoot $\Delta C_{L_{max}} = C_{L_\alpha} \cdot \Delta\alpha_s$ of the maximum lift (Fig. 15b). Similarly, an effective $\Delta\alpha_s$ can be defined for the $C_{L_{max}}$ overshoot of trailing edge stall (Fig. 16b). Thus, the overshoot derivative $\partial\alpha_s/\partial(c\dot{\alpha}/U_\infty)$ shown in Fig. 17 can be obtained by dividing the $C_{L_{max}}$-overshoot derivatives with C_{L_α}. Writing the overshoot $\Delta\alpha_s$ as follows

$$\Delta\alpha_s = \frac{\partial\alpha_s}{\partial\left(\frac{\bar{c}\dot{\alpha}}{U_\infty}\right)} \frac{\bar{c}\dot{\alpha}}{U_\infty} = (\dot{\alpha})_{mean} \Delta t = \left(\frac{\bar{c}\dot{\alpha}}{U_\infty}\right)_{mean} \Delta\xi_a$$

shows that the derivative in Fig. 17 is equivalent to a dimensionless time lag $\Delta\xi_a$, $1 < \Delta\xi < 9$, where $\Delta\xi_a$ is the distance in cord lengths that the airfoil travels during the acceleration produced overshoot of α_s (and $C_{L_{max}}$). The large values of this equivalent time lag means that the dynamic effects of flow separation can be large even when the static effects are small. At higher subsonic speeds, the $C_{L_{max}}$ overshoot is negligible (Ref. 23 and Fig. 13). This does not, however, mean that the acceleration-induced effects are negligible. As is illustrated in Fig. 18 (Ref. 28), the shock-induced separation existing at higher Mach numbers induces a force couple $\Delta C_{N_1} - \Delta C_{N_2}$ which varies with α but does not produce any net lift. The fact that "local" attached flow lift is practically cancelled by separation induced lift is of little significance dynamically, as the two forces are affected by the unsteady motion differently.* That is, the dynamic effects can be large and adverse. The shock-boundary layer interaction on airfoils at high subsonic Mach numbers is very similar to the flow phenomenon existing on cone-cylinders at high subsonic Mach numbers (Refs. 29 and 30).

Although the pitch rate induced nose droop was negligible and hardly could cause a change from leading edge to trailing edge type stall, the accelerated flow effect can. Some of the wind tunnel test results in Ref. 22 indicate that this might have happened (Fig. 19). Shock-augmented, leading-edge type stall at low angular rates would give the observed high $C_{L_{max}}$ overshoot. At higher angular rates, the milder pressure

*See Section 3 for the treatment of trailing-edge separation.

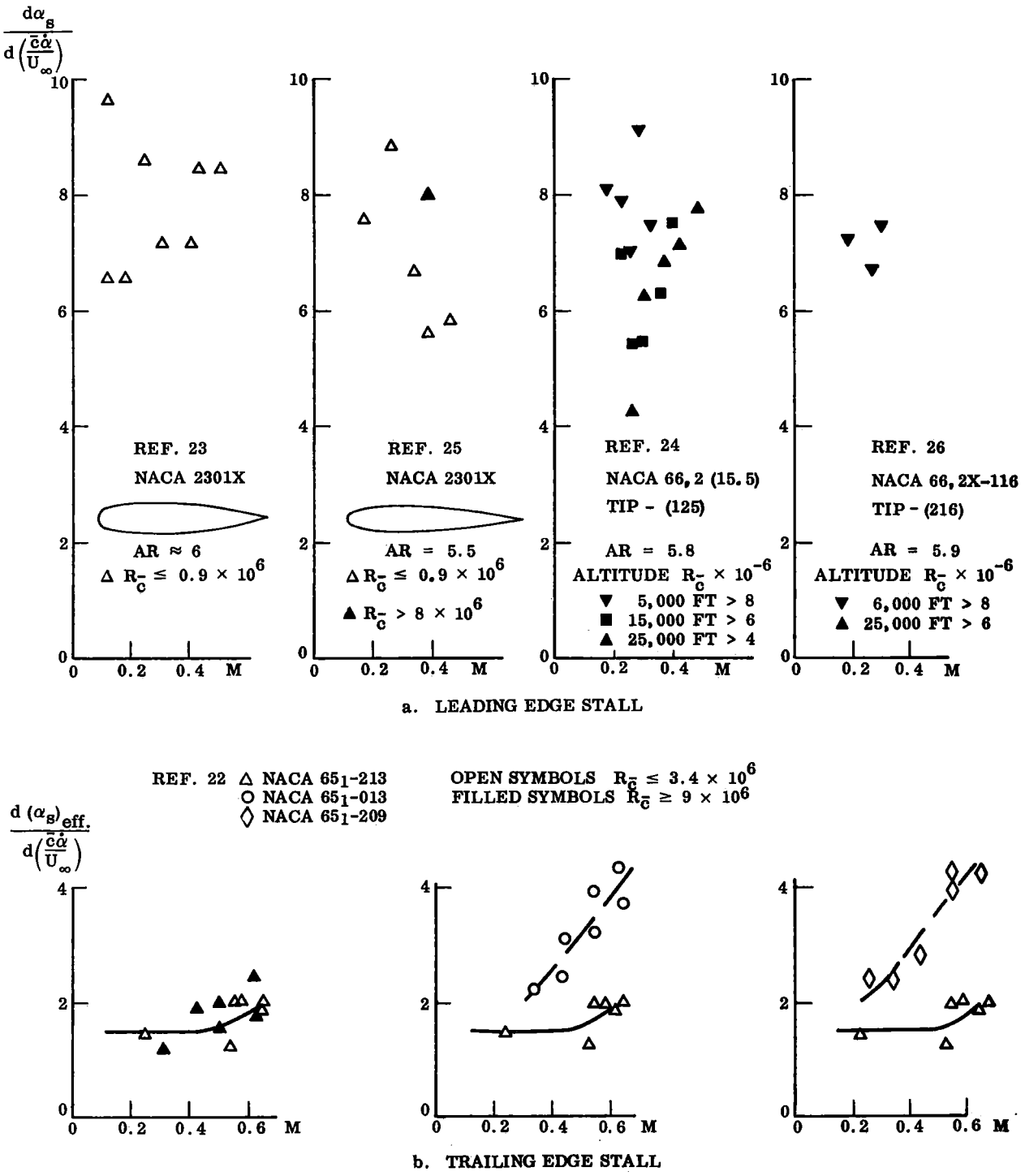

Fig. 17 Derivatives for Linear Dependence of α_{stall}-Overshoot on Normalized Pitch Rate

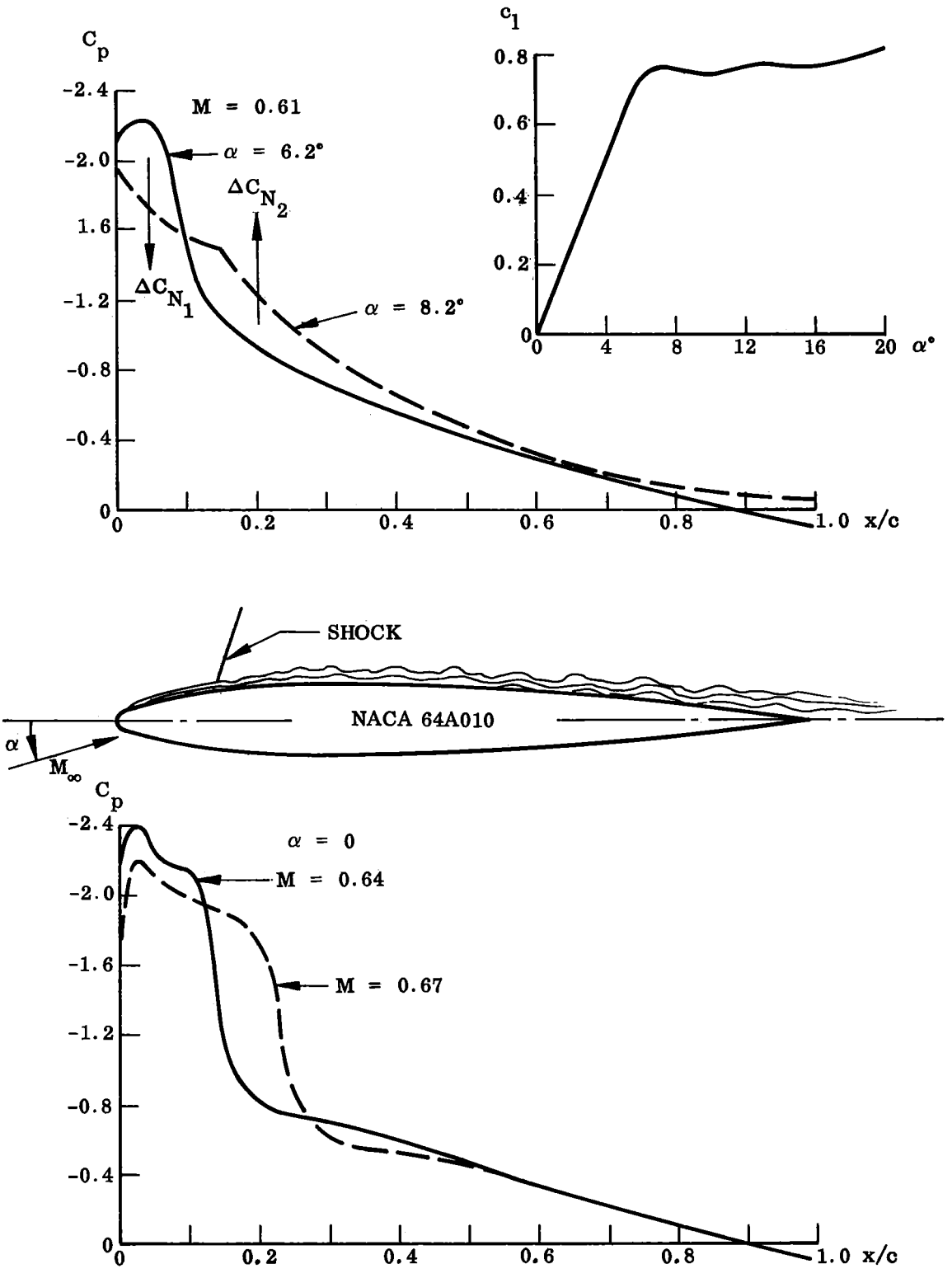

Fig. 18 Shock-Boundary Layer Interaction on Airfoil NACA 64A010 at High Subsonic Mach Numbers

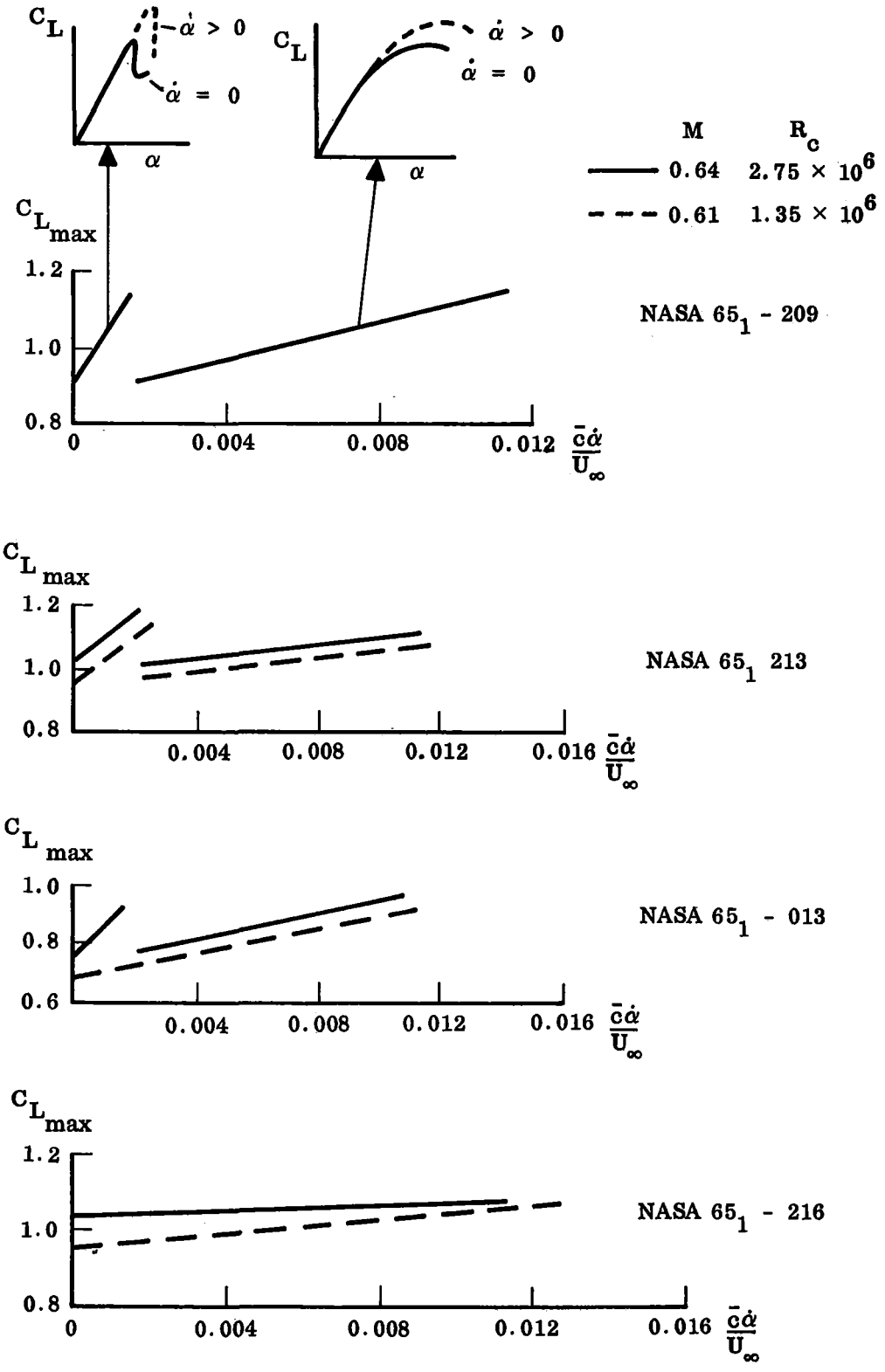

Fig. 19 Evidence of Change of Dynamic Stall Pattern With Increasing Normalized Pitch Rate

gradient (at the same angle-of-attack) promotes trailing edge type stall with its lower $C_{L_{max}}$ overshoot. The observed overshoot on helicopter blades (Ref. 30) or oscillating airfoils (Ref. 3) is also of the magnitude discussed above (Fig. 20).

2.2.2 Oscillatory Stall and Stall Flutter

A classic, often referenced investigation of oscillatory stall and stall buffet, is the one by Halfman, Johnson, and Haley (Ref. 3). They observed the now familiar anomalous oscillatory $C_L(\alpha)$- and $C_M(\alpha)$-loops (Fig. 21). Leaving the energy dissipation and (un)damping discussion for later, we will take a look at the time average $C_L(\alpha)$ and $C_M(\alpha)$ curves obtained in oscillations in pitch and translatory oscillations. Three 12% thick airfoils were investigated, one blunter and one sharper than the NACA-0012 airfoil (Fig. 22). The blunt wing behaved very much as could be expected from the discussion in previous sections. Thus the translatory oscillation gave time average values that agreed with the static characteristics, when an apparent zero shift is corrected for (Fig. 23a). For oscillations in pitch the generated accelerated flow effect caused the stall to change from leading edge type to the gradual trailing edge type stall, causing time average values* high above static C_L for $\alpha > \alpha_s$ (Fig. 23b). The sharp wing, however, shows some surprising characteristics. An unexpected overshoot of the translatory time average was observed** (Fig. 24a). The only rational explanation we have been able to find is that the translatory oscillation generates a higher effective Reynolds number than the nominal $R_c = 10^6$, causing a change from abrupt to smooth stall. It could be connected with the observed zero shift. However, this is unlikely in view of the fact that the pitch oscillation gives no zero shift but the same unexplainable overshoot of $C_{L_{max}}$ (Fig. 24b). The oscillations around $\alpha = 22°$ of 6 degree amplitude will never "reach down"*** to the static curve to produce the type overshoot discussed for the blunt wing (Fig. 23b). When comparing all three wings (Fig. 25) this explanation seems to hold. Thus, the translatory oscillation affects the overshoot only

---

*That is, the centroids of the dynamic loops (see Fig. 26 for example).
**Zero shift still apparent.
***The oscillations are not fast enough to build up a "circulatory residue" to cause attached flow on the "next upstroke." (See Section 3.)

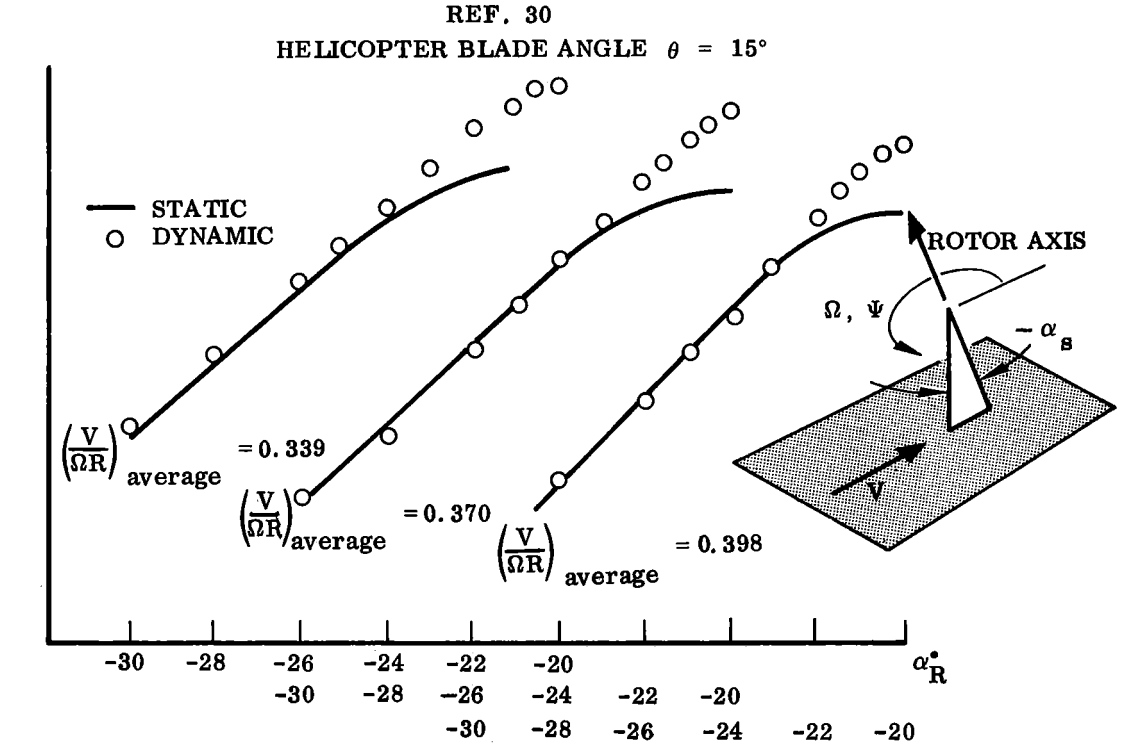

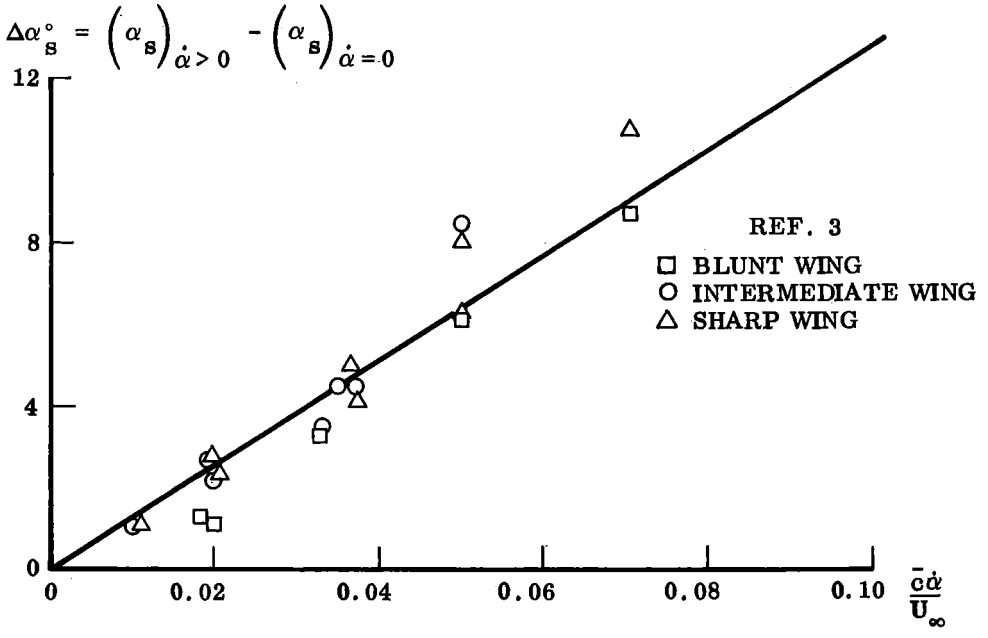

Fig. 20 Helicopter Rotor and Oscillatory Airfoil Data for Dynamic Stall Overshoot

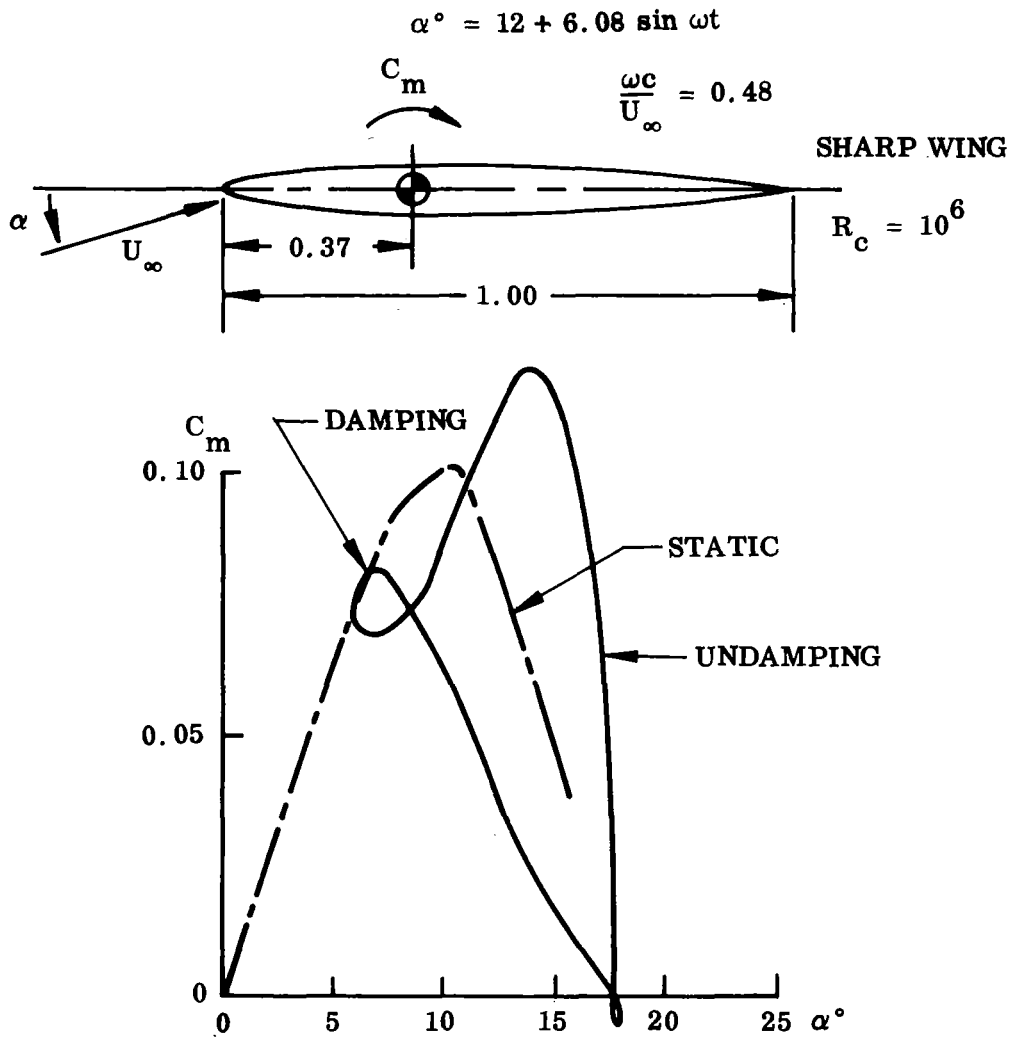

Fig. 21 Typical "Anomalous" Oscillatory $C_m(\alpha)$-loop

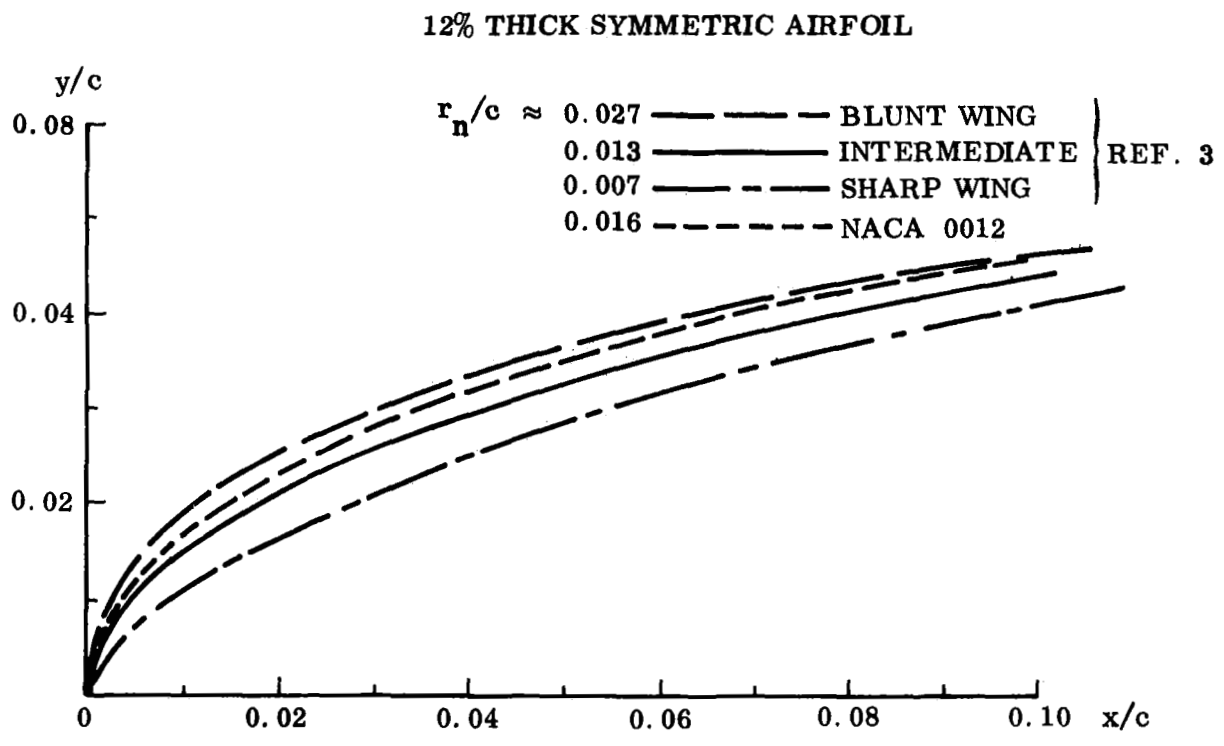

Fig. 22 Comparison Between Airfoils in Ref. 3 and NACA 0012

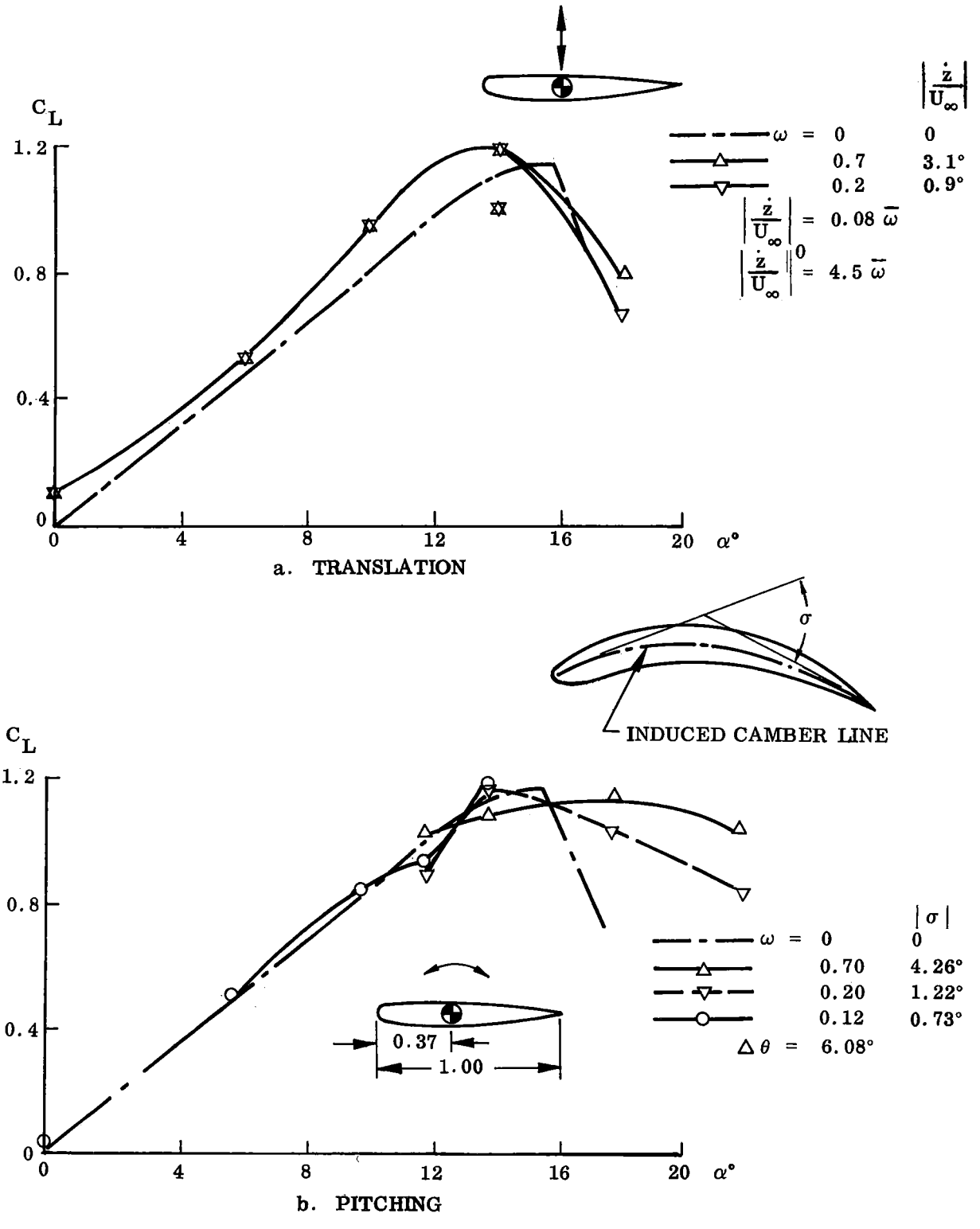

Fig. 23 Time Average $C_L(\alpha)$-Curves for Blunt Wing at $R_c = 10^6$

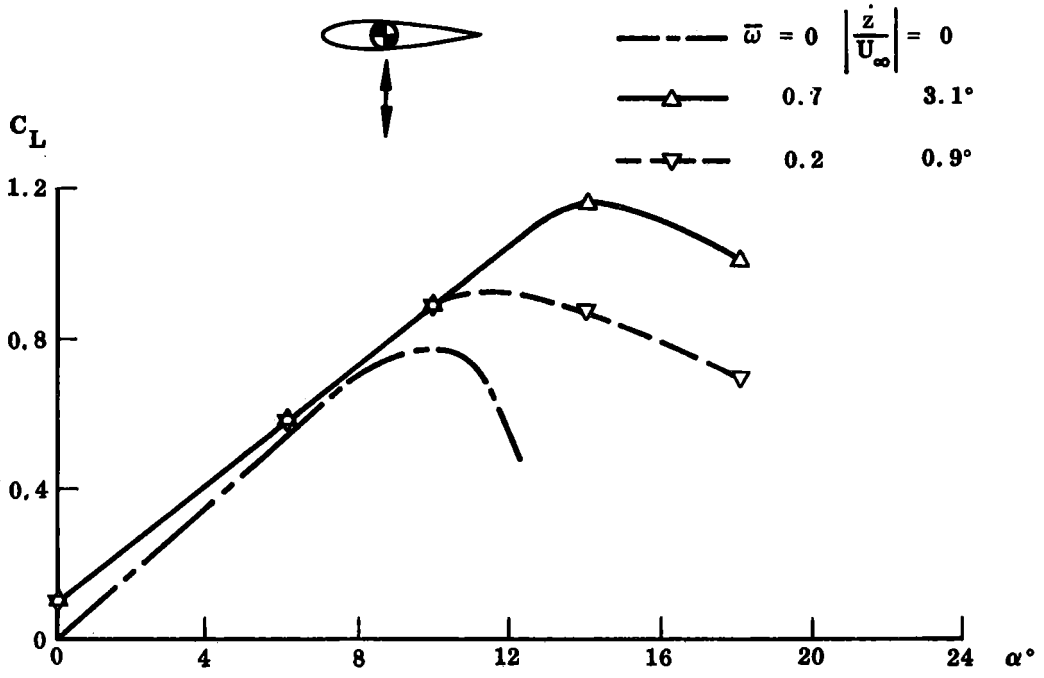

a. TRANSLATION

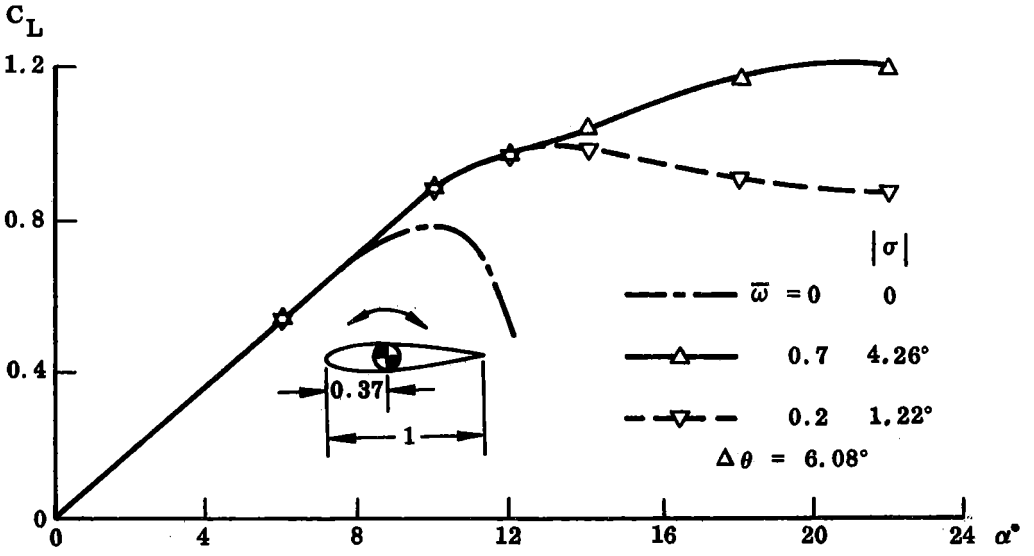

b. PITCHING

Fig. 24 Time Average C_L (α)-Curves for Thin Wing at $R_c = 10^6$

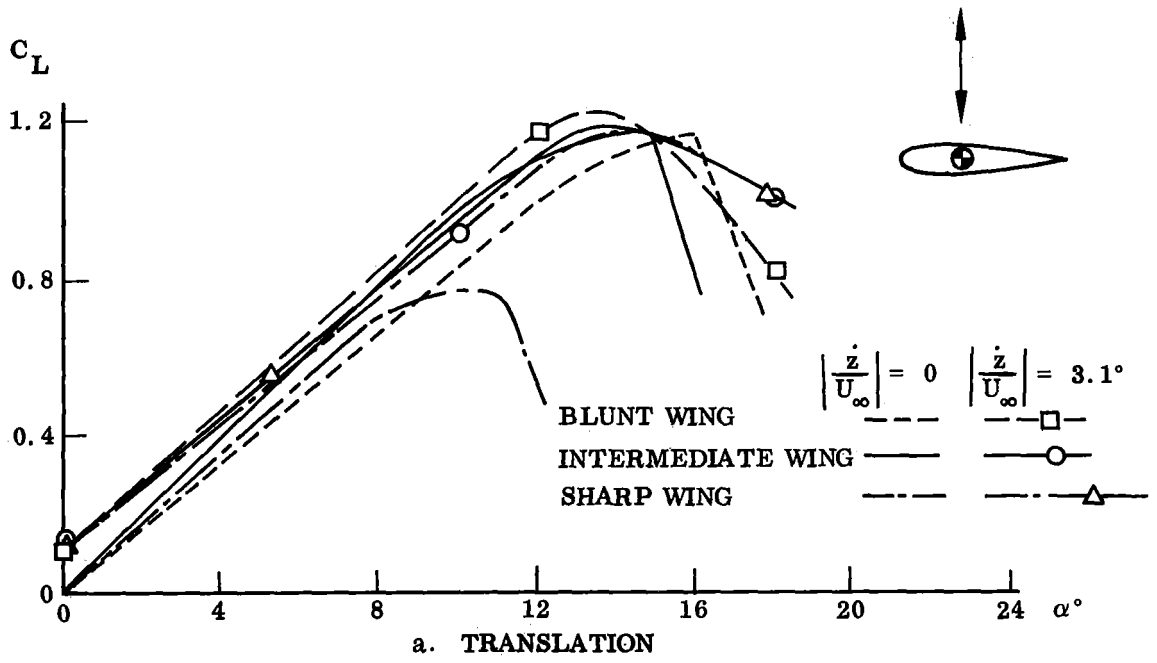

a. TRANSLATION

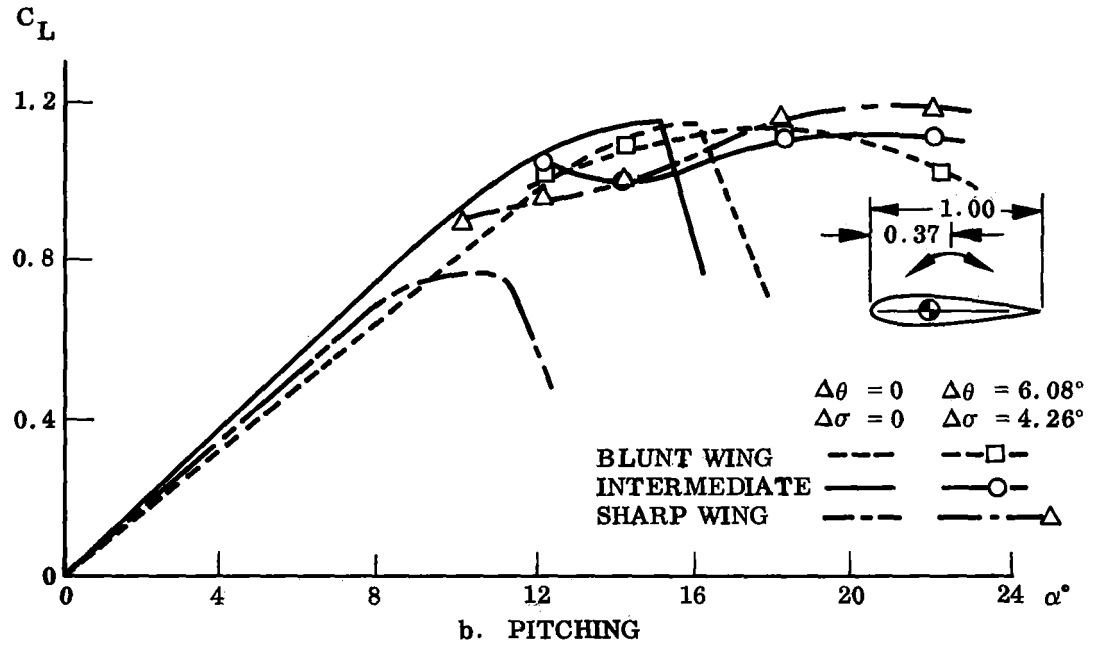

b. PITCHING

Fig. 25 Comparison Between Time Average $C_L(\alpha)$-Curves for Blunt, Intermediate, and Thin Wings at $R_c = 10^6$

of the sharp wing, which would benefit most from an energizing of the boundary layer. Thus, while the pitch rate induced nose droop may have negligible effect, the pitching induced improvement of the boundary layer profile, possibly but not necessarily equivalent to an increase of (effective) Reynolds number, can have a large effect if the nose curvature is fairly sharp.*

At stall penetration, the oscillation in pitch becomes less and less damped and may even become undamped (Fig. 21). This is caused by accelerated flow and time lag effects which will be elaborated on in Sections 3 and 4. Carta shows the same type loops for the normal force and pitching moment, and shows how the corresponding unsteady aerodynamic characteristics affect the normal force variation with time of a compressor blade (Ref. 1 and Fig. 26), and the pitch damping or blade stall of a helicopter rotor (Ref. 32 and Fig. 27). By defining a "stall closeness parameter," $\alpha_{mean}/\alpha_{stall}$, and accounting for the different locations of oscillation centers (25% and 37% cord) Carta finds his damping in pitch data to agree rather well with the results obtained by Halfman et al. (Ref. 3).

The delay or overshoot of the static stall for oscillating airfoils was observed early. In 1936 Studer (Ref. 33) suggested that the stall was delayed to the "end of the upstroke," i.e., to $\alpha = \alpha_{max}$, when the airfoil was oscillating about the static stall point, $\alpha_{mean} = \alpha_{stall}$. (This may be close to the truth for high pitch rates.) Reattachment would occur at an angle below the static stall value $\alpha < \alpha_{stall}$. In this manner a hysteresis loop would be generated at stall (in addition to the regular dynamic hysteresis). Mendelson (Ref. 34) introduces the phase lag ϕ between force or moment and the pitch rate induced velocity vector and neglects the amplitude modulation, i.e., uses the static amplitude, strictly valid for $\bar{\omega} \to 0$. (This comes very close to our quasi-steady treatment with lumped time-history effects, Section 3 and Refs. 6 and 7.) Mendelson relates the phase lag ϕ to the loss of lift slope at stall (see Section 4 for further discussion).

---

*Halfman et al. used these time average unsteady curves and a semi-empirical extension of attached flow theory to predict unsteady stall and associated undamping.

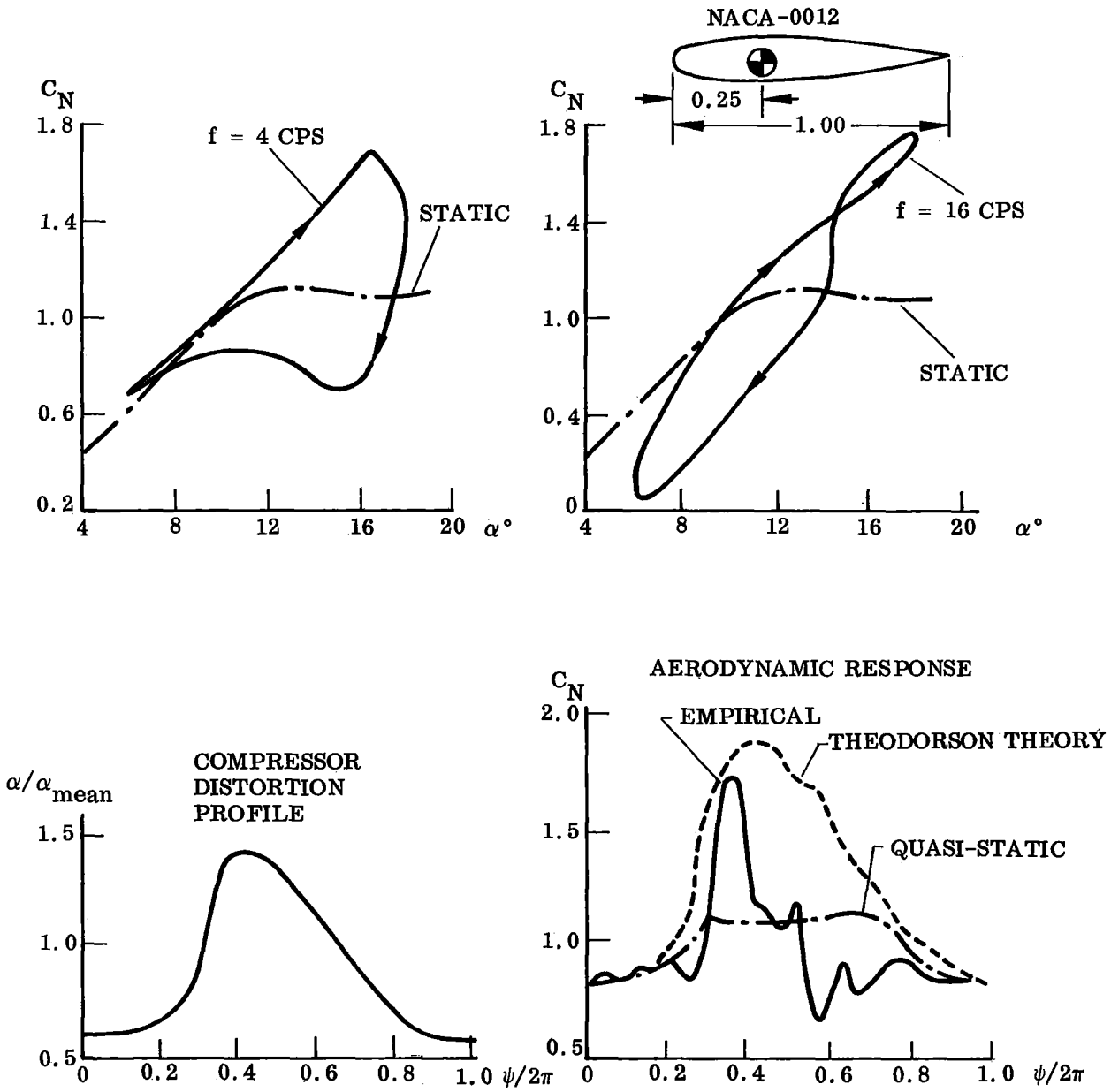

Fig. 26 Dynamic Airfoil C_N-Stall and Compressor Blade Response

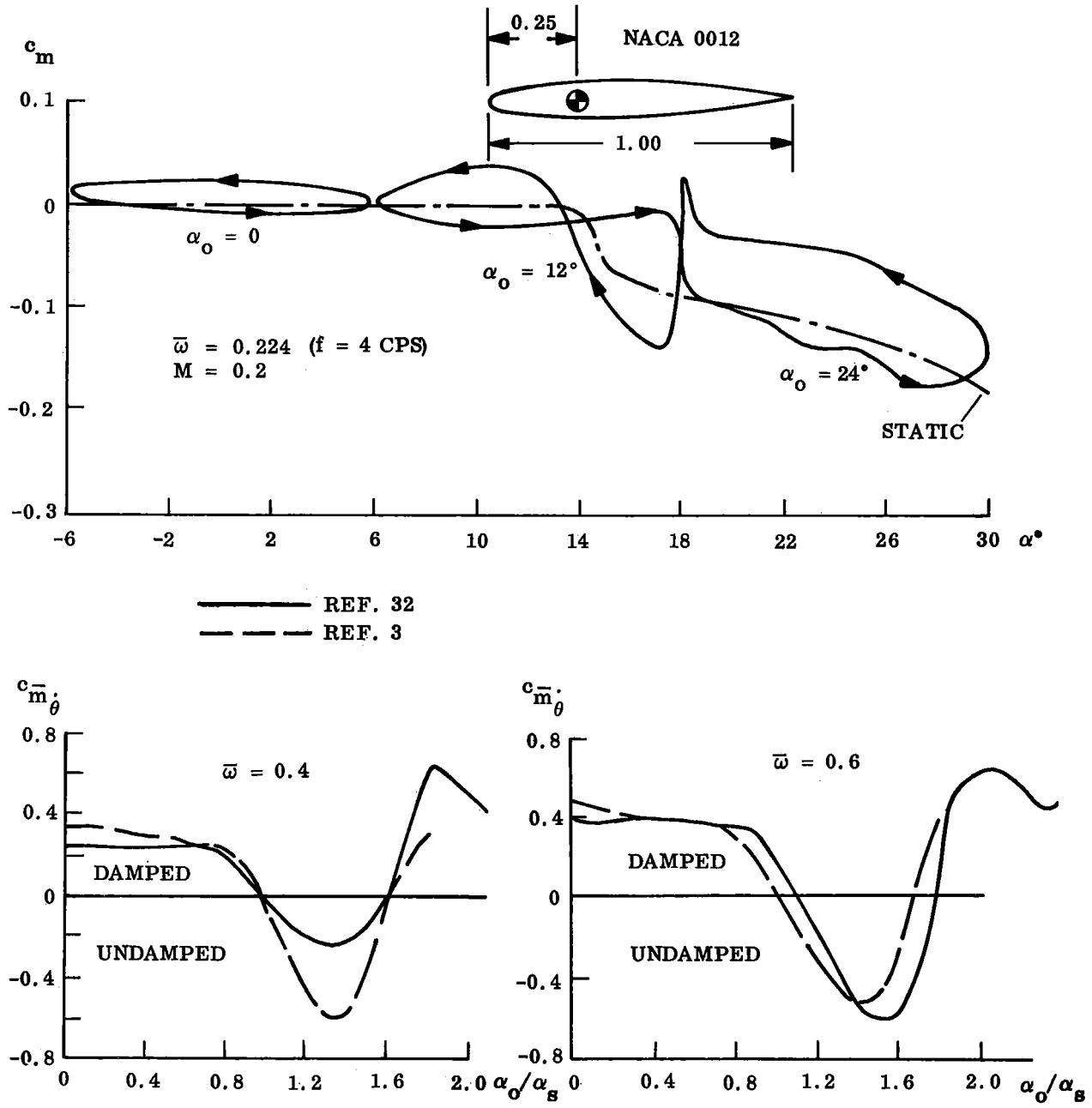

Fig. 27 Dynamic Airfoil c_m-Stall and Effective Damping Derivatives

Ham and Young (Ref. 35) describe the delayed dynamic stall and the resulting stall flutter. They do not consider the accelerated flow effect or any initial delay of flow separation, but ascribe the dynamic stall overshoot to the effect of the "spilled" concentrated vortex at separation. (Possibly this is the reason for their unconcern about profile shape; no information given.) The fact that a trip at 10% cord had no effect on the characteristics at $R_c = 0.4 \times 10^6$ is probably a result of centrifugal forces stabilizing the boundary layer more than the turbulence from previous revolution destabilized it. Static tests showed natural transition at mid-cord, and transition at 10% cord when a masking tape with sawtooth leading edge plan form was used as a trip. Their concern with Reynolds number makes it almost certain that thin airfoil stall is not the stall pattern of concern. That is, one has to be aware of possible change of stall pattern as well as of the general delay of separation. That would explain their finding that a critical reduced frequency existed, above which unstable hysteresis loops were produced.

Ham and Young show with fluctuating pressure measurements that "the spilled vortex" generates a large statically stabilizing moment, which, due to the phasing to the oscillatory motion, is dynamically destabilizing and gives rise to limit cycle torsional blade oscillations (Fig. 28). However, the sudden occurrence and gradual disappearance of frequency dependent lag effects is not explained by the spilled vortex alone. The sudden appearance of large moment effects at $\bar{\omega} > 0.2$ could be due to sudden occurrence of leading edge stall, the pitch rate induced leading edge turbulence being the triggering factor (see discussion of Fig. 24). As the frequency is increased the spilled vortex from previous blade (rotation) and its field starts decreasing the suction peaks over the airfoil.

Liiva and Davenport (Ref. 36) suggest the use of an effective angle of attack that lags the instantaneous angle of attack on the upstroke (Fig. 29). They contribute the lag ($\Delta\alpha = - C_3 \, d\alpha/dt$) to "the effective camber due to pitch rate which postpones leading edge separation." As has been shown earlier in the present report, it is the nose droop part only of the pitch rate induced camber that postpones stall, and that effect accounts only for a few percent of the experimentally observed dynamic stall overshoot.

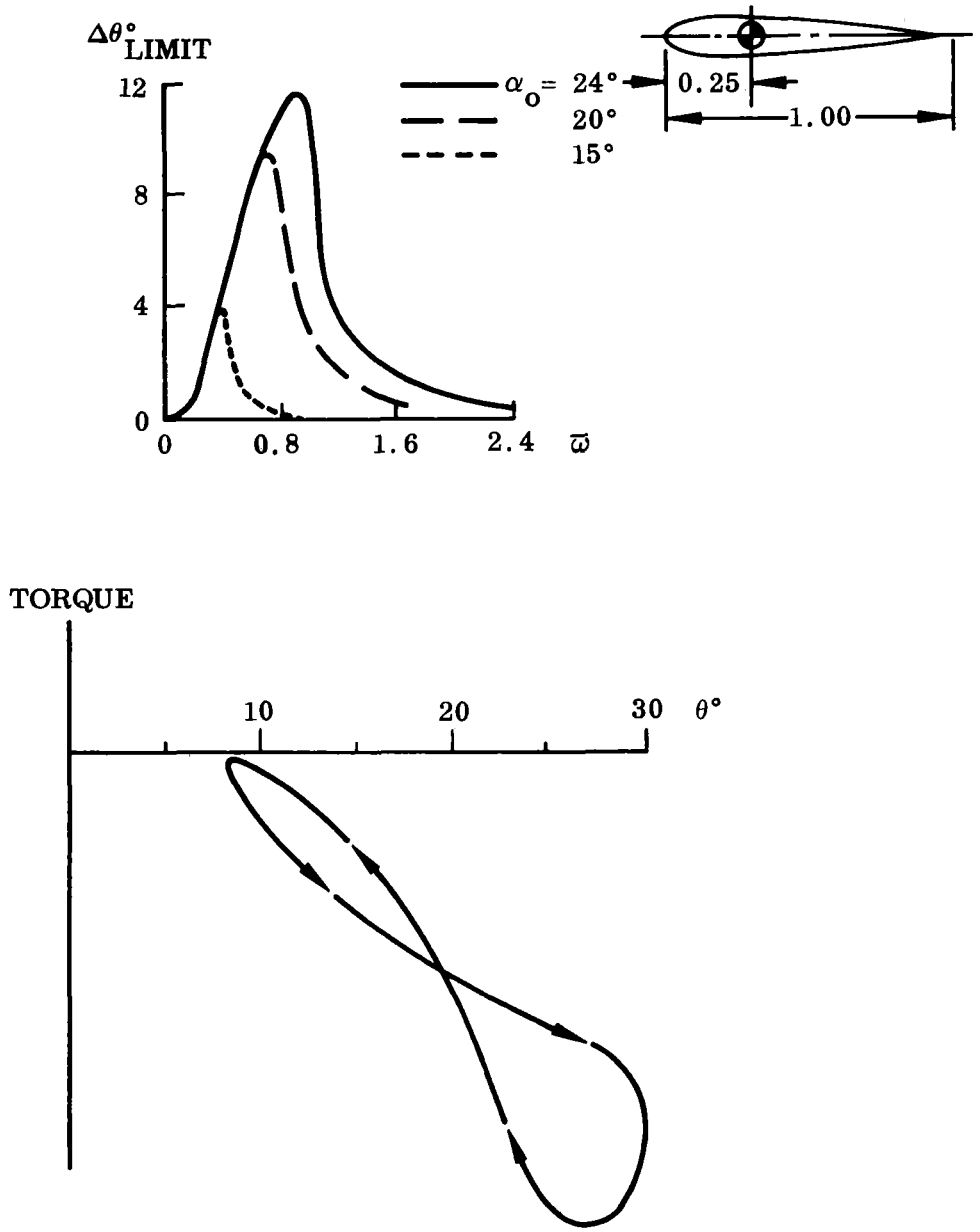

Fig. 28 Dynamic Airfoil C_m-Stall and Torsional Limit Cycle Oscillations

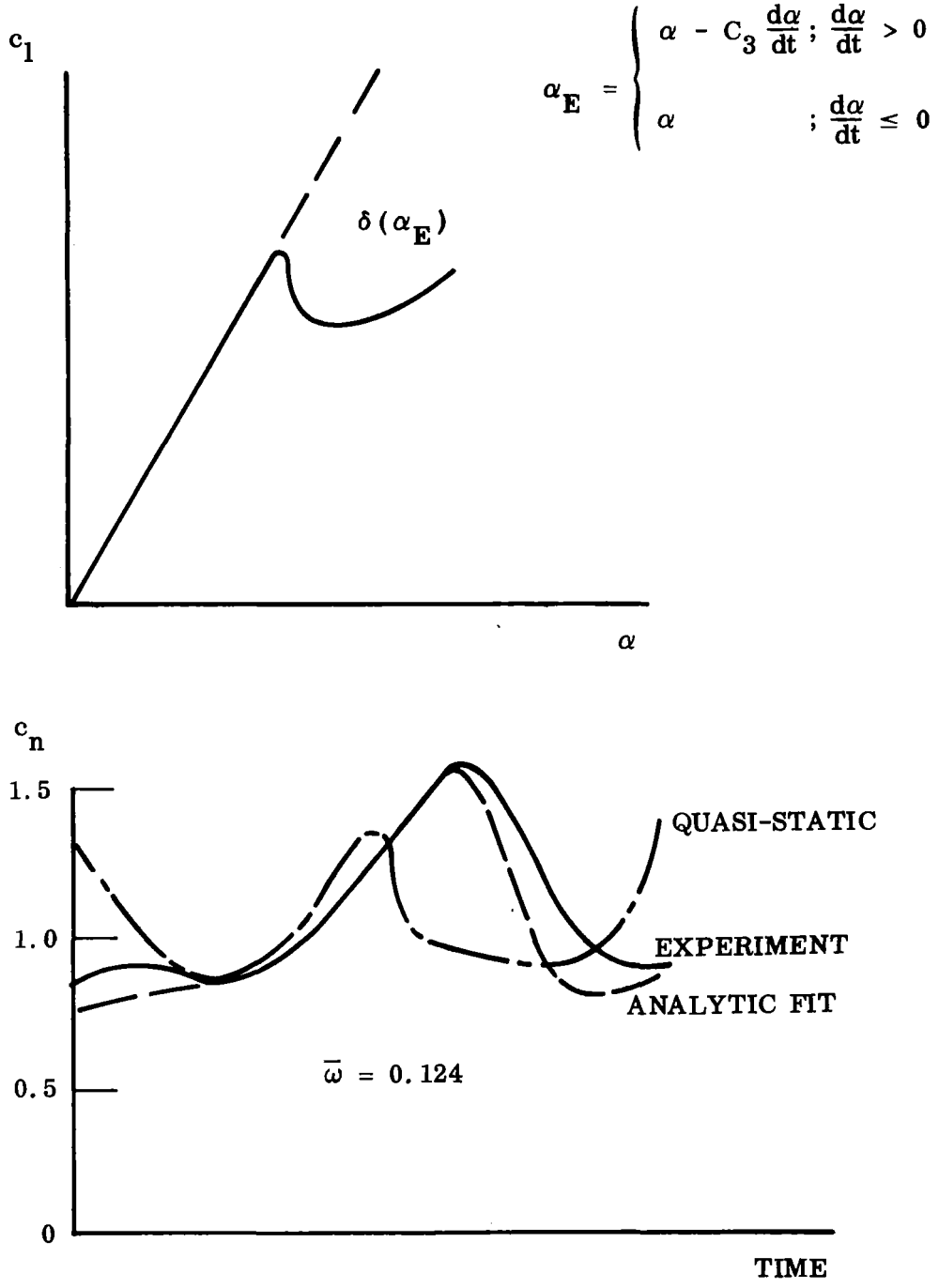

Fig. 29 Liiva's Time Lag Concept and Corresponding Fit of Experimental Dynamic Data

Nevertheless, the assumed proportionality of the lag to the pitch rate holds also for the accelerated flow effect, and it is not surprising that Liiva and Davenport are able to describe the dynamic stall characteristics rather well by using their analytic concept. In opposition to Studer, they do not consider any delay in the flow reattachment process. This must, of course, be included, especially in view of the fact that even at zero pitch rate a delay of reattachment is observed (Figs. 9 and 10).

Section 3
ANALYTIC THEORY FOR UNSTEADY AIRFOIL CHARACTERISTICS

The unsteady airfoil characteristics will be derived using quasi-steady theory in which the time history is represented by one discrete past time event. We will first develop this quasi-steady lumped-time-history theory for angles of attack below stall, and will then extend the theory to include the dynamic effects of stall following through on the hints given in the previous sections.

3.1 BELOW STALL

Below stall the classic treatment by von Karman and Sears (Ref. 37) will be used as the exact theory with which to compare quasi-steady time-lagged theory. In the von Karman-Sears theory, the effect of the airfoil wake is represented by a continuous vortex sheet with the vorticity related to the instantaneous variation of the "lifting surface" vorticity over the airfoil at earlier time instants. In Fig. 30, the "lifting surface" vorticity distribution is represented by the lifting line vortex Γ_o at 25% cord with the requirement of zero velocity normal to the airfoil at 75% cord, a "lumped vorticity" representation that has been in frequent use since Multhopp proposed its use (Ref. 38). It is immediately apparent that the downwash from unit size vortex elements in the wake upstream of $\xi = 1.25$ will give zero net downwash at 75% cord. If the reduced frequency is low, one can expect that the effect of the continuous vortex wake can be approximated by one discrete "spilled" vortex (located downstream of $\xi = 1.25$). The strength of this vortex is the difference between the strength of the lifting line vortex at an earlier time instant $\Gamma_o (t - \Delta t)$, and its present strength, $\Gamma_o(t)$.

In the Karman-Sears theory the mutual interference between vortex elements is neglected and the vortices are assumed not to move relative to their environment,

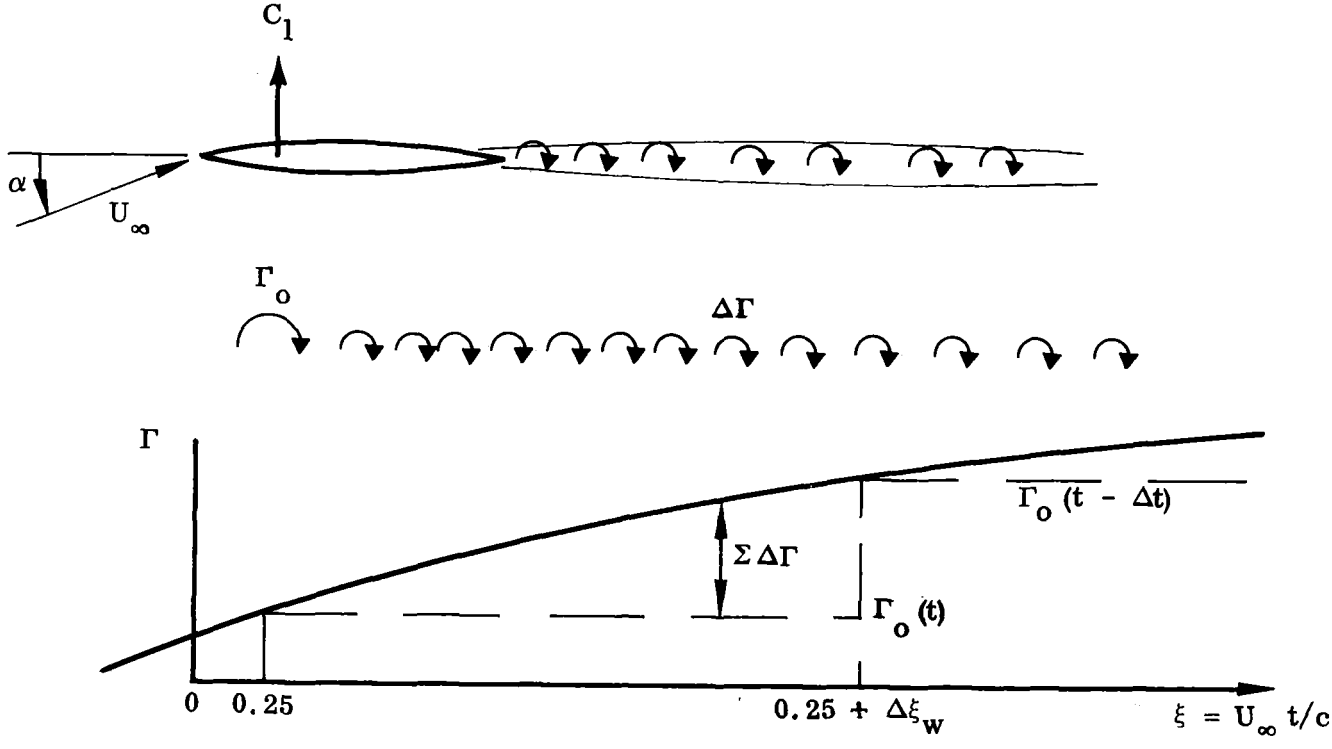

Fig. 30 Karman-Sears Vortex Wake Effects

i.e., they are transported downstream relative to the airfoil with free stream velocity. Thus, the unsteady characteristic of the airfoil can be written

$$C(t) = C(\alpha_o) + C_\alpha \left\{\theta(t) - \epsilon_\alpha \left[\theta(t) - \theta(t - \Delta t)\right]\right\} \tag{1}$$

where

$$\Delta t = c(\xi - 0.25) = c\Delta\xi_w$$

For harmonic oscillations,

$$\alpha(t) = \alpha_o + \Delta\theta \sin \omega t$$

the corresponding variation of the airfoil characteristic can be written

$$\frac{C(t) - C(\alpha_o)}{C_\alpha \Delta\theta} = \frac{A}{A_o} \sin(\omega t - \phi)$$

$$\frac{A}{A_o} = \left\{\left[1 - \epsilon_\alpha (1 - \cos\Delta\phi)\right]^2 + \left[\epsilon_\alpha \sin\Delta\phi\right]^2\right\}^{1/2}$$

$$\phi = \arctan\left[\frac{\epsilon_\alpha \sin\Delta\phi}{1 - \epsilon_\alpha (1 - \cos\Delta\phi)}\right]$$

$$\Delta\phi = \omega\Delta t = \bar{\omega}\Delta\xi_w \tag{2}$$

The half circle like vector diagram obtained by Karman-Sears (Ref. 37) suggests the following values on ϵ_α and $\Delta\xi_w$

$$\epsilon_\alpha = 0.25 \quad ; \quad \Delta\xi_w = 3.$$

How this quasi-steady lumped time history theory compares with the Karman-Sears prediction is shown in Fig. 31. The results suggest the following approximation for the unsteady vortex-wake effect.

$$C(t) - C(\alpha_o) = C_\alpha \Delta\theta \frac{A}{A_o} \sin(\omega t - \phi)$$

$$\frac{A}{A_o} = \begin{cases} 1 & : \bar{\omega} < 0.2 \\ 0.5\left[1 + (10\bar{\omega})^{-1}\right] & : \bar{\omega} \geq 0.2 \end{cases}$$

$$\phi = \begin{cases} 0.75\,\bar{\omega} & : \bar{\omega} < 0.2 \\ 14^\circ & : \bar{\omega} \geq 0.2 \end{cases} \qquad (3)$$

The low-frequency results agree very well with the time lag assumed for the boundary layer growth before separation (Ref. 27).

All generation of circulation-lift has this vortex-wake effect. An airfoil pitching around an oscillation center $\xi_{CG} = \xi_o$, which also describes translatory oscillations, has the following component characteristics:

$$\begin{aligned} C(t) = C(\alpha_o) &+ C_\alpha \left\{\theta(t) - \epsilon_\alpha \left[\theta(t) - \theta(t - \Delta t)\right]\right\} \\ &+ C_\alpha \left\{\alpha\left(q(t)\right) - \epsilon_\alpha \left[\alpha\left(q(t)\right) - \alpha\left(q(t - \Delta t)\right)\right]\right\} \\ &+ C_\sigma \left\{\sigma\left(q(t)\right) - \epsilon_\alpha \left[\sigma\left(q(t)\right) - \sigma\left(q(t - \Delta t)\right)\right]\right\} \\ &+ C_\alpha \left\{\alpha\left(\dot{z}(t)\right) - \epsilon_\alpha \left[\alpha\left(\dot{z}(t)\right) - \alpha\left(\dot{z}(t - \Delta t)\right)\right]\right\} \end{aligned} \qquad (4)$$

θ, $\alpha(q)$, $\sigma(q)$, and $\alpha(\dot{z})$ as defined in Fig. 32, are

$$\begin{aligned} \theta(t) &= \Delta\theta \sin \omega t \\ \alpha\left(q(t)\right) &= (0.5 - \xi_o)\,\bar{\omega}\Delta\theta \cos \omega t \\ \sigma\left(q(t)\right) &= \bar{\omega}\Delta\theta \cos \omega t \\ \alpha\left(\dot{z}(t)\right) &= \omega\Delta\xi \cos(\omega t + \nu) \end{aligned} \qquad (5)$$

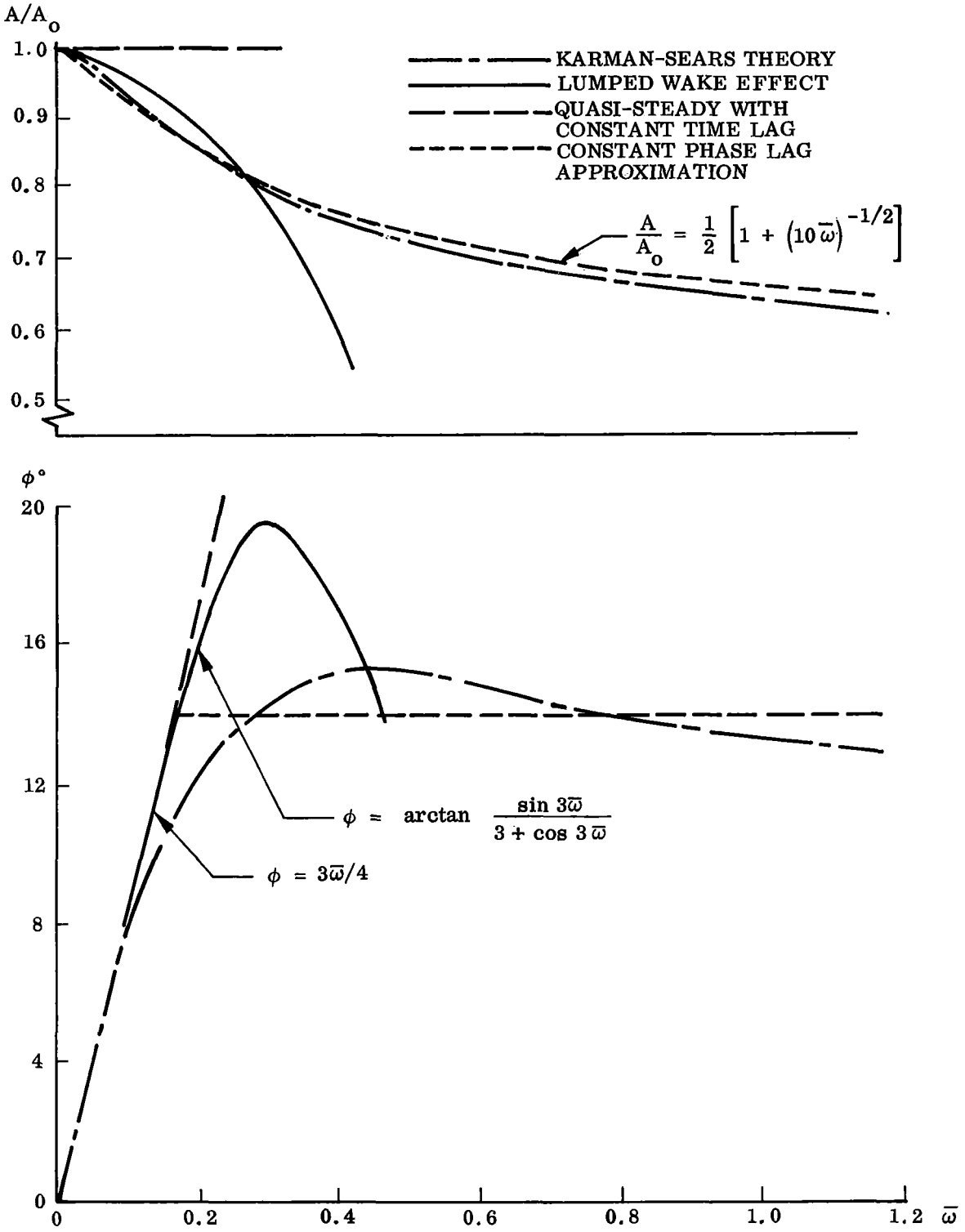

Fig. 31 Comparison Between Quasi-Steady Lumped-Time History Treatment and Exact Theory for Vortex Wake Effects Below Stall

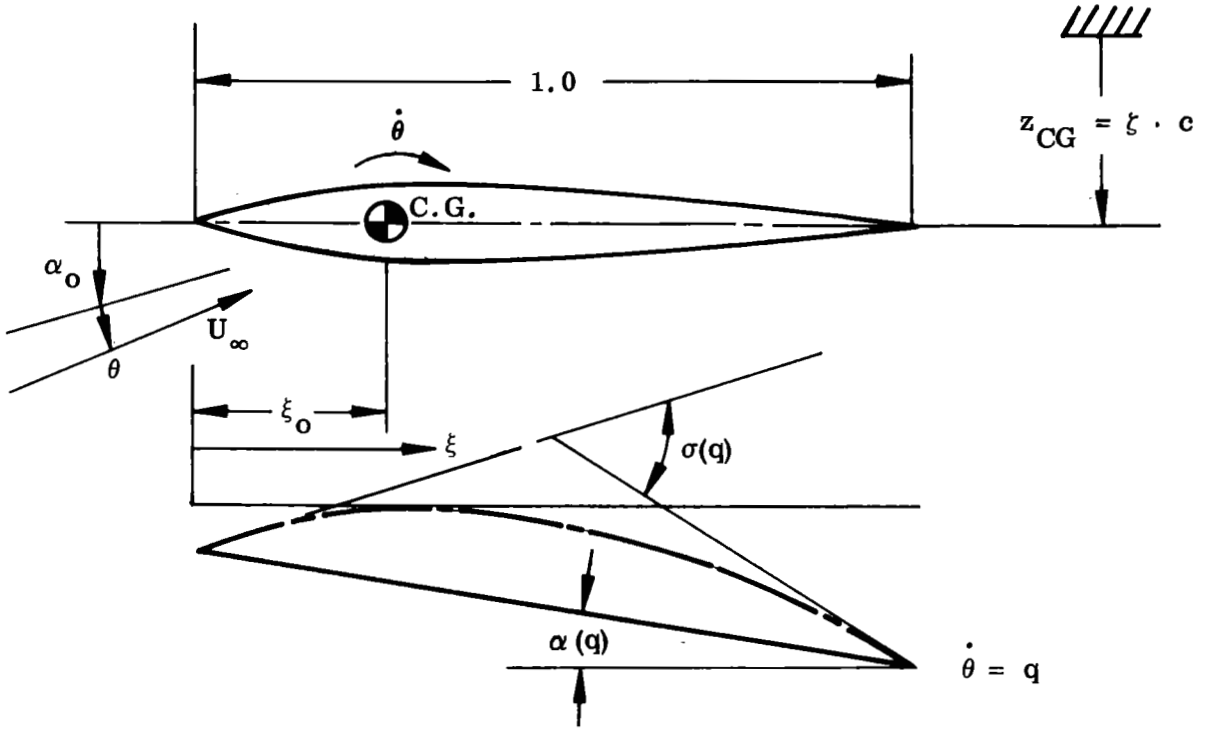

$$\alpha(q) = (0.5 - \xi_o)\frac{c\dot{\theta}}{U_\infty}$$

$$\sigma(q) = \frac{c\dot{\theta}}{U_\infty}$$

$$\alpha(\dot{z}) = \frac{\dot{z}_{CG}}{U_\infty} = \frac{c\dot{\zeta}}{U_\infty}$$

$$\theta(t) = \Delta\theta \sin \omega t$$

$$\zeta(t) = \Delta\zeta \sin(\omega t + \Delta\phi)$$

Fig. 32 Definition of Perturbations θ, α (q), σ (q), and α ($\dot{z}$)

In addition to these time lagged characteristics there are the instantaneous apparent mass effects

$$C_L(\ddot{z}) = \frac{\pi}{2}\frac{c^2\ddot{\zeta}}{U_\infty^2}$$

$$C_m(\ddot{z}) = -\frac{\pi}{2}\left(\xi_o - \frac{1}{2}\right)\frac{c^2\ddot{\zeta}}{U_\infty^2}$$

$$C_L(\ddot{\theta}) = -\frac{\pi}{2}\left(\xi_o - \frac{1}{2}\right)\frac{c^2\ddot{\theta}}{U_\infty^2}$$

$$C_m(\ddot{\theta}) = -\frac{\pi}{2}\left[\left(\xi_o - \frac{1}{2}\right)^2 + \frac{1}{16}\right]\frac{c^2\ddot{\theta}}{U_\infty^2} \qquad (6)$$

Two special cases are of particular interest, viz., pure translations and pure oscillations in pitch.

Translatory oscillations $z(t) = c\Delta\zeta \sin \omega t$

$$C_L(t) - C_L(\alpha_o) = C_{L_\alpha}\,\bar{\omega}\Delta\zeta\left(\frac{B}{B_o}\right)\cos(\omega t - \psi)$$

$$\frac{B}{B_o} = \frac{A}{A_o}\cos\phi\sqrt{1 + \left(\tan\phi - a_1\right)^2}$$

$$\tan\psi = \tan\phi - a_1$$

$$a_1 = \frac{\pi}{2}\frac{\bar{\omega}}{C_{L_\alpha}}\sqrt{\frac{A}{A_o}}\cos\phi \qquad (7)$$

$$C_m(t) - C_m(\alpha_o) = -C_{L_\alpha} \bar{\omega} \Delta\xi (0.5 - \xi_o) \left(\frac{B}{B_o}\right) \cos(\omega t - \psi)$$

$$\frac{B}{B_o} = \frac{A}{A_o} \cos\phi \sqrt{a_2^2 + \left(a_2 \tan\phi - a_1\right)^2}$$

$$\tan\psi = \tan\phi - \frac{a_1}{a_2}$$

$$a_2 = (0\ 25 - \xi_o)/(0.50 - \xi_o) \tag{8}$$

Pure oscillations in pitch: $\theta = \Delta\theta \sin \omega t$

$$C_L(t) - C_L(\alpha_o) = C_{L_\alpha} \Delta\theta \frac{B}{B_o} \cos(\omega t - \psi)$$

$$\frac{B}{B_o} = \frac{A}{A_o} \cos\phi \sqrt{\left(b_1 - \tan\phi\right)^2 + \left[b_1 \tan\phi + 1 - a_3\right]^2}$$

$$\tan\psi = (b_1 \tan\phi + 1 - a_3)/(b_1 - \tan\phi)$$

$$b_1 = \left(0.5 - \xi_o + \frac{C_{L_\sigma}}{C_{L_\alpha}}\right) \bar{\omega}$$

$$a_3 = a_1 (0.5 - \xi_o) \bar{\omega} \tag{9}$$

$$C_m(t) - C_m(\alpha_o) = C_{L_\alpha} \Delta\theta\,(0.5 - \xi_o)\left(\frac{B}{B_o}\right)\cos(\omega t - \psi)$$

$$\frac{B}{B_o} = \frac{A}{A_o}\cos\phi\sqrt{\left(b_2 - a_2\tan\phi\right)^2 + \left(b_2\tan\phi + a_2 - a_4\right)^2}$$

$$\tan\psi = (b_2\tan\phi + a_2 - a_4)/(b_2 - a_2\tan\phi)$$

$$b_2 = b_1 - 0.25\,\bar{\omega}$$

$$a_4 = a_3 + \frac{a_1\bar{\omega}}{16}\Big/(0.5 - \xi_o) \tag{10}$$

Equations (9) and (10) are illustrated in Figs. 33 and 34 for $\xi_o = 0.25$.

3.2 STALL PENETRATION

When and where separation occurs is determined by the boundary layer (profile) shape and the adversity of the local pressure gradient. On the pitching airfoil, the (axial) flow acceleration on the leeward side will delay the flow separation. The pressure gradient of the external flow at the boundary layer edge is given by the complete Bernoulli equation.

$$\frac{1}{\rho_e}\frac{dp_e}{dx} = \frac{\partial U_e}{\partial t} + U_e\frac{\partial U_e}{\partial x} \tag{11}$$

With $x/c = \xi$, Eq. (11) can be written

$$\frac{dp_e}{d\xi} = -\rho_e U_e\left(\frac{\partial U_e}{\partial t}\frac{c}{U_e} + \frac{\partial U_e}{\partial \xi}\right) \tag{12}$$

For constant free-stream velocity, U_e changes only through airfoil pitching. Thus

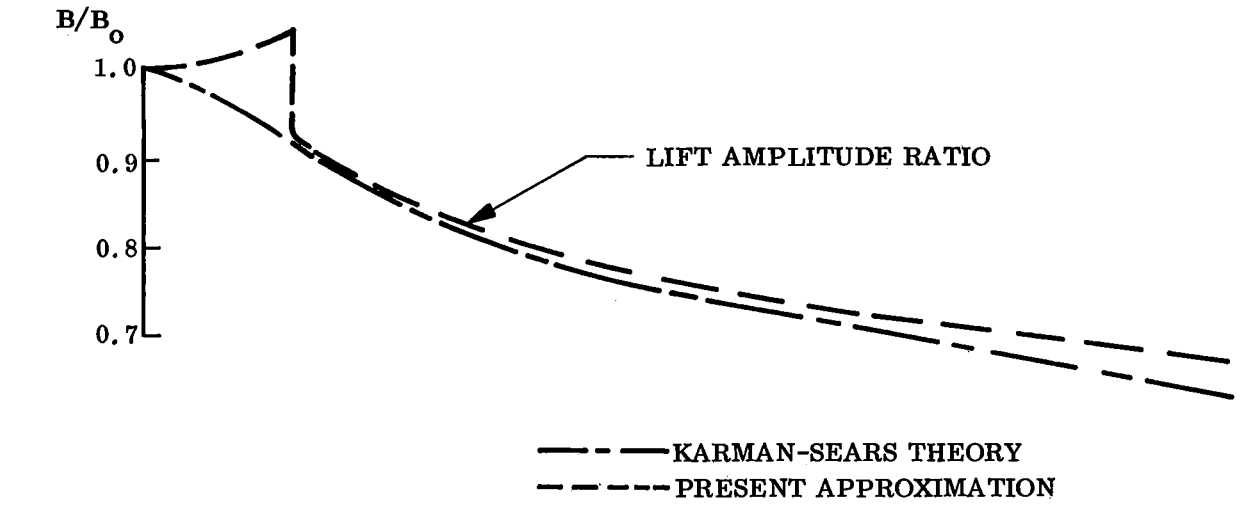

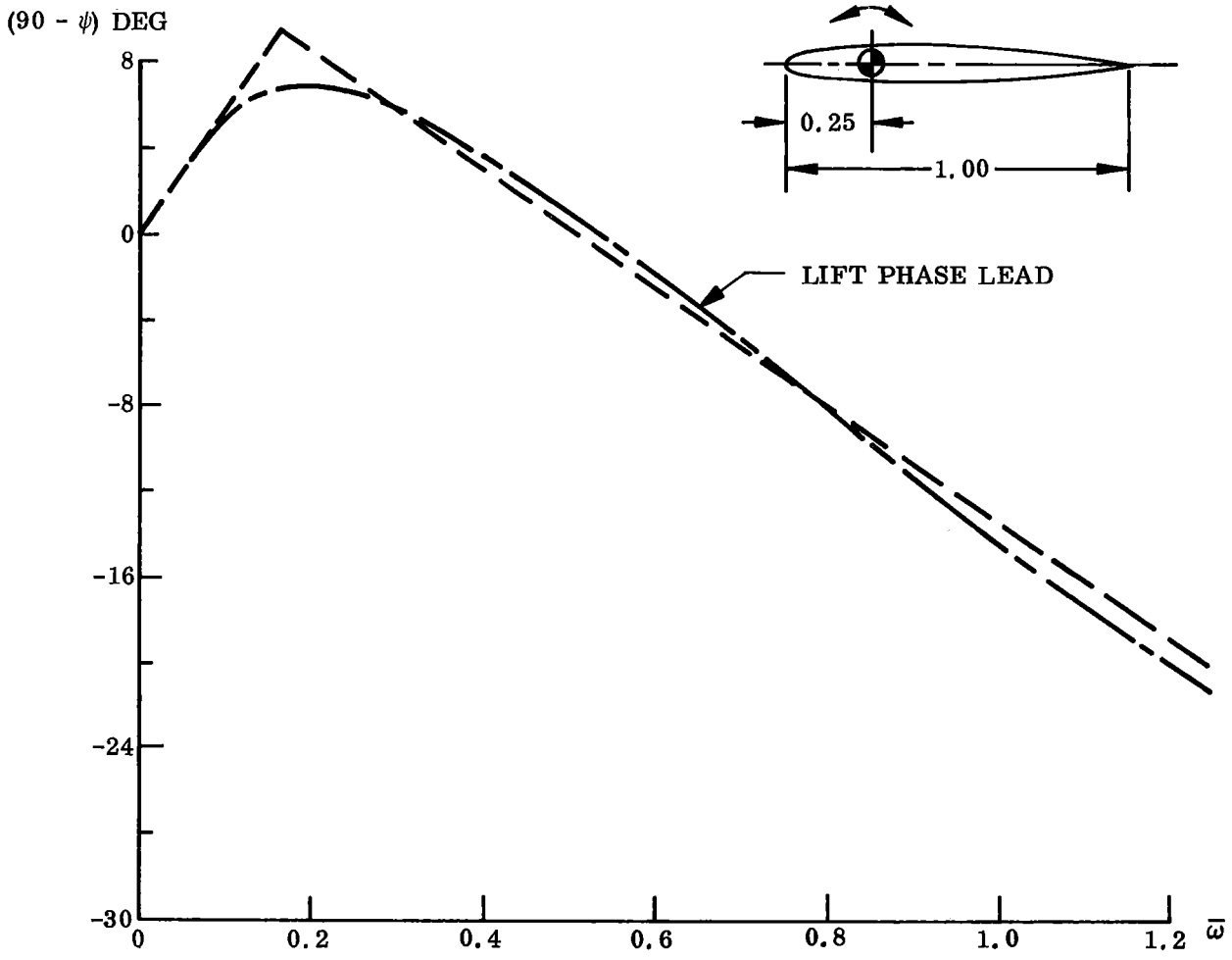

Fig. 33 Substall Dynamic Lift Characteristics for Small Amplitude Oscillations in Pitch Around Quarter Chord

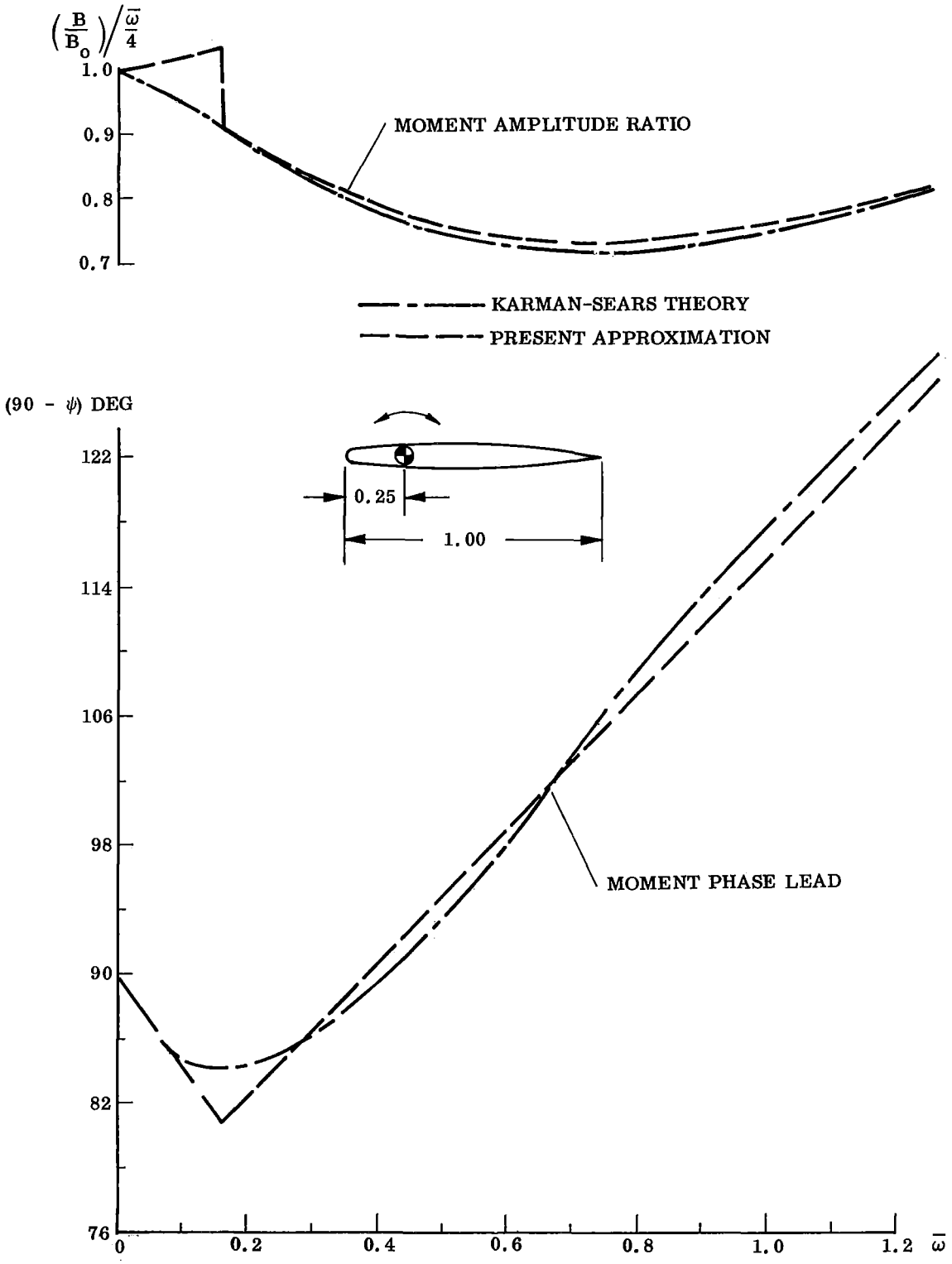

Fig. 34 Substall Dynamic Moment Characteristics for Small Amplitude Oscillations in Pitch Around Quarter Chord

$$\frac{dp_e}{d\xi} = -\rho_e U_e \left(\frac{\partial U_e}{\partial \alpha} \frac{c\dot{\alpha}}{U_e} + \frac{\partial U_e}{\partial \xi} \right) \tag{13}$$

That is,

$$\frac{dp_e}{\partial \xi} = \left(\frac{\partial p_e}{\partial \xi} \right)_{\dot{\alpha} = o} + \frac{\partial p_e}{\partial \alpha} \frac{c\dot{\alpha}}{U_e} \tag{14}$$

On the leeward side of the airfoil, $\partial p_e/\partial \alpha$ is negative, as suction increases with angle of attack. Consequently, the pressure gradient dp_e/dx is decreased on the leeward side when the airfoil pitches at a certain rate, $c\dot{\alpha}/U_e > 0$, and the boundary layer separation is, as a consequence, delayed. That is, the separation will in the unsteady case lag behind the static or steady state condition, allowing an overshoot of the stall angle of attack.

For trailing edge separation, either laminar or turbulent, this is the total lag to be added to the regular substall lag generated by the vortex-wake. However, for leading edge separation, there is a sudden, discontinuous change of the circulation which one can visualize conceptually (and physically, Ref. 35) in form of a "spilled vortex" (Fig. 35). At the time instant t_2 this spilled vortex would increase the suction over the mid-cord portion of the airfoil. This agrees with Ham's observations (Ref. 39 and Fig. 36). At a later time, t_3 in Fig. 35, when the vortex has moved downstream towards the trailing edge, a double peaked pressure distribution would result, which is the load distribution shown by Ham (Ref. 39 and Fig. 36)

Judging by the Reynolds number, $R_c = 0.35 \times 10^6$, the NACA 0012 airfoil must have laminar trailing edge separation statically, and much of the overshoot is due to

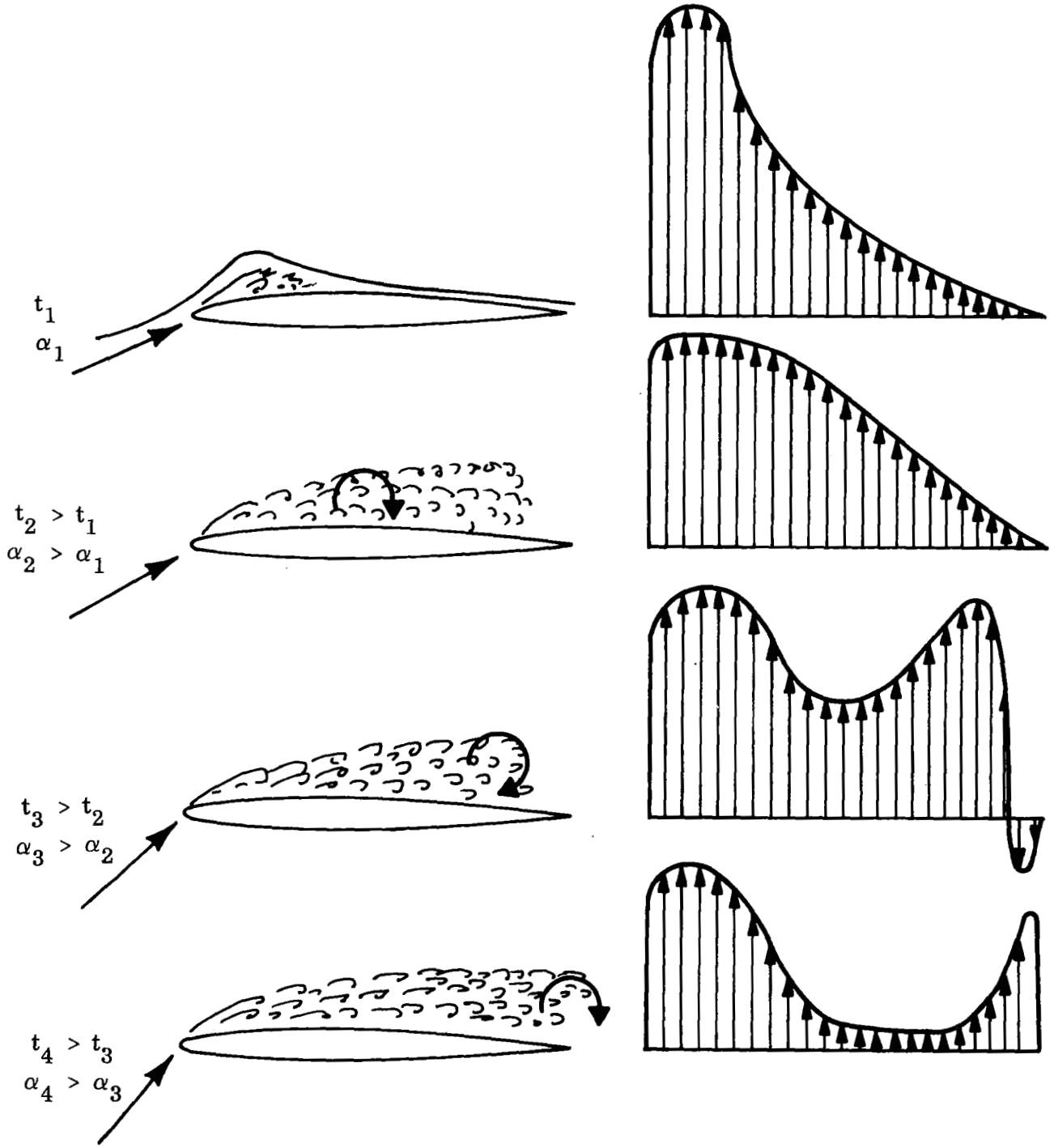

Fig. 35 Dynamic Leading Edge Stall with "Spilled" Vortex, Conceptual Picture

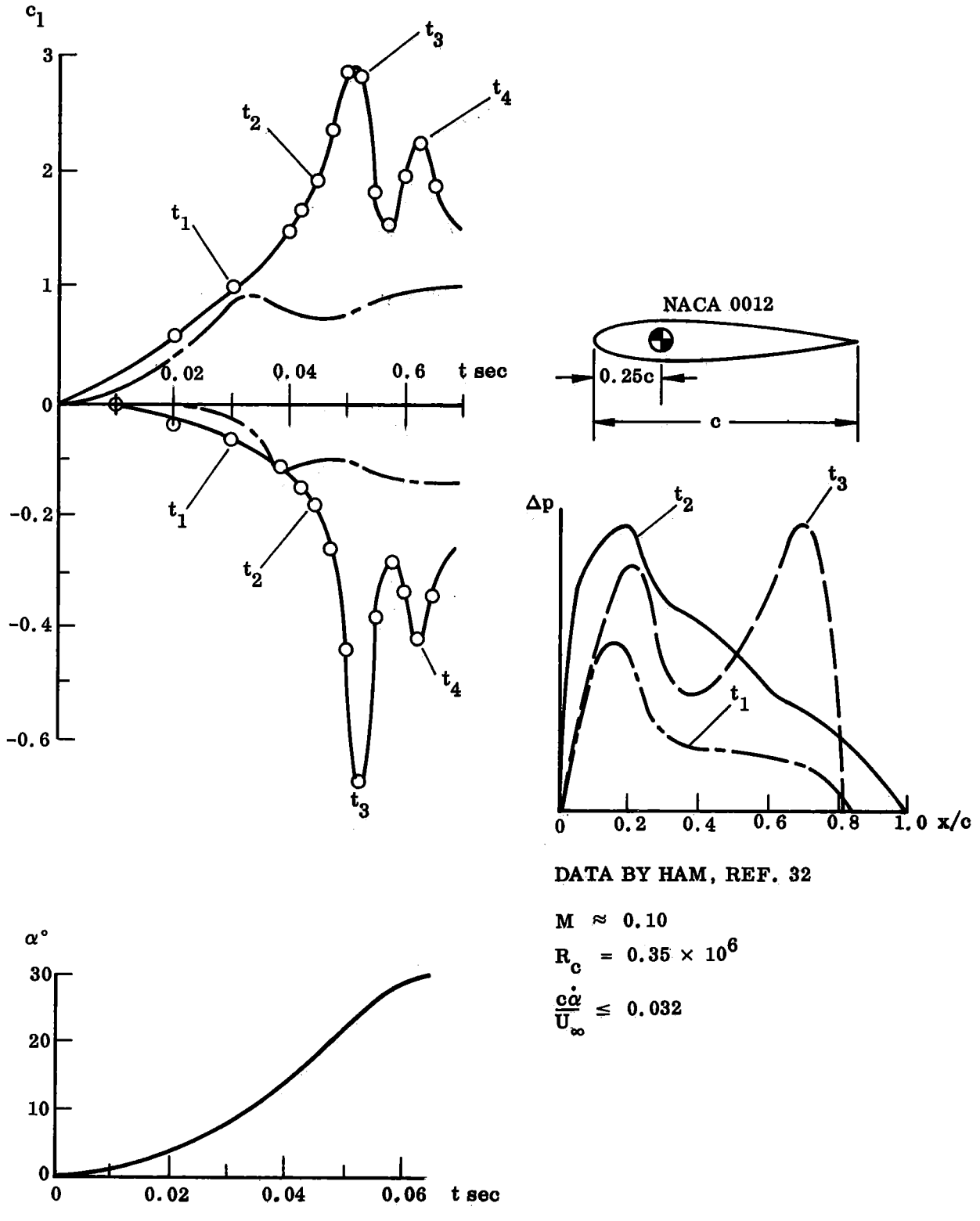

Fig. 36 Dynamic Leading Edge Stall with "Spilled" Vortex, Experimental Data

pitch rate induced switch to leading edge separation, as was discussed earlier. However, there is still a sizable overshoot of that magnitude (Fig. 37). This is caused by the "spilled" vortex. When it moves downstream over the cord, the lift (or normal force) remains relatively constant while the pitching moment changes drastically (compare $\alpha = 23.7°$ and $\alpha = 25.3°$ in Fig. 37). The spilled vortex effect seems to oscillate around the "quasi-steady" overshoot in a manner similar to the observed oscillations of shock-induced bounday-layer separations (Ref. 40). A Karman vortex sheet from a cylinder with the diameter c sin α_s would have a shedding frequency roughly twice as high as the observed reduced frequency of $\bar{\omega} \approx 2$ for the "spilled" vortex (Fig. 36).

The transient stall phenomenon for thin airfoils has been described by Sarpakaya (Ref. 41 and Fig. 38). The moment increases as long as the "long bubble" flow reattaches near the trailing edge. When this is no longer possible and trailing edge separation occurs, forming a second vortex, the moment drops off due to lost aft body or trailing edge suction. The peak c_m- magnitude increases with increasing reduced frequency. When the trailing edge vortex increases in size with increasing θ it finally causes leading edge attached flow and is spilled, causing the next c_m-peak. It appears that a few cycles of alternating vortex shedding may occur before the steady state conditions are reached. The reduced frequency of the first half-cycle of the harmonic oscillations vary from $\bar{\omega} = 1$ for $c\dot{\theta}/U_\infty = 0.11$ to $\bar{\omega} = 2.5$ for $c\dot{\theta}/U_\infty = 0.35$. The frequency increases and the amplitude decreases with increasing θ, the same nonlinear behavior observed for the shock-boundary layer interaction (Ref. 40). Sarpakaya describes this oscillation as the result of trailing-edge vortex buildup until it causes attached flow over the leading edge and sheds, whereafter the building up of trailing- and leading-edge separation vortices starts over again.

Scruggs and Morris (Ref. 42) found that a disorganized flat plate wake at $\alpha = 16°$ could be tuned using 3-deg amplitude pitch oscillations at the right frequency.

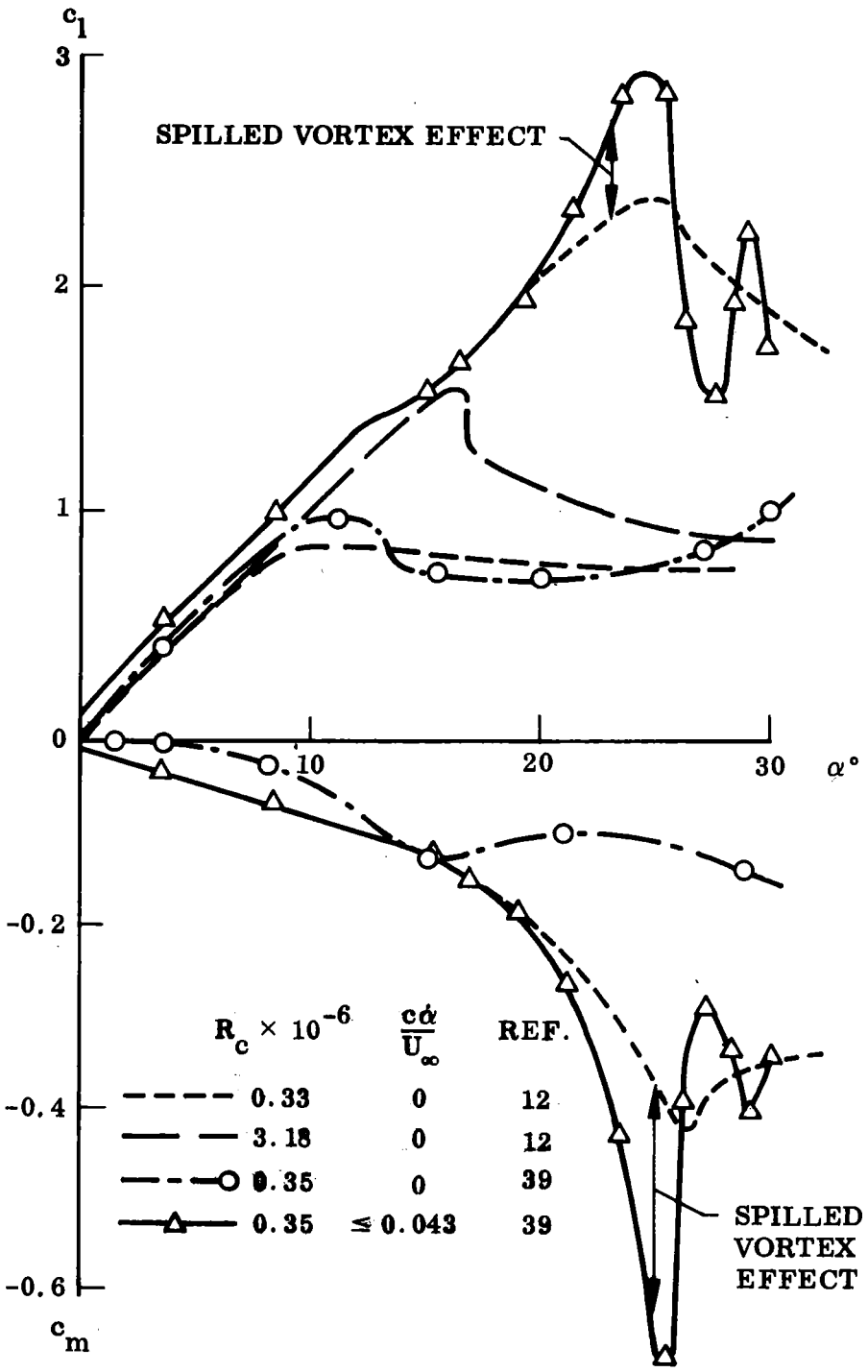

a. LIFT AND PITCHING MOMENT

Fig. 37a "Spilled" Vortex Effect on Dynamic Stall Overshoot

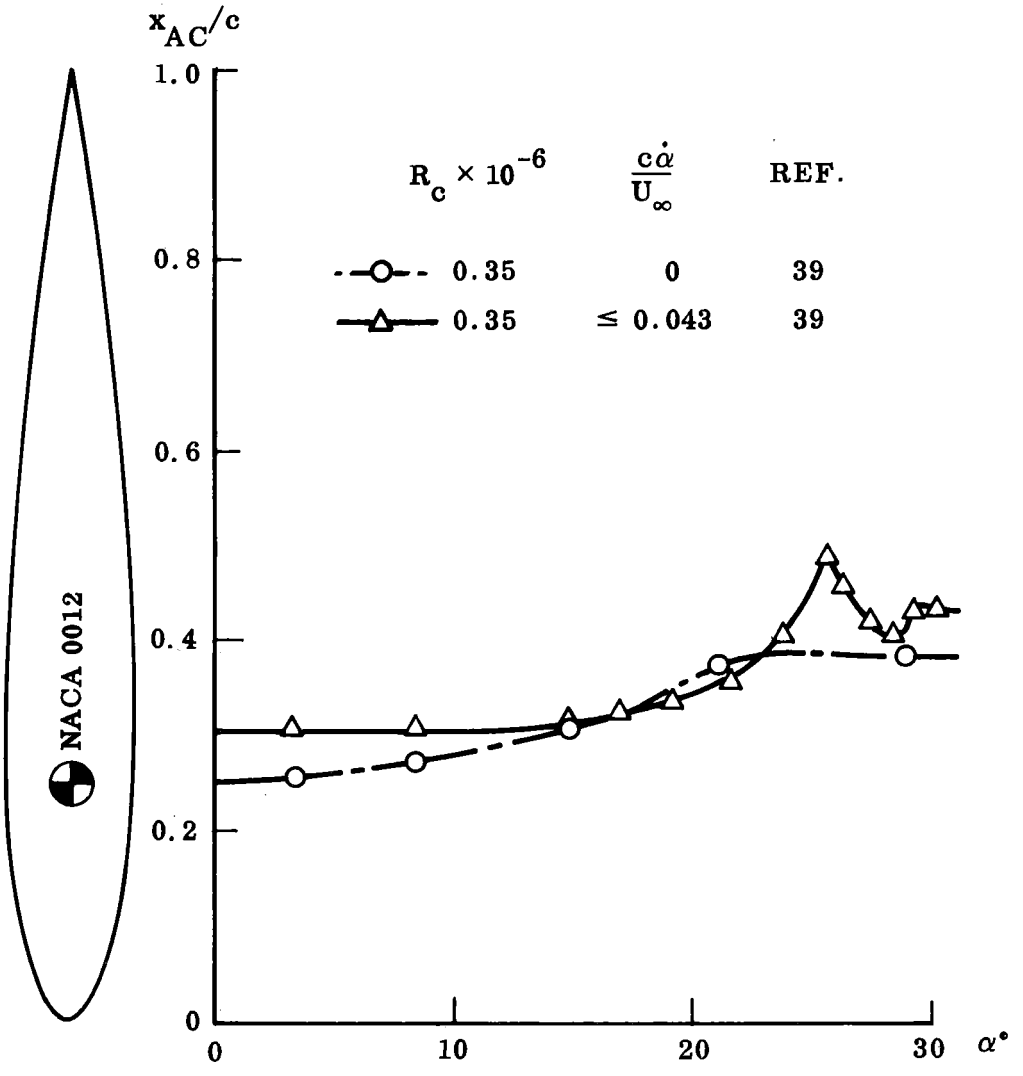

b. AERODYNAMIC CENTER

Fig. 37b "Spilled" Vortex Effect on Dynamic Stall Overshoot

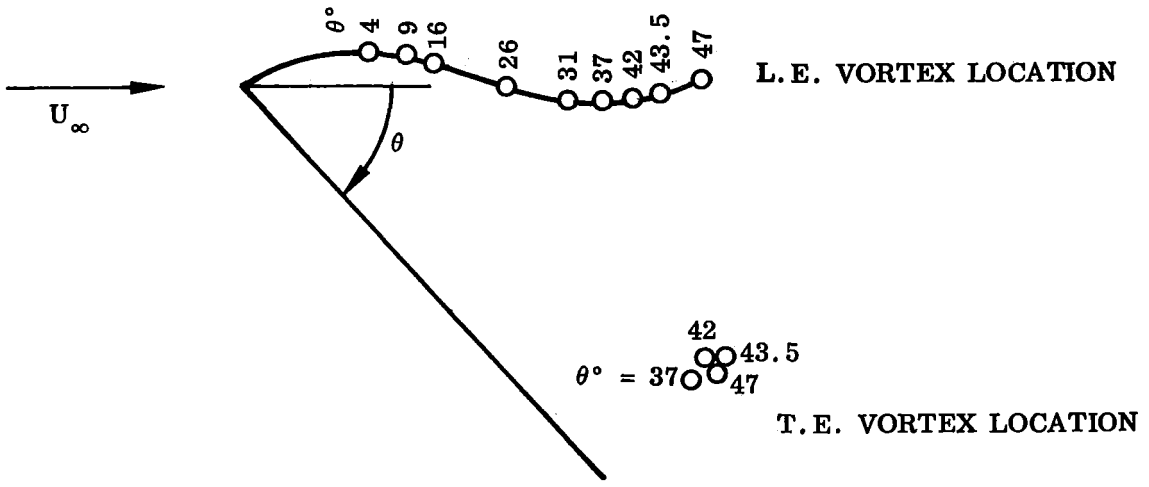

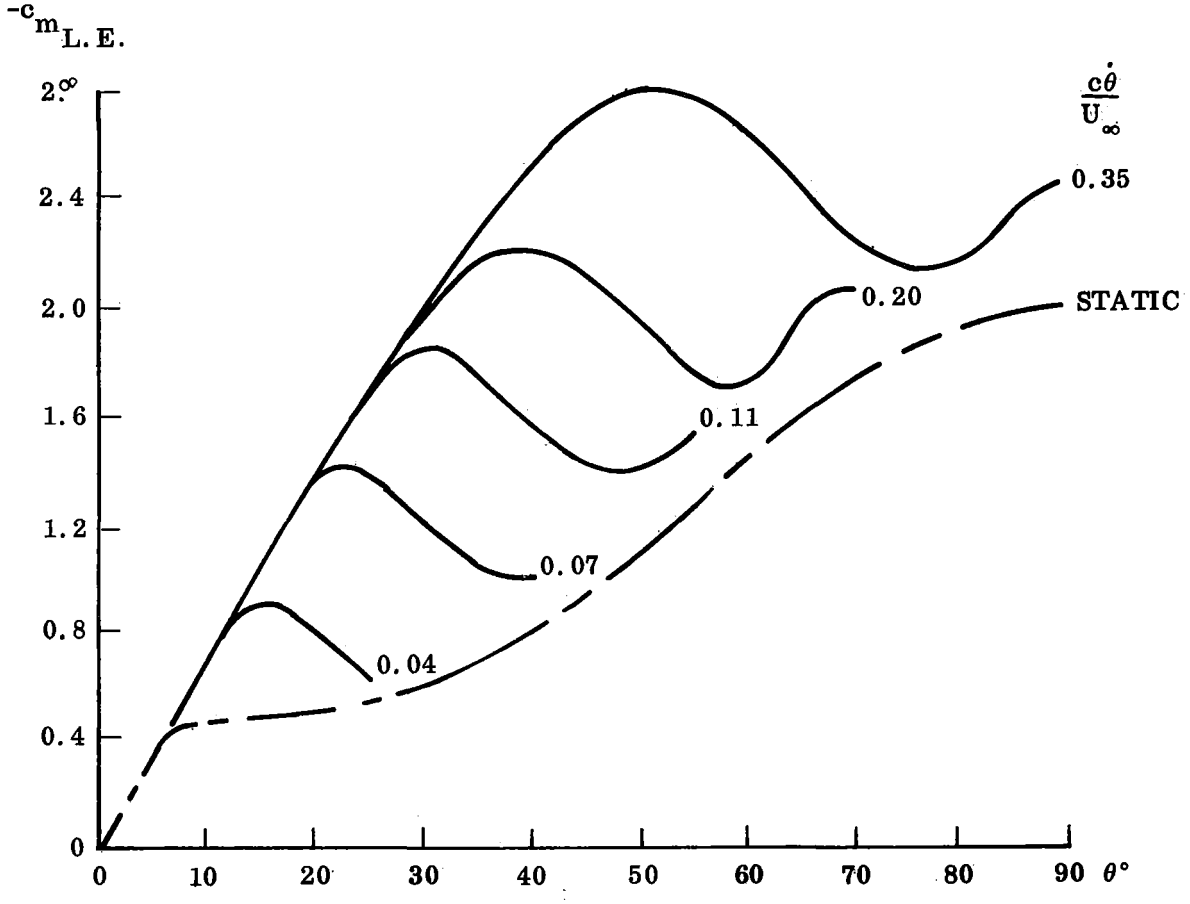

Fig. 38 Dynamic Thin Airfoil Stall, Flat Plate Data up to 90 Deg Angle-of-Attack

Viewed in this light, Ham's critical frequency (Fig. 28) may indeed be due to resonance effects. The regular Strouhal frequency for Karman vortex shedding were one order of magnitude too large and could not be blamed. However, this different type of alternating vortex shedding occurring on airfoils could cause the observed effects, although it is equally likely that a change in stall pattern is the true explanation for the sudden occurrence of limit cycle oscillations.

3.3 OSCILLATION THROUGH STALL AND STALL BUFFET EFFECTS

In oscillations through stall, the stall penetration effects, although modified by the variation of the pitch rate over the cycle, are the same in principle as those discussed in the previous section. The big difference is the addition of the reattachment process at the "backstroke." It was shown before that the flat plate characteristics would be the lower limit for the reattachment process (Fig. 11). When the pitch rate-induced effects on the "upstroke," turbulence, lessened pressure gradient adversity, etc., have caused a transition from one stall pattern to another, one can, of course, expect a switch back on the "backstroke." At low Reynolds numbers, one may even have to look out for the possibility that a leading edge stall pattern may revert to laminar trailing-edge separation on the "backstroke."

When leading edge stall is prevailing throughout the cycle, the spilled vortex phenomenon discussed earlier (Figs. 35 – 37) plays an important role. If the oscillation frequency is near the vortex shedding frequency discussed earlier, resonance type phenomena will play an important role in the generation of stall flutter. Even without resonance the spilled vortex will cause some peculiarities, such as causing earlier occurrence of moment stall, as discussed in Ref. 5. This is due to the fact that the suction peak can travel the whole cord length (Figs. 35 –37) before the lift is affected, whereas the moment is affected immediately by the changed load distribution.

The thin airfoil oscillation through stall can, of course, be dealt with using Sarpakaya's approach (Ref. 40). Ham (Ref. 43) has described such an analysis. However, it can still not predict leading-edge type oscillatory stall, as the method neglects the initial delay of separation, which Ham has himself pointed out to be an important feature (Ref. 32). The vortex theory is, of course, totally inapplicable to trailing-edge stall.

Section 4

COMPARISON BETWEEN ANALYTIC PREDICTIONS AND DYNAMIC EXPERIMENTAL RESULTS

For a check of the substall analytic assumptions, Molyneaux and Ruddlesden (Ref. 44) provide the needed detailed experimental data (Fig. 39). Data were obtained for oscillations about leading and trailing edge, the combinations of which gave the pure effects of pitch rate induced camber and frequency induced plunging (Ref. 27 and Fig. 40). $C_{L_\sigma}/C_{L_\alpha} = 0.29$ was measured compared with the thin airfoil theoretical value 0.25. The camber load distribution was close to the theoretical with a center of pressure near mid-cord. The phase angle between α- and $\dot{\alpha}$-pressure distributions was 11.4°. For the integrated lift and moment the phase angles were 9.7 and 12.1°, respectively. For the reduced frequency of the experiement, $\overline{\omega} = 0.33$, both Karman-Sears theory and our lumped-time history treatment predicts $\phi = 14°$ (Fig. 32). The translatory loading induced in a wing section through bending or flapping the wing is 25% above what would be estimated from the in phase loading in pitch. This may be due to different spanwise loadings, the airfoil section reaching two-dimensional flow conditions faster on the bending wing.

The Dutch trio – Greidanus, van de Vooren, and Bergh – "accidentally" obtained data that beautifully illustrate dynamic effects of trailing-edge separation (Ref. 45). They were performing a thorough experimental check of theories for small amplitude oscillations around $\alpha = 0$. Their model, a 7.3 percent thick symmetrical airfoil, had natural boundary-layer transition near the trailing edge if no tripping was used. Since boundary-layer transition is very similar to trailing-edge separation (see previous discussion of Ref. 20), we can expect some interesting "anomalous" results (Fig. 41). When natural boundary-layer transition is permitted to occur near the trailing edge, there are drastic variations from the expected theoretical trends, the latter being in agreement with the trip-on experimental results. The oscillation

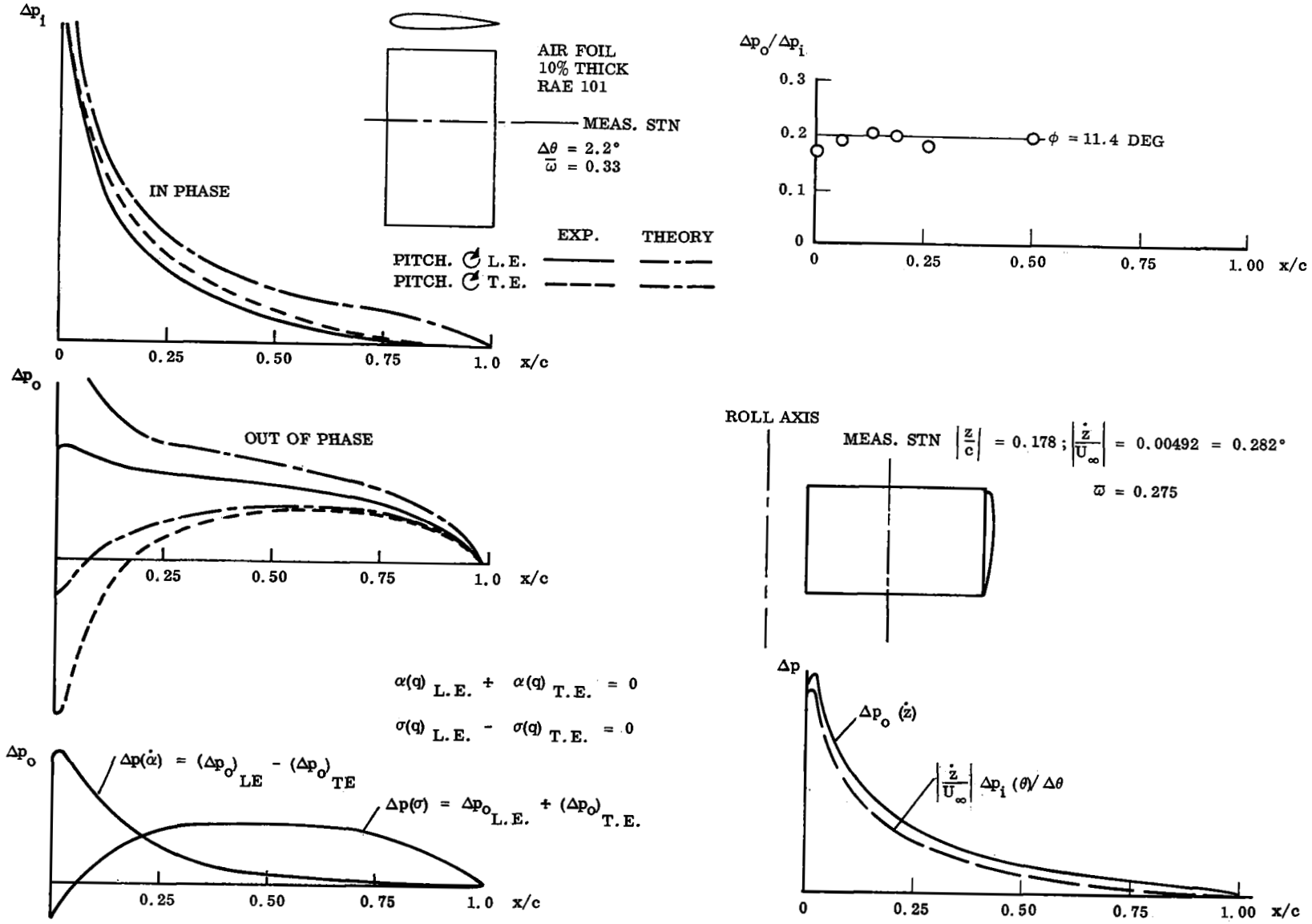

Fig. 39 In-Phase and Out-of-Phase Pressure Loads on a 10% Thick Airfoil Oscillating in Pitch and Translation at $\alpha = 0$

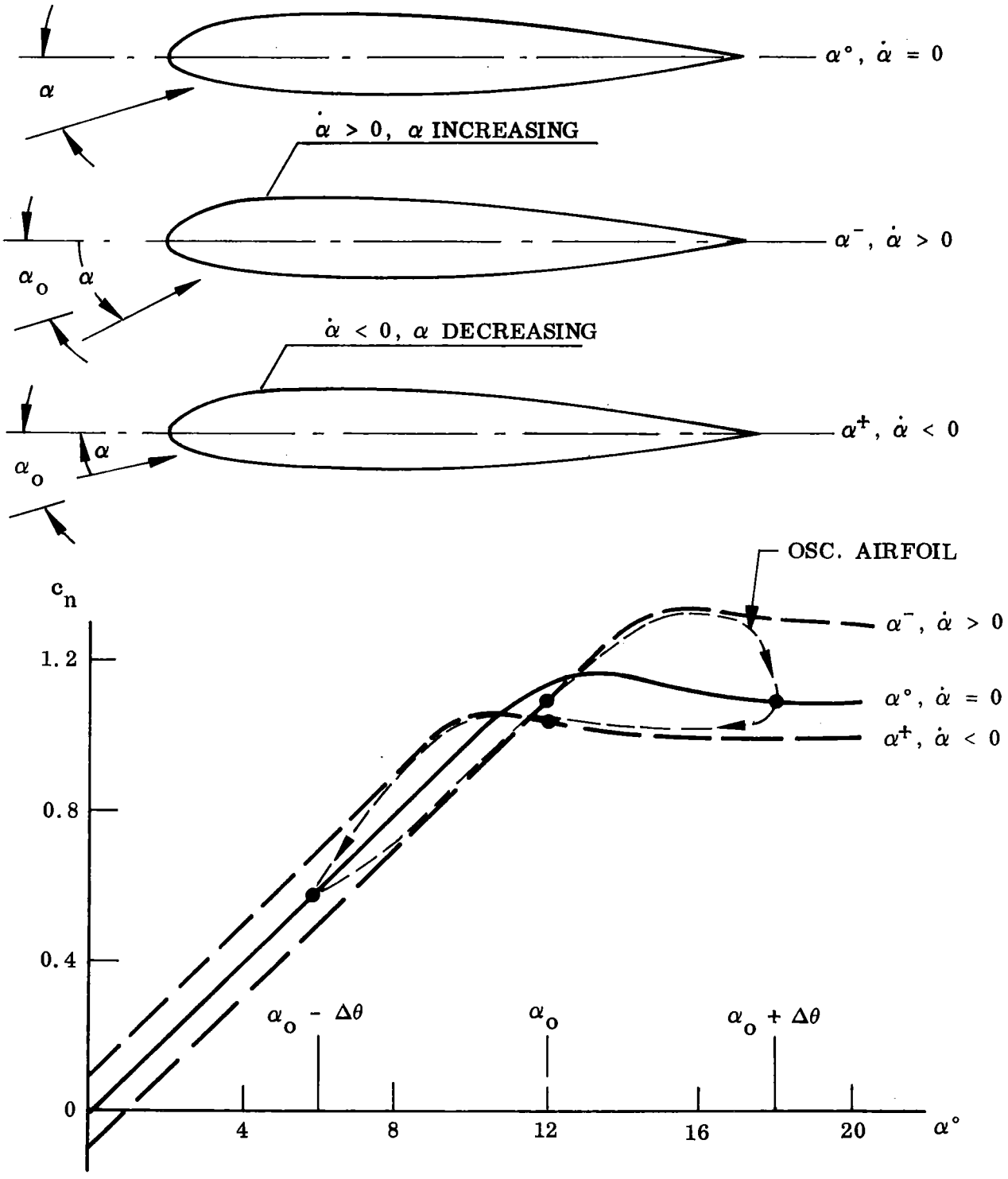

Fig. 40 Frequency-Induced Plunging

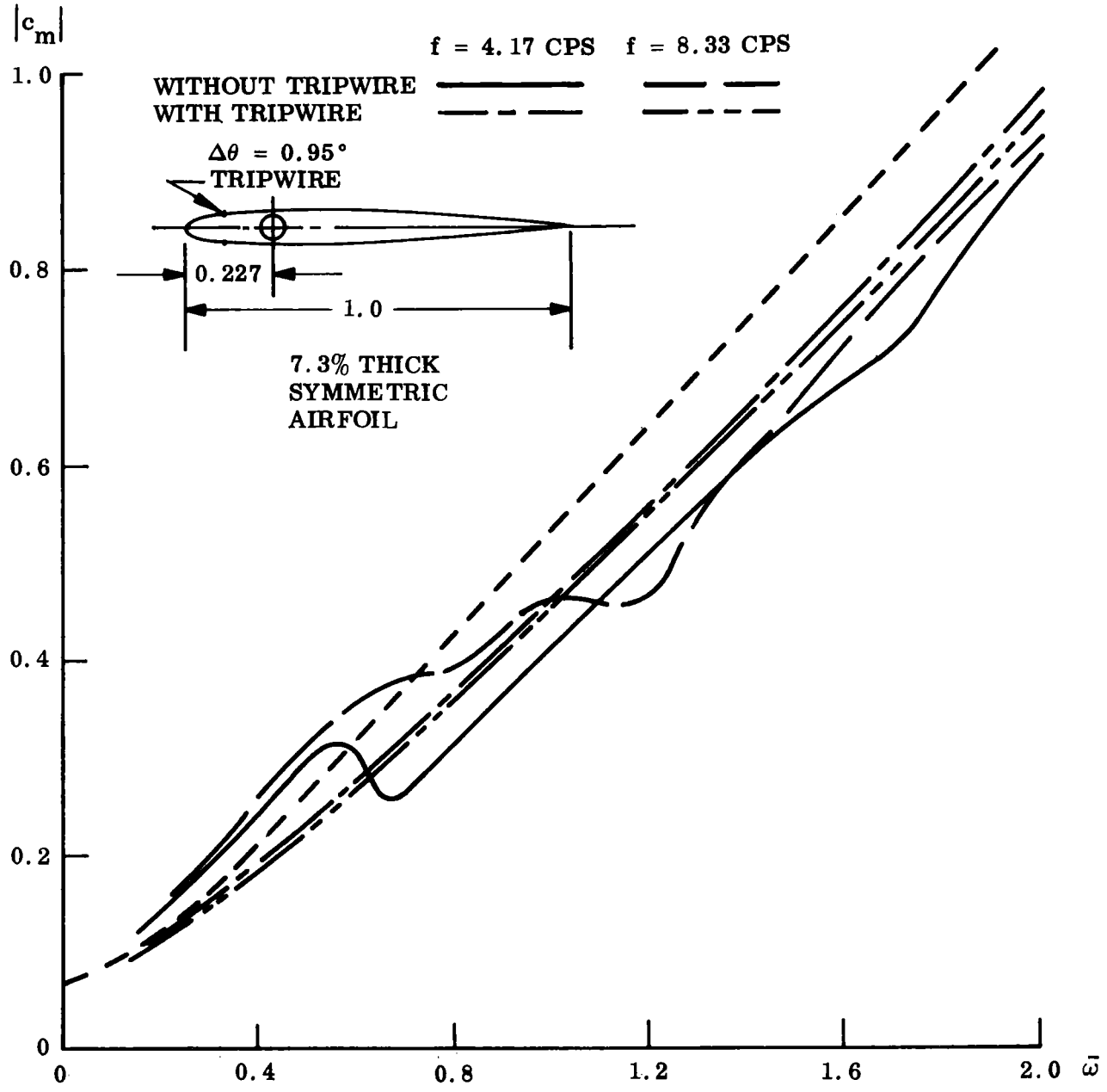

a. MOMENT AMPLITUDE VARIATION WITH FREQUENCY

Fig. 41a Effect of Trip Wire on the Dynamic Characteristics of a 7.3% Thick Symmetric Airfoil Oscillating in Pitch About the 22.7% Chord at $\alpha = 0$

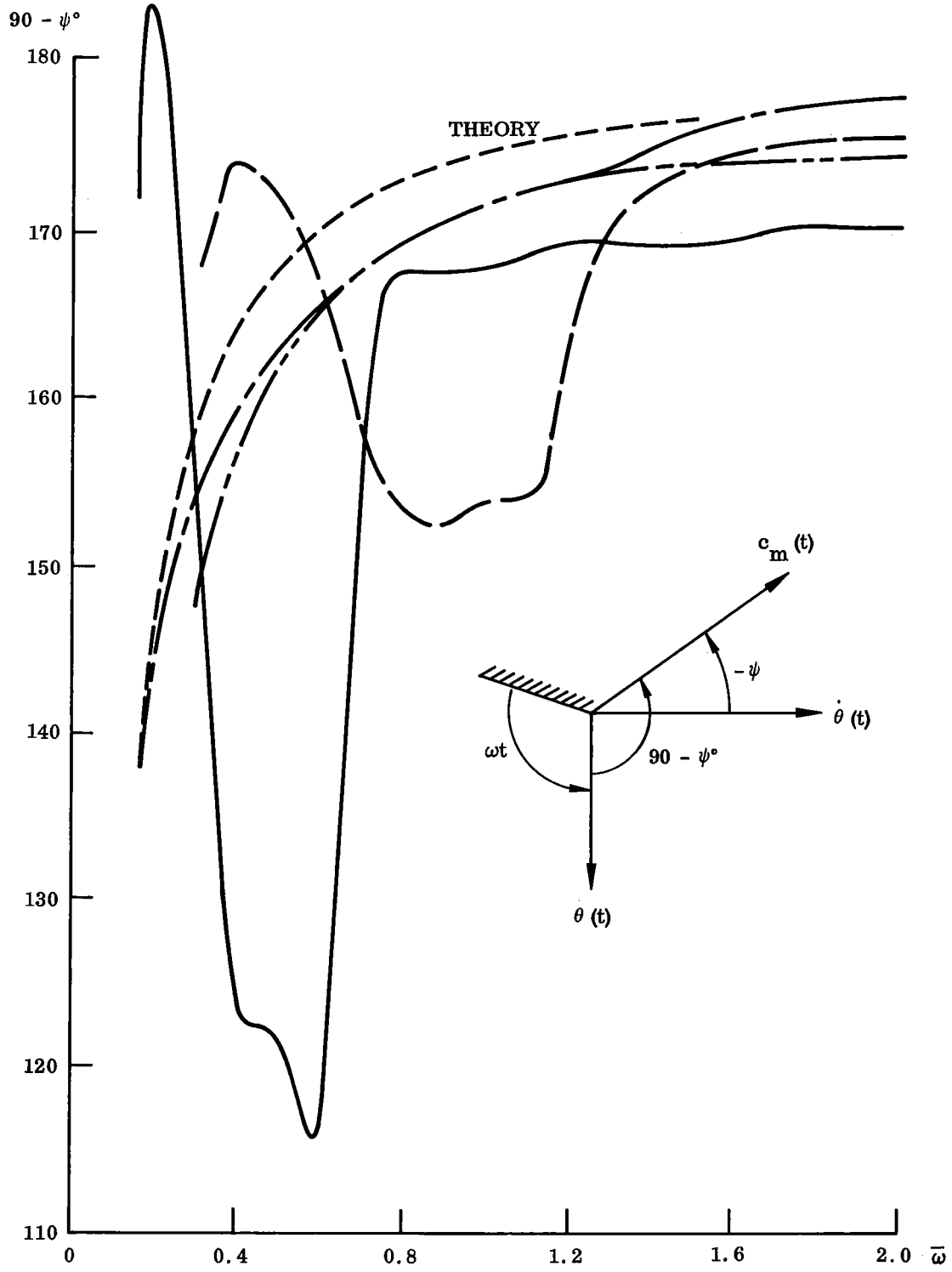

b. PHASE LEAD VARIATION WITH FREQUENCY

Fig. 41b Effect of Trip Wire on the Dynamic Characteristics of a 7.3% Thick Symmetric Airfoil Oscillating in Pitch About the 22.7% Chord at $\alpha = 0$

center $\xi_o = 0.227$ is close to the 25 percent chord where attached flow lift has no effect on the pitching moment. That is the reason for the large effects of "trailing-edge transition." For the same reason, trailing-edge separation will have large effects on pitch damping of airfoils with torsional oscillation axes near the 25 percent cord. Figure 42 explains what happens. The reduced frequency was changed by changing the (incompressible) velocity. Thus, the Reynolds number increases with decreasing reduced frequency, and, as a consequence, transition moves forward (over the airfoil) with decreasing $\bar{\omega}$.

At angle of attack the boundary-layer transition occurs more forward on the leeward side due to increased boundary layer edge velocity, and thereby increased local Reynolds number. The differential transition on top and bottom surfaces causes a force couple (Fig. 42 insets) similar to what is the result of leeward side trailing-edge separation (Fig. 1). When Reynolds number is increased (decreasing $\bar{\omega}$), the transition moves forward, and the forward force component becomes less and less effective, causing the overall static effect of boundary-layer transition to change from destabilizing to stabilizing. With this in mind, one can illustrate the effects using vector diagrams as shown in Fig. 42.

In the frequency range $0.8 < \bar{\omega} < 1.2$, the transition takes place near the trailing edge, causing a moment increment of magnitude $\Delta c_{m_{tr_1}}$. (Note that the stabilizing moment $-c_m$ is used in the vector diagram in sign agreement with the way the experimental results — Ref. 45 — were presented.) Without transition effects, the moment vector leads the velocity vector by $-\psi \approx 80°$ (due to the high apparent mass effects at these high reduced frequencies). Without any accelerated flow induced lag effects, the instantaneous transition induced moment would lead the angle of attack vector, $\theta(t)$, by 180°, as it is destabilizing. Using the effective time lags established earlier for boundary-layer separation (Fig. 17) indicates that $c_{m_{tr_1}}$ should lag its instantaneous position by more than 90° at $\bar{\omega} > 0.8$. Thus, the resultant vector will lag the attached flow vector by $\Delta\psi_1$ and will decrease the moment magnitude by, $\Delta \left| c_m \right|_{tr_1}$ in agreement with the observed test results.

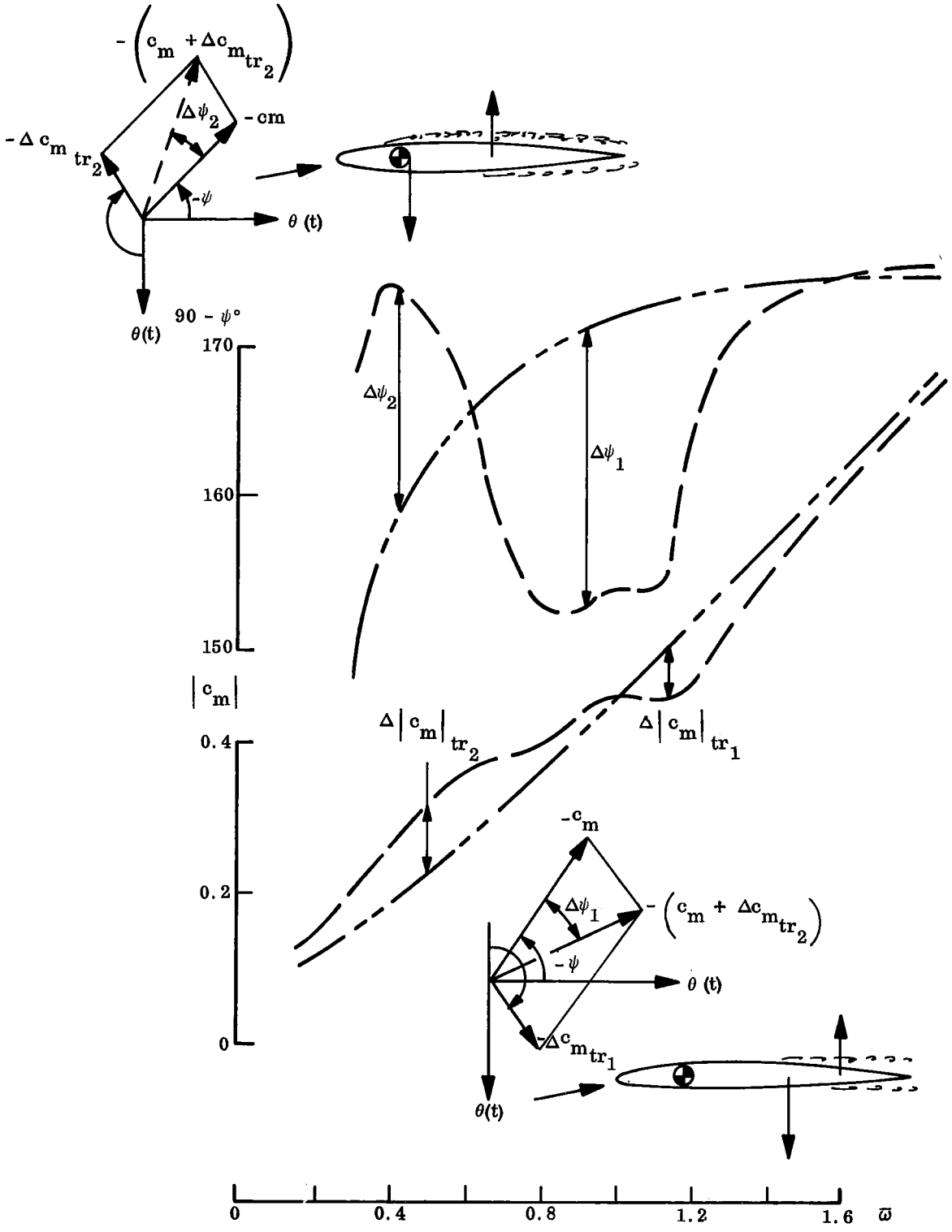

Fig. 42 Effect of Boundary-Layer Transition Induced Loads on Dynamic Characteristics

For $0.3 < \overline{\omega} < 0.6$, the phase lag of the transition induced moment is reduced to less than half the value it had in the previous vector diagram, while the attached flow vector lead has not changed much, $-\psi \approx 75°$. Thus, the situation depicted in the top vector diagram results. That is, the transition induced statically stabilizing moment causes the total vector to lead the attached flow vector by $\Delta\psi_2$ and increases the moment vector magnitude by $\Delta \left| c_m \right|_{t_{r_2}}$.

If one considers the other test run in Fig. 41 with the lower frequency, f = 4.17 cps, the whole interaction region is moved down to lower $\overline{\omega}$ - values. The top vector diagram in Fig. 42 illustrates directly that an increase of the lead $\Delta\psi_2$ is to be expected, and the bottom vector diagram shows that the lag will increase also. The large accelerated flow effect is in agreement with observed effects of boundary-layer transition on the vehicle dynamics of slender bodies of revolution (Ref. 46). The results shown in Figs. 41 and 42 vividly demonstrate the powerful effects that trailing-edge separation will have on unsteady airfoil aerodynamics.

In order to predict unsteady airfoil characteristics versus instantaneous angle of attack, the loops presented by Carta, Liiva, Halfman, Ham, and others (Refs. 1, 2, 3, 32, 35, and 36), the graphical construction from static characteristics described in Ref. 27 is used. Figures 43 and 44 show in detail how the construction is done. First, the instantaneous loop is constructed. This is a composite of effects which include lift overshoot and undershoot, attached and separated flow camber effects. Attached flow phase lag (lumped von Karman-Sears lag) is used below stall, where attached flow is anticipated, and the additional accelerated flow phase lag is added after static stall, i.e., for $\alpha(t) > \alpha_s$. The discontinuous change in phase lag at α_{stall} is faired out manually over $\Delta\alpha = 2°$.

For turbulent trailing edge stall, there are no difficulties in constructing the overshoot and undershoot characteristics (Fig. 43). Based upon Kline's findings (Ref. 20), complete (anti)symmetry is assumed for the delay of separation and reattachment caused by the accelerated flow effect on the adversity of the pressure gradient. The composite

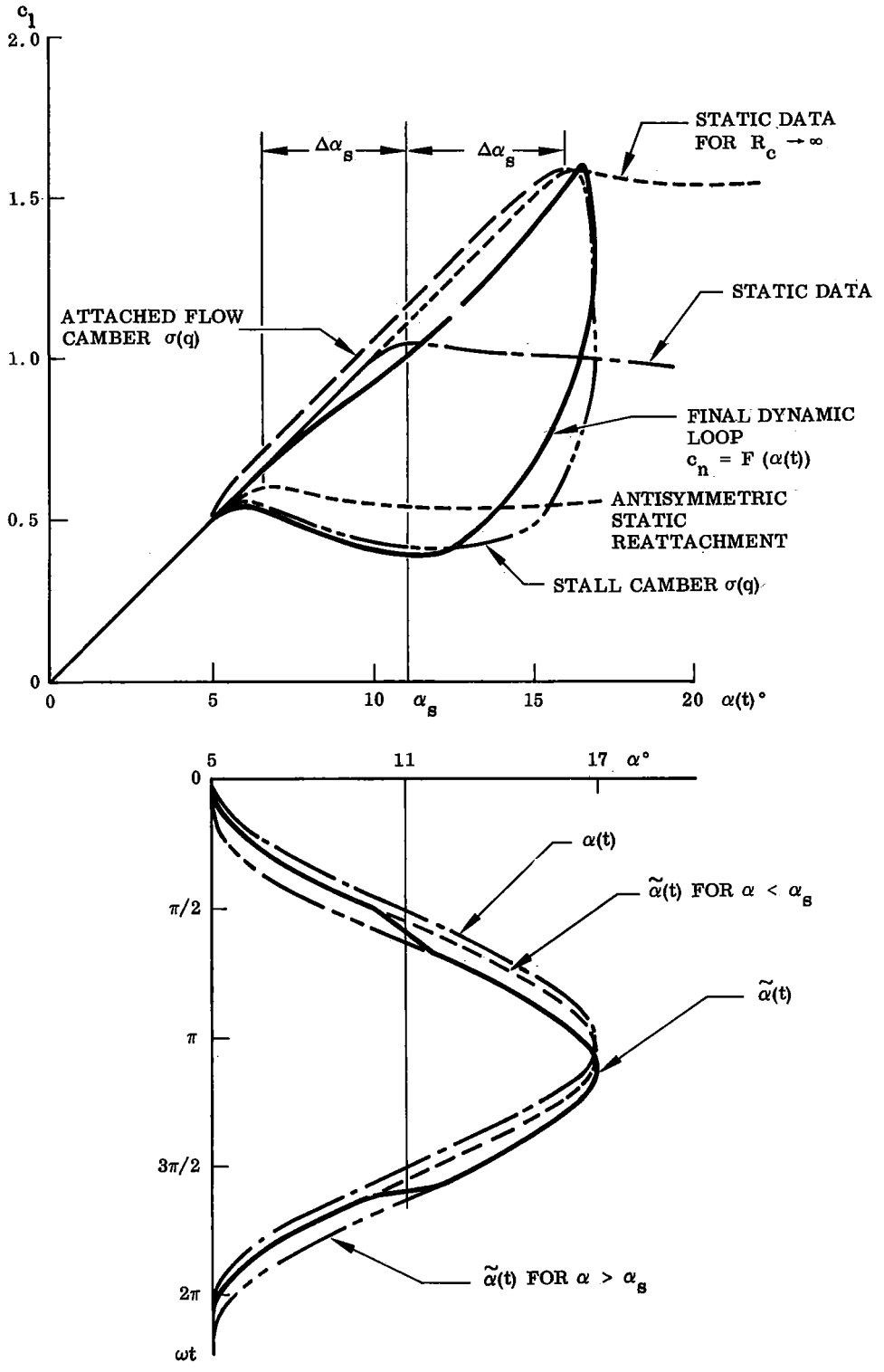

Fig. 43 Quasi-Steady Construction of Dynamic Normal Force Characteristics Including Time Lag Effects Due to Vortex Wake and Accelerated Flow for Turbulent Trailing Edge Stall

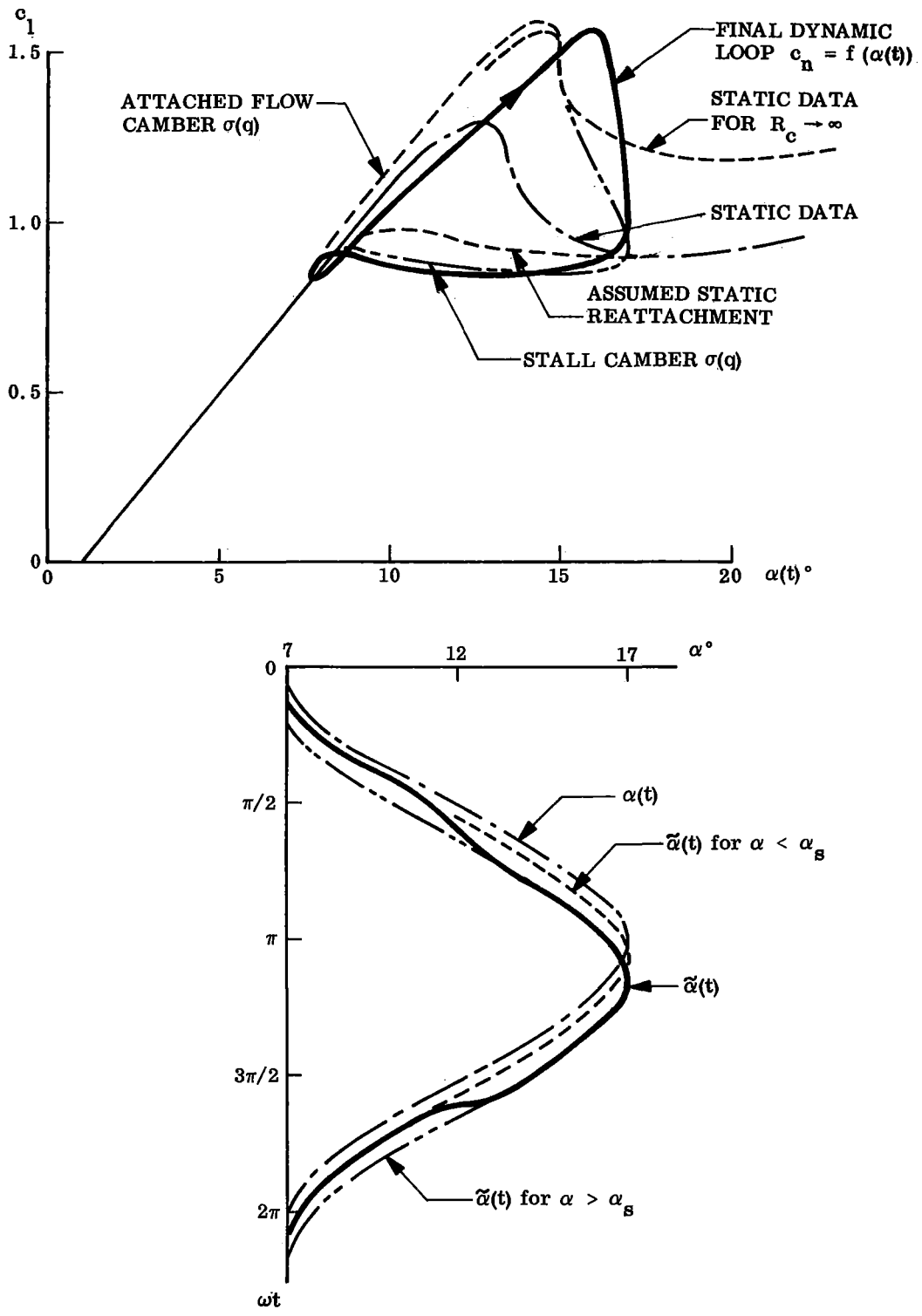

Fig. 44 Quasi-Steady Construction of Dynamic Normal Force Characteristics Including Time Lag Effects Due to Vortex Wake and Accelerated Flow for Leading Edge Stall

instantaneous loop is constructed using $c_{l_{max}}$ for infinite Reynolds number and assuming $\Delta\alpha_{stall}$ is the same for the "downstroke" as for the "upstroke." Thin airfoil theory gives the attached flow pitch rate induced camber effect, while static experimental data are used to obtain the effect of camber after separation. Separated flow camber effects are used down to the stall point $\alpha = \alpha_s - \Delta\alpha_s$, of the assumed static reattachment curve. At the limits of the cycle when $\dot{\alpha} = q = 0$, steady lift values are used at α_{max}. The appropriate attached flow and separated flow time lags described previously are then applied to these instantaneous characteristics to obtain the final dynamic loop. Throughout the loop constructions presented here, an effective equivalent time lag of $\Delta\xi_a = 2$ was used for the accelerated flow effect, as it seemed to be a representative value for trailing-edge stall (Fig. 17) as well as for oscillatory leading-edge stall (Fig. 20).

For leading-edge separation, the limiting static characteristics in regard to overshoot and undershoot are, in general, those sketched in Fig. 44; that is, a large infinite Reynolds number overshoot of $c_{l_{max}}$ on the "upstroke," whereas the "backstroke" characteristics are those for thin airfoil stall. This should be a fairly good assumption, especially in view of the negative camber existing on the "backstroke" (Ref. 47 and Fig. 45). There are, of course, possibilities of changes in stall pattern at critical Reynolds numbers as was discussed before. The effects of time lag and camber are handled as described earlier.

For thin airfoil stall, there are no accelerated flow effects to be concerned about, and it appears that it should be possible to predict the unsteady characteristics by the methods proposed by Sarpakaya and Ham (Refs. 41 and 43). No specific examples of unsteady thin airfoil stall are discussed in the present report.

Figure 46 shows how well the quasi-steady time-lagged predictions agree with Carta's data for trailing edge type stall (Ref. 1). It should be noted that it is the agreement of the net area enclosed by the dynamic loop that determines how well the damping characteristics agree.

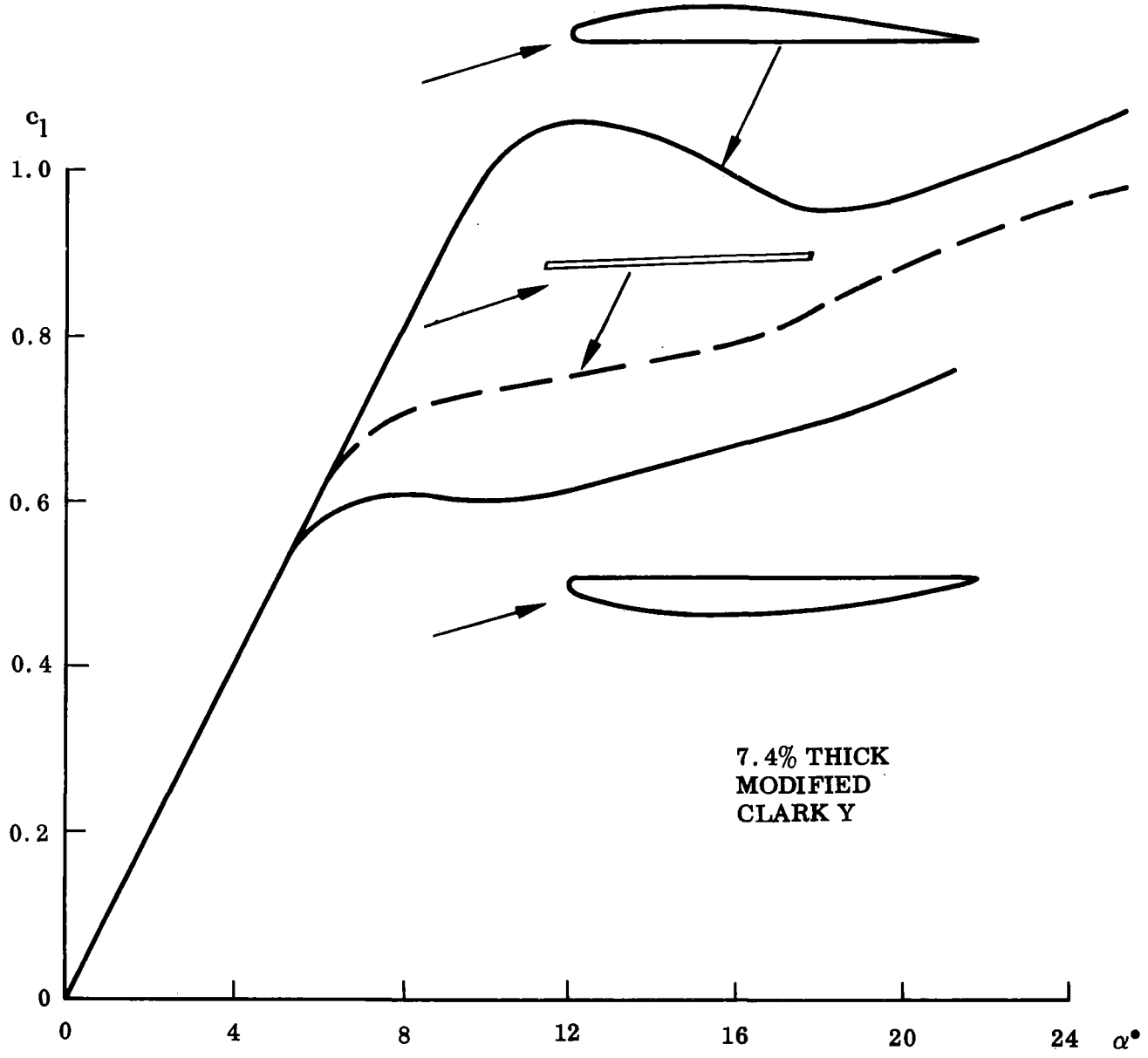

Fig. 45 Effect of Negative Camber on Static Stall Pattern

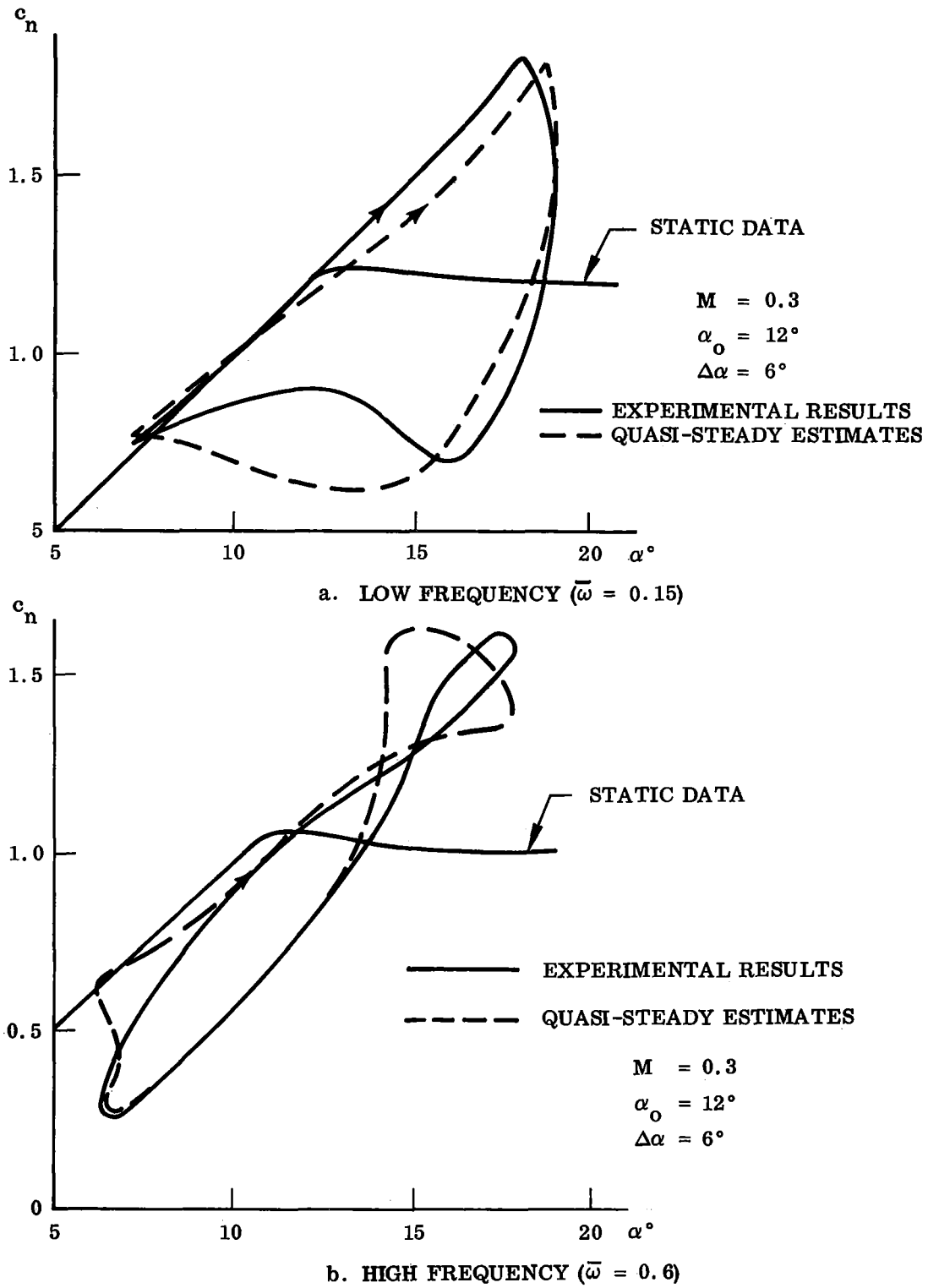

Fig. 46 Effect of Frequency on Normal Force Estimates for Dynamic Trailing Edge Stall (NACA 0012 Airfoil Section, Ref. 1)

Figures 47 – 50 show how Liiva's extensive data (Ref. 2) can be predicted with a fair amount of success, especially in regard to enclosed net area by the loops. It should be noted that no accelerated flow time lag was used in reproducing the deep stall loops (α_o = 24.57° in Figs. 47 and 48). Once the separation is established, the only lag acting is that induced by the shed vorticity into the wake. Thus, these loops are constructed using only the separated flow σ (q)-camber and the lumped von Karman-Sears time lag.

The effect of frequency for Liiva's data is much the same as it was for Carta's. That is, at high reduced frequencies the agreement between quasi-steady prediction and experimental data deteriorates (compare Fig. 46 with Figs. 49 and 50).

In Ref. 36, Jaan Liiva shows the big differences observed in the shape of successive moment loops (Fig. 51). He uses an average of several loops to determine the loops used in his various publications. Liiva ascribes these variations to large-scale turbulent eddies and expects a random load variation. However, the loops look more like they were the result of a slightly off resonance interaction with the alternate vortex shedding discussed earlier. Some of the "c_m-blips" shown at the end of the "backstroke" could possibly be caused by such interference, the delayed results of the trailing edge "fish tailing" being a suspect cause. Acoustic wall interference effects are always of concern but do not seem to be a likely culprit at the $\overline{\omega}$ - M range tested (Ref. 48 and Fig. 52). It is only in the stall penetration case that characteristics become peculiar, and adverse dynamic effects result from the "on-off stall."

Perhaps this near-resonance phenomenon is responsible for the poor prediction of Liiva's unusual c_n-Loop (Fig. 53 and Ref. 49). However, it is quite often difficult to get good correlation when stall occurs at the end of the upstroke. In viewing Kline's argument (Ref. 20), it could be that the assumption of returning to the steady characteristic at the end of the cycle is sometimes invalid. If the separation pockets do not completely coalesce, it seems reasonable to assume that the appropriate return cycle should be along some intermediate curve. This holds only for the turbulent

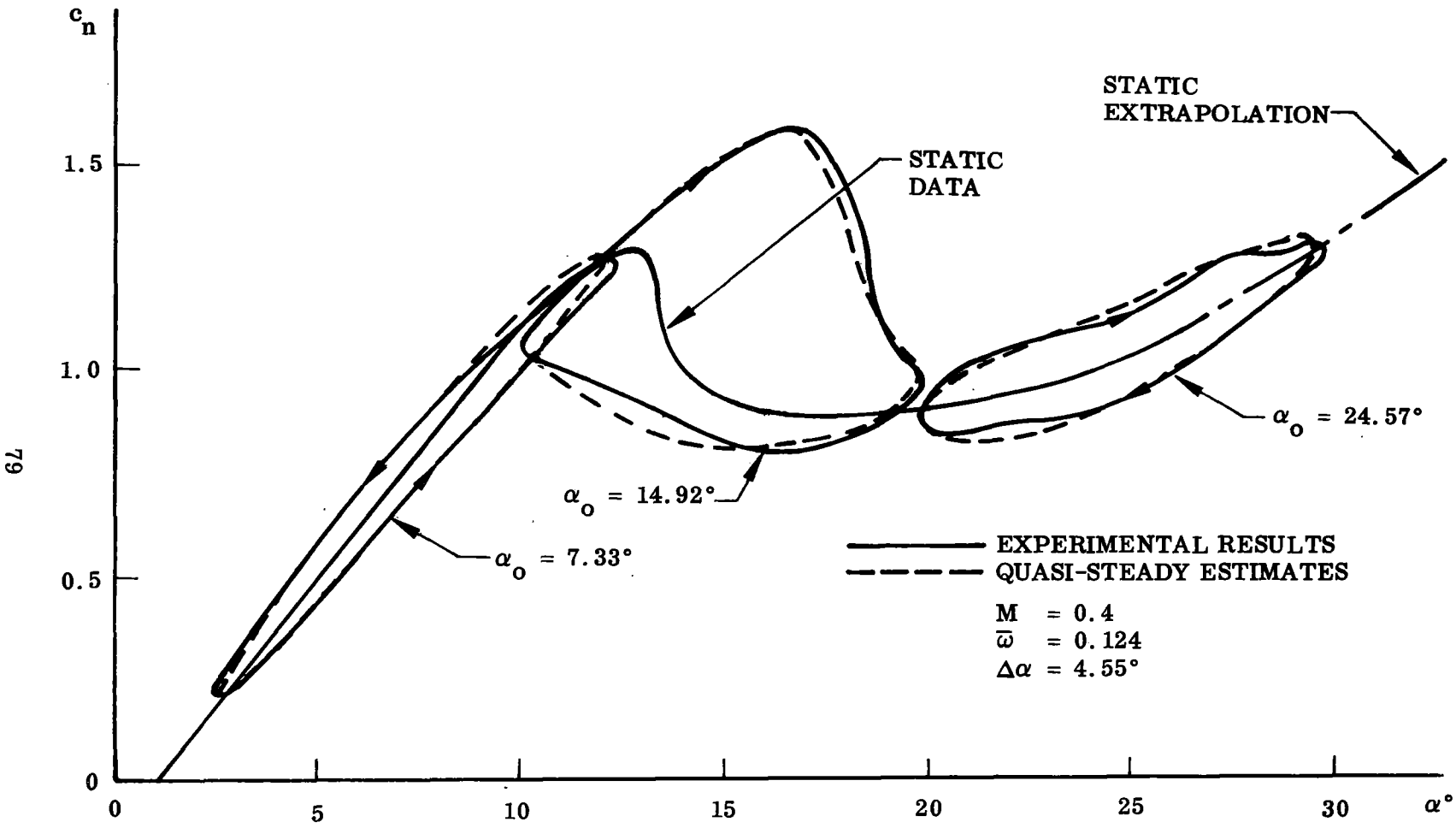

Fig. 47 Effect of Angle-of-Attack on Normal Force Dynamic Characteristics (Vertol 23010-1.58 Airfoil Section, Ref. 2)

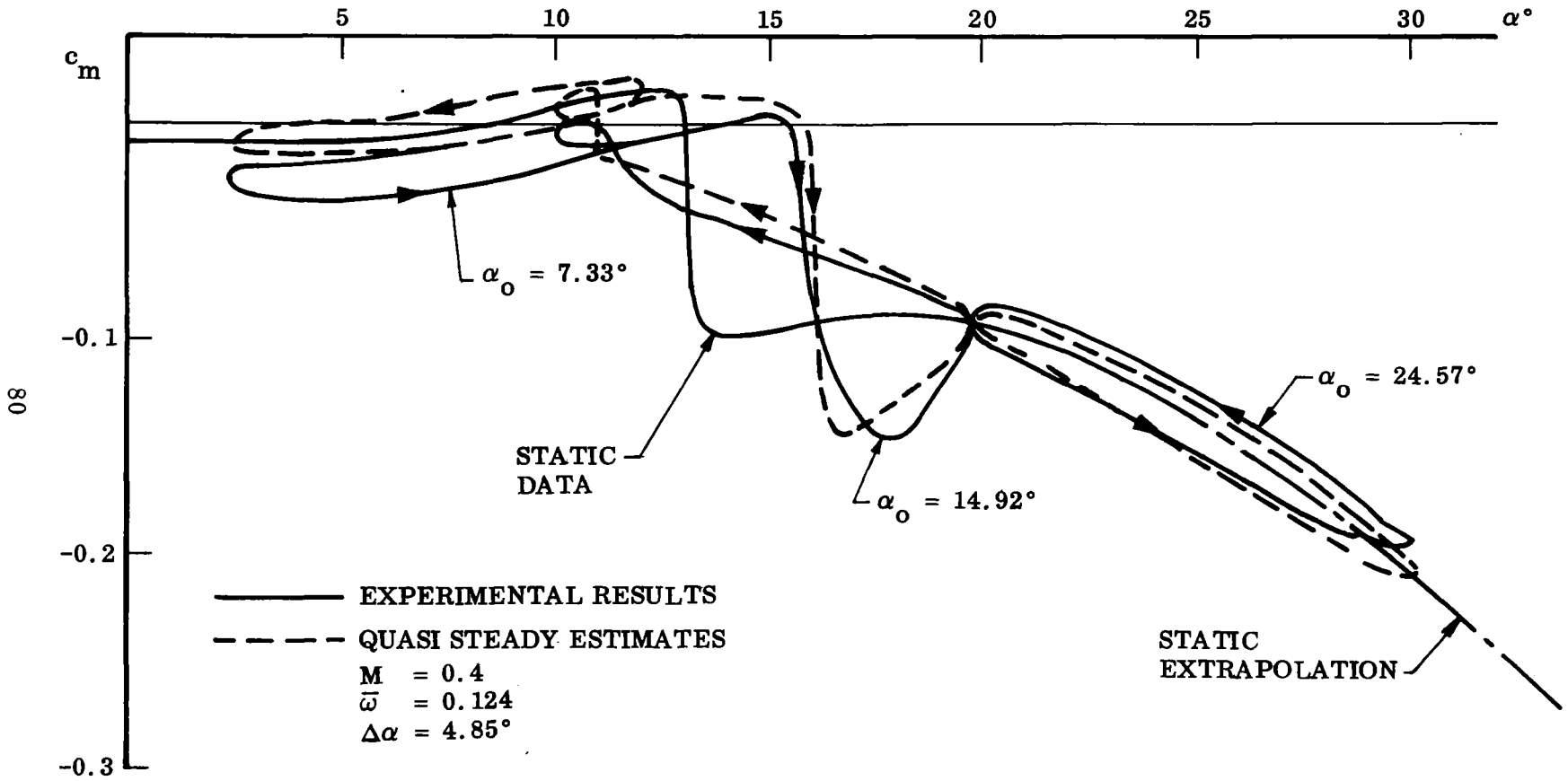

Fig. 48 Effect of Angle-of-Attack on Pitching Moment Dynamic Characteristics (Vertol 23010-1.58 Airfoil Section, Ref. 2)

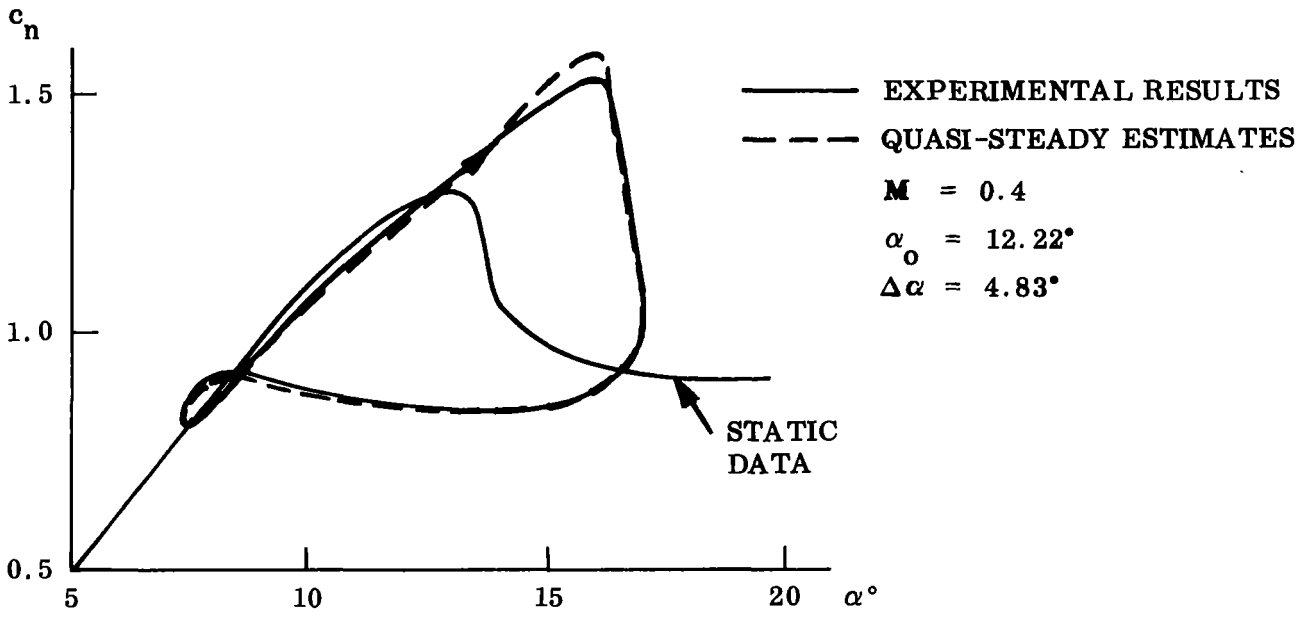

a. LOW FREQUENCY ($\bar{\omega}$ = 0.124)

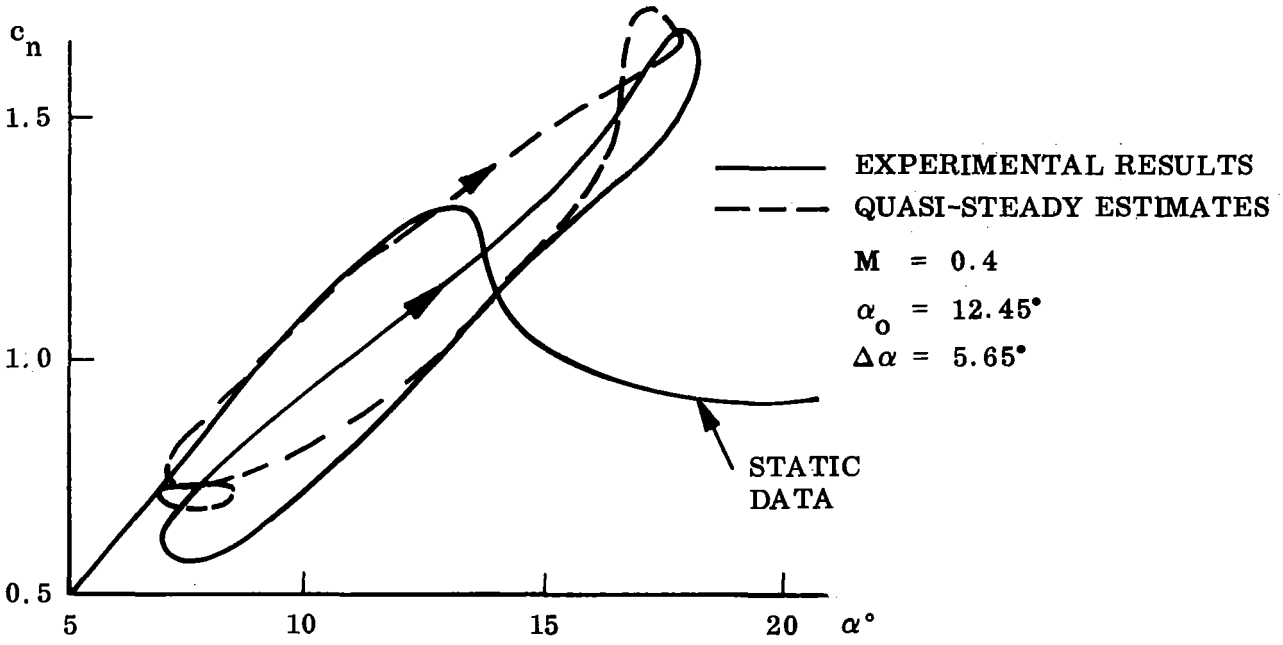

b. HIGH FREQUENCY ($\bar{\omega}$ = 0.71)

Fig. 49 Effect of Frequency on Normal Force Dynamic Characteristics (Vertol 23010-1.58 Airfoil Section, Ref. 2)

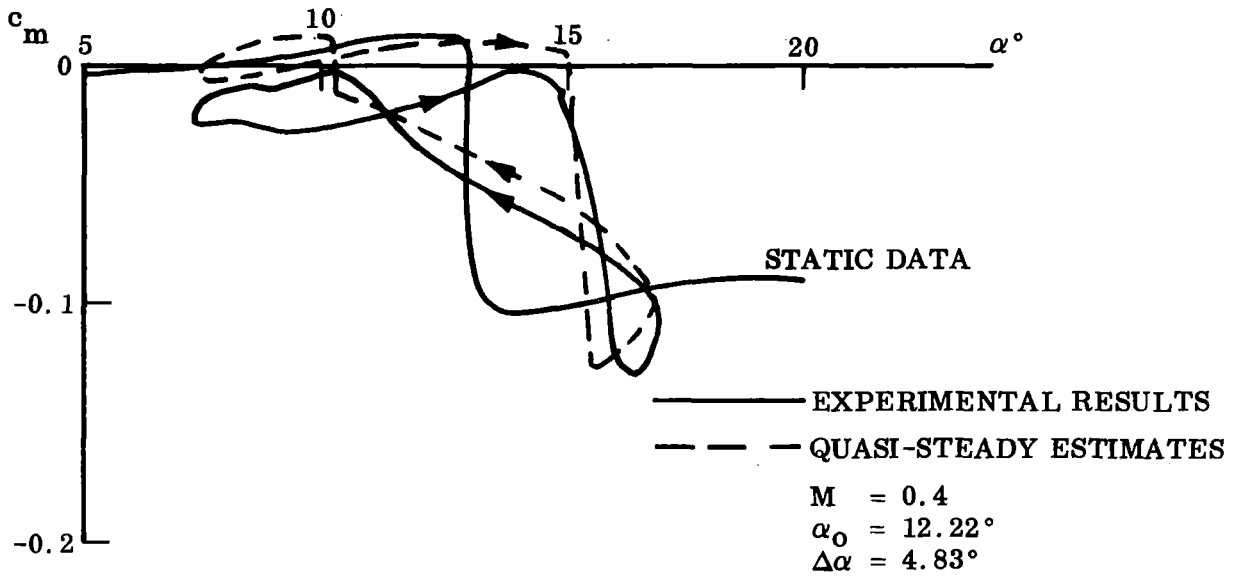

a. LOW FREQUENCY ($\bar{\omega}$ = 0.124)

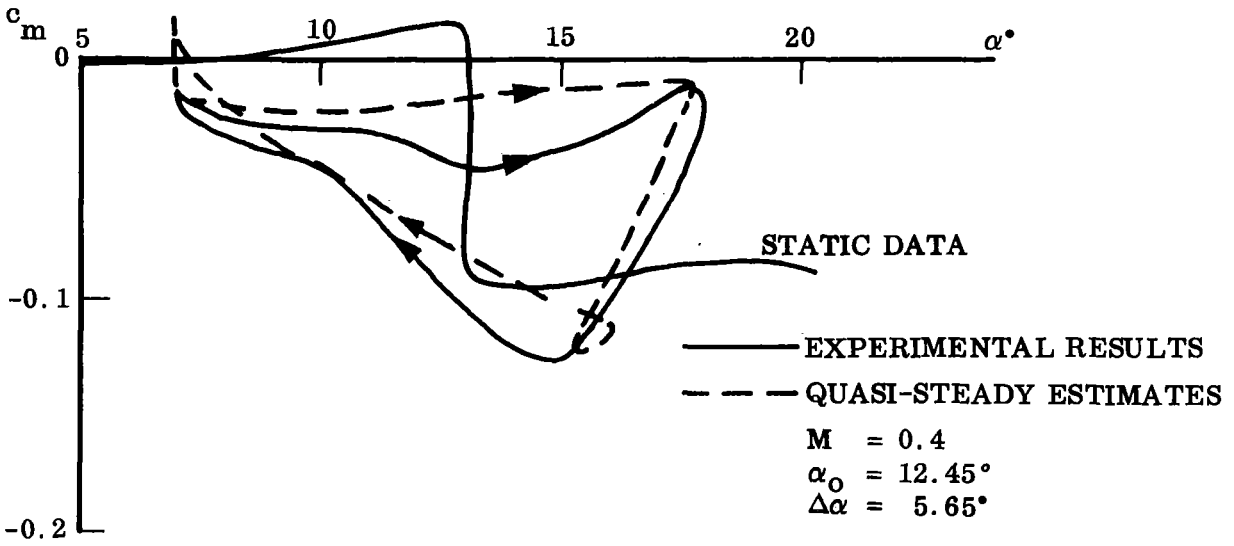

b. HIGH FREQUENCY ($\bar{\omega}$ = 0.71)

Fig. 50 Effect of Frequency on Pitching Moment Dynamic Characteristics (Vertol 23010-1.58 Airfoil Section, Ref. 2)

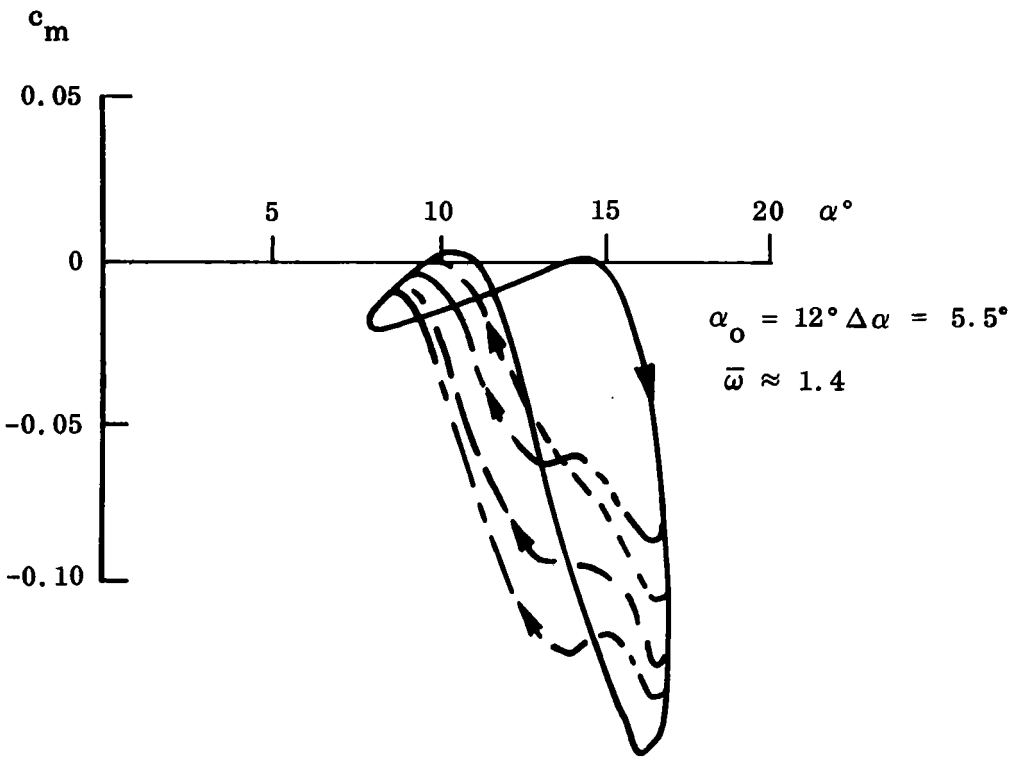

Fig. 51 Nonrepeating Consecutive Dynamic Moment Loops

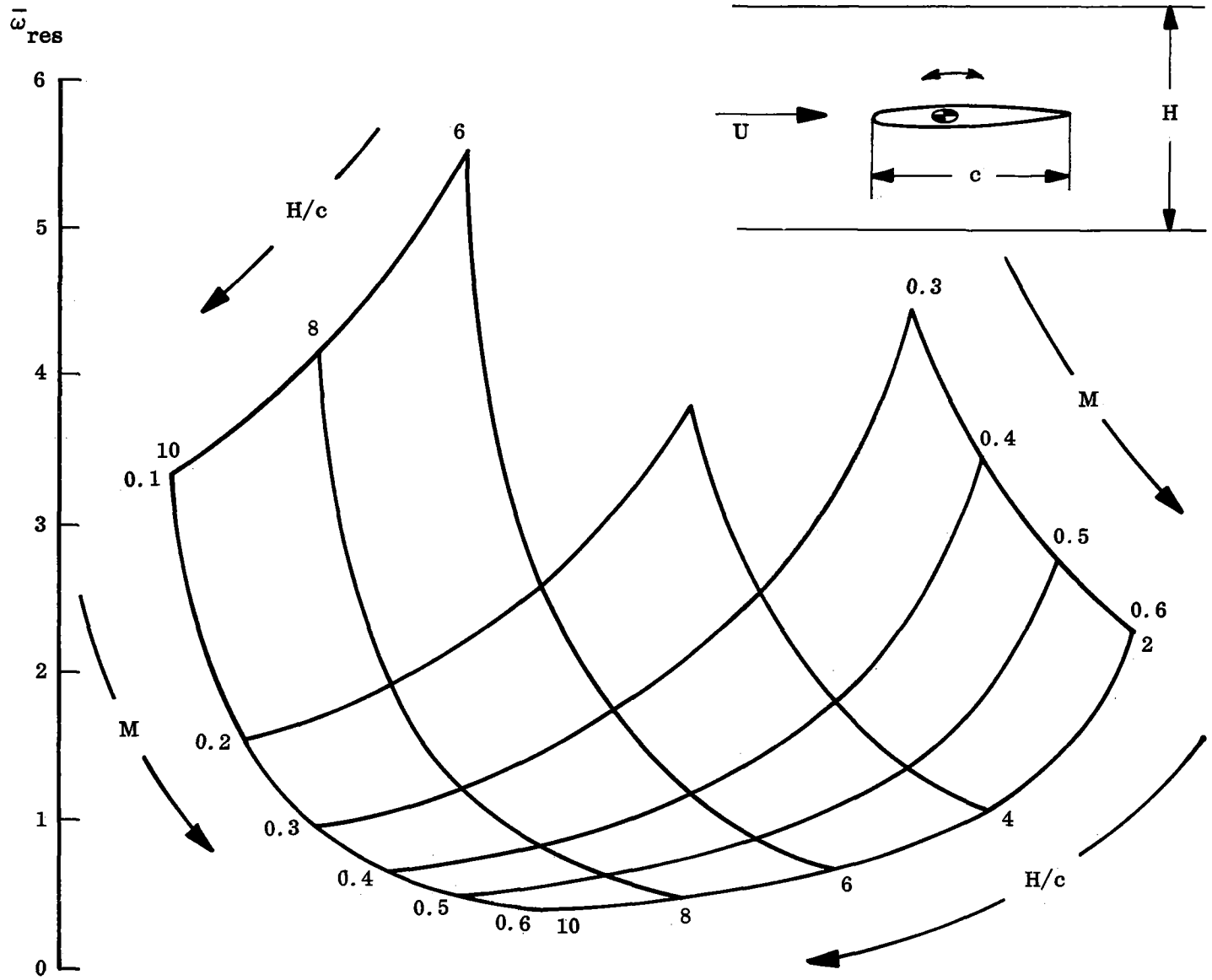

Fig. 52 Critical Parameters for Acoustic Wind-Tunnel Wall Intereference

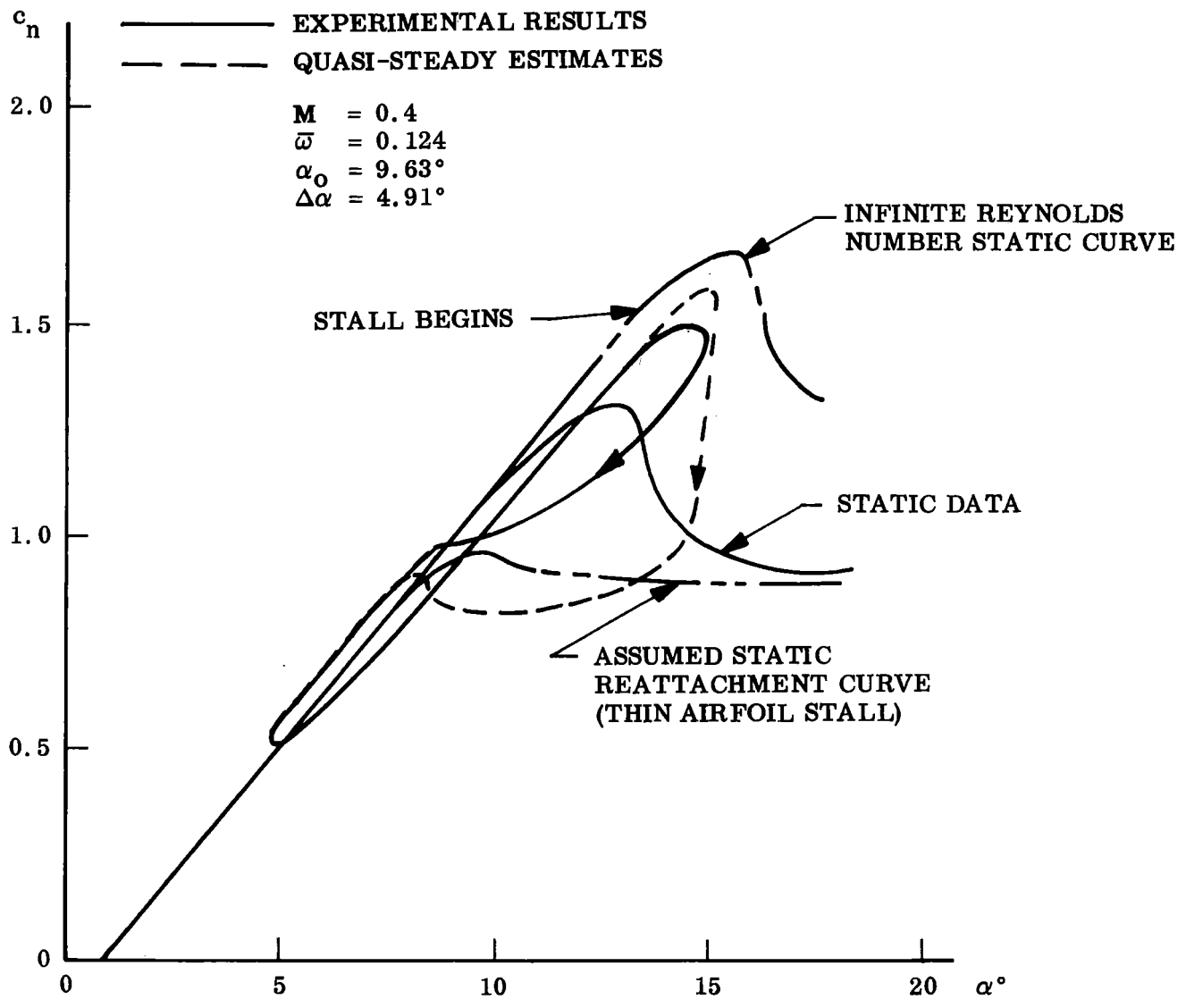

Fig. 53 Comparison Between Predicted and Experimental Dynamic Normal Force Loops for Slight Stall Penetration (Vertol 23010-1.58 Airfoil Section, Ref. 49)

trailing-edge separation. However, as was discussed earlier, the dynamic stall behavior may be of the turbulent type even if the static stall is of leading-edge type.

Data by Carta for supposedly turbulent separation show similar effects (Fig. 54a and Ref. 32). The predictions obtained with the regular usage of the static stall characteristics (described in Fig. 43) do not agree at all with the experimentally observed dynamic stall loops (α_o = 12° and 24° in Fig. 54a). However, by assuming certain shifted static reattachment characteristics (both in α and c_m) the loops can be better reproduced (Fig. 54b). This method of "fudging" in order to reproduce the measured results is rather unscientific, but it does illustrate the sensitivity of the dynamic results to details of the reattachment phenomenon. Carta's data are highly irregular in that trailing-edge stall occurs at Raynolds numbers where one would expect leading-edge stall for the NACA 0012 airfoil (Fig. 3a). This leads one to suspect wall interference or instrumentation irregularities, thus questioning the applicability of the data to full scale flight conditions. It is possible that both types of stall co-exist along the end-plated "two-dimensional" wing, and that a flip from this mixed stall to leading edge stall occurs on the "backstroke." Such a switch from trailing edge to leading-edge stall could also occur for a truly two-dimensional airfoil on the "backstroke." It is not impossible that the predicted results in Fig. 54a could be more indicative of full-scale performance than the dynamic experimental results.

In view of all the various flow mechanisms involved, the success of the simple analytical predictions from static data to match the experimental dynamic characteristics is very encouraging. It is undoubtedly true that better descriptions of the moment loops are needed, which at lower reduced frequencies would depend mainly on a more detailed knowledge of the static characteristics, in particular the transition from stall to reattachment. At high reduced frequencies, interaction with the "spilled" vortex and with motion-independent vortex shedding, as well as circulation or downwash effects from previous "stroke," have to be included. However, it appears that it will be possible to describe the unsteady stall characteristics analytically with the detail needed for inclusion in unsteady analyses of turbomachinery and helicopter rotors including coupling between various degrees of freedom.

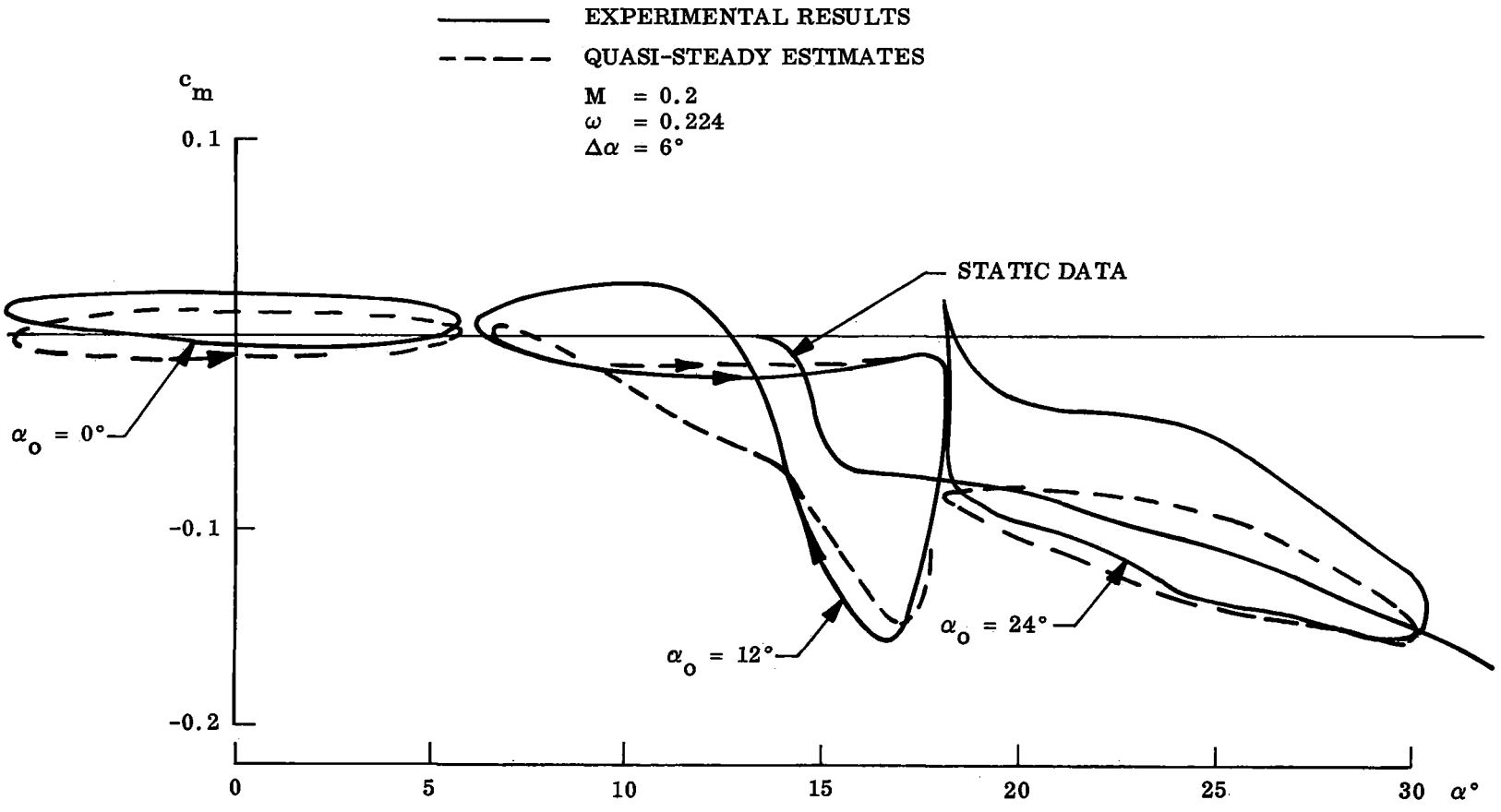

a. REGULAR PROCEDURE (SHOWN IN FIG. 43)

Fig. 54a Sensitivity of Dynamic Moment Characteristics to Static Characteristics (NACA 0012 Airfoil Section, Ref. 32)

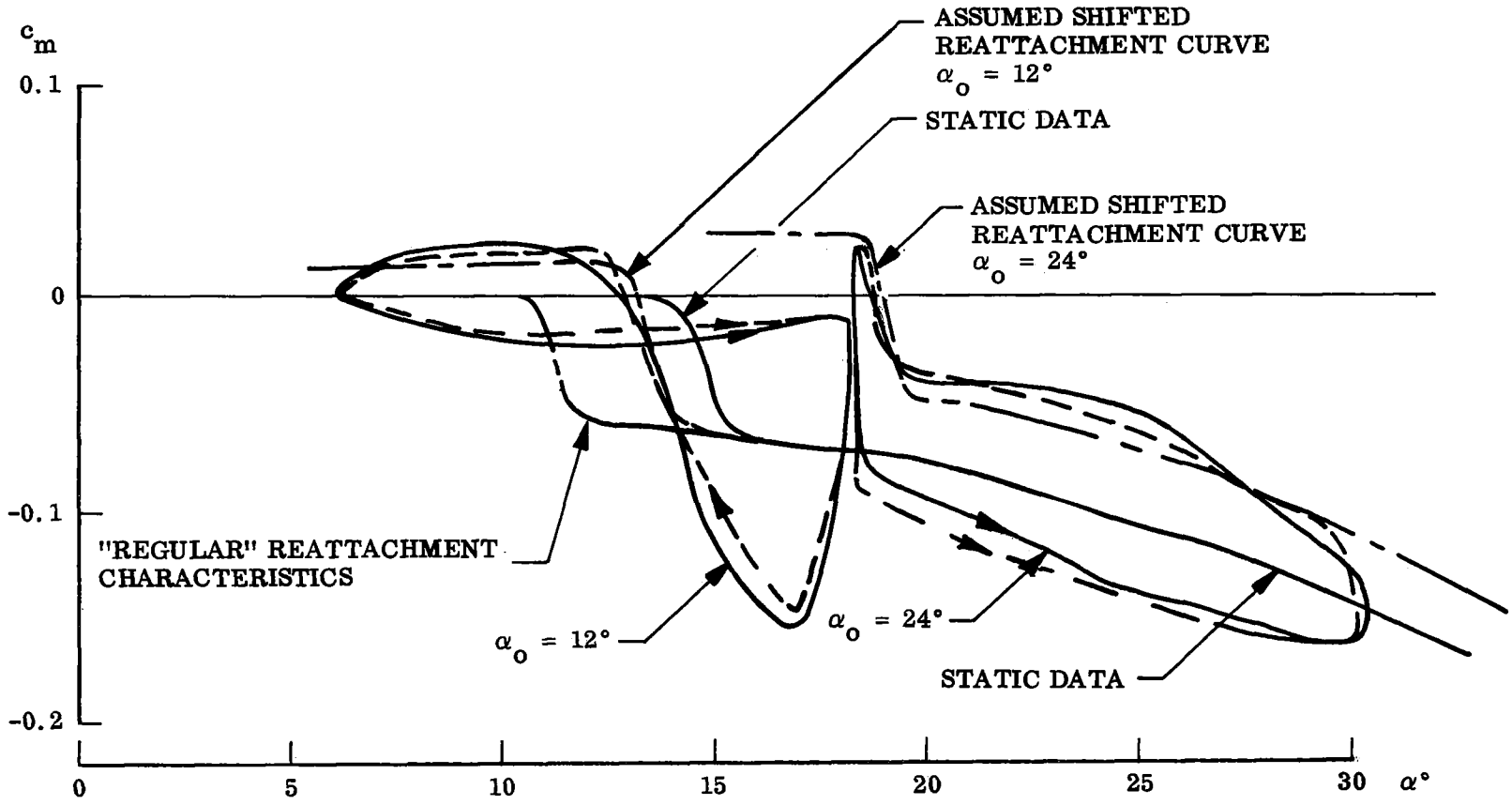

b. ADJUSTED REATTACHMENT CHARACTERISTICS

Fig. 54b Sensitivity of Dynamic Moment Characteristics to Static Characteristics (NACA 0012 Airfoil Section, Ref. 32)

Section 5
CONCLUSIONS

The study of unsteady airfoil stall has revealed that most of the apparently anomalous characteristics can be explained by simple antlytic concepts and can, to a large extent, be predicted from static (experimental) characteristics. The prominent and outstanding problem analytically is the large dynamic overshoot of static stall and undershoot of static reattachment.

For turbulent trailing edge stall, both the overshoot and undershoot are caused by the effects of pitch-induced flow acceleration on the adversity of the leeward side pressure gradient. Both the overshoot and undershoot are to a first approximation proportional to $c\dot{\alpha}/U_\infty$, the dimensionless frequency induced plunging.

For thin airfoil stall the overshoot and undershoot are caused by the finite time involved in the growth of leading edge and trailing edge vortices. An alternating vortex shedding phenomenon is complicating an otherwise well-defined unsteady flow picture.

Leading-edge stall contains a little of both the above flow characteristics with some nontrivial additional problems. The leading-edge stall is delayed initially by the accelerated flow effect. Once the separation has occurred, the dynamic stall characteristics become very similar to those of the thin airfoil stall. However, the sudden "spillage" of a strong leading edge vortex, rather than a gradual buildup of it, changes the leading edge-trailing edge vortex interference pattern.

The above general characteristics are often upset by change in stall type. Thus, a static leading edge stall may convert into a dynamic trailing edge stall. This can happen through pitch rate induced accelerated flow effects on the pressure gradient, but the most dramatic switch seems to happen because the pitch rate induced

energizing of the leading edge boundary layer results in an apparent increase of the "effective Reynolds number."

The most important conclusion to be drawn from the present study is that the situation existing in a dynamic wind tunnel test may not at all simulate full-scale conditions in regard to stall behavior. Unsteady airfoil stall appears, therefore, to be a problem that will need considerable attention before predictions of compressor or helicopter dynamic blade stall can be made with confidence. The results obtained in the present exploratory study indicate that it should be possible to use simple analytic techniques to build up the needed prediction methods.

Section 6
RECOMMENDATIONS FOR FUTURE STUDY

The performed exploratory study vividly demonstrates the need for continued study of the unsteady airfoil stall problem. The results obtained indicate that the prospects are good that a complete analytic theory can be developed that satisfactorily will predict full-scale unsteady airfoil stall using static experimental data as an input. Further research is needed to develop the quasi-steady time-lagged theory from the presented graphical-semi-empirical status. It would also be desirable to extend the research to include effects of shock induced boundary-layer separation, as higher subsonic Mach numbers are of current practical interest for aircraft industry as a whole, including compressor and helicopter applications. The aircraft buffet problem is intimately connected with this shock-boundary layer interaction phenomenon.

The developed analytic theory should be checked by specially designed dynamic tests. It is very probable that the unsteady airfoil characteristics through stall can be described analytically with sufficient detail to permit direct usage in analysis of actual compressors or helicopters. The three-dimensional effects of centrifugal spanwise flow and highly nonuniform blade loadings have to be added. The spanwise venting of the blade wake may radically limit the applicability of dynamic test data, if the effect cannot be accounted for analytically.

Section 7
REFERENCES

1. F. O. Carta, "Unsteady Normal Force on an Airfoil in a Periodically Stalled Inlet Flow," J. Aircraft, Vol. 4, No. 5, Sep–Oct 1967, pp. 416–421 (presented as Paper 67-18 at the 5th AIAA Aerospace Sciences Meeting, New York, N.Y., Jan 23–26, 1967)

2. J. Liiva, "Unsteady Aerodynamic and Stall Effects on Helicopter Rotor Blade Airfoil Sections," Paper 68-58, AIAA 6th Aerospace Sciences Meeting, New York, N.Y., Jan 22–24, 1968

3. R. L. Halfman, H. C. Johnson, and S. M. Haley, Evaluation of High-Angle-of-Attack Aerodynamic-Derivative Data and Stall-Flutter Prediction Techniques, NACA TN 2533 (1951)

4. A. G. Rainey, Measurement of Aerodynamic Forces for Various Mean Angles of Attack of an Airfoil Oscillating in Pitch and on Two Finite-Span Wings Oscillating in Bending with Emphasis on Damping in the Stall, NACA TN 3643 (1965)

5. F. D. Harris and R. P. Pruyn, "Blade Stall – Half Fact, Half Fiction," American Helicopter Society Journal, Vol. 13, No. 4, Apr 1968, pp. 27–48

6. L. E. Ericsson and J. P. Reding, "Analysis of Flow Separation Effects on the Dynamics of a Large Space Booster," J. Spacecraft and Rockets, Vol. 2, No. 4, July–Aug 1965, pp. 481–490

7. -----, "Dynamic Stability Problems Associated with Flare Stabilizers and Flap Controls," Paper 69-182, AIAA 7th Aerospace Sciences Meeting, New York, N.Y., Jan 20–22, 1969

8. G. B. McCullough and D. E. Gault, Examples of Three Representative Types of Airfoil-Section Stall at Low Speed, NACA TN 2502, 1951

9. D. D. Carrow, A Note on the Boundary Layer and Stalling Characteristics of Airfoils, Great Britain ARC CP No. 174, 1950

10. L. K. Loftin and W. J. Bursnall, The Effects of Variations in Reynolds Number Between 3.0×10^6 and 25.0×10^6 Upon Aerodynamic Characteristics of a Number of NACA 6 – Series Airfoil Sections, NACA TN 1773 (1948)

11. G. B. McCullough and D. E. Gault, Boundary Layer and Stalling Characteristics of the NACA 64A006 Airfoil Section, NACA TN 1923 (1949)

12. E. N. Jacobs and A. Sherman, Airfoil Section Characteristics as Affected by Variations in the Reynolds Number, NACA Tech. Report 586 (1937)

13. R. M. Pinkerton, The Variation with Reynolds Number of Pressure Distribution Over an Airfoil Section, NACA Tech. Report 613 (1938)

14. J. H. Preston, Visualization of Boundary Layer Flow, Great Britain ARC R&M 2267 (1946)

15. P. Poisson-Quinton et A. deSievers, Etude Aerodynamique d'un Element de Pale d'Helicoptère,

16. J. A. Kelly, Effect of Modifications to the Leading-Edge Region on the Stalling Characteristics of the NACA 63, -012 Airfoil Section, NACA TN 2228 (1950)

17. D. E. Gault, A Correlation of Low-Speed, Airfoil-Section Stalling Characteristics with Reynolds Number and Airfoil Geometry, NACA TN 3963 (1957)

18. "Influence des Decallements au Bord d'Attaque sur les Characteristiques Aerodynamiques des Voilures," par l'Ingenieur Principal de L'AIRVILLE

19. C. C. Critzos, H. H. Heyson, and R. W. Boswinkle, Jr., Aerodynamic Characteristics of NACA-0012 Airfoil Section at Angles of Attack from 0° to 180°, NACA TN 3361 (1955)

20. E. N. Jacobs, K. E. Ward, and R. M. Pinkerton, The Characteristics of 78 Related Airfoil Sections from Tests in the Variable-Density Wind Tunnel, NACA Tech. Report 460 (1935)

21. S. J. Kline, "Some New Concepts of the Mechanics of Stall in Turbulent Boundary Layers," J. Aero. Sci., Vol. 24, No. 6, June 1957, pp. 470–471

22. F. Conner, C. Willey, and W. Twomey, A Flight and Wind Tunnel Investigation of the Effect of Angle-of-Attack Rate on Maximum Lift Coefficient, NACA CR-321 (1965)

23. P. W. Harper and R. E. Flanigan, The Effect of Rate of Change of Angle of Attack on the Maximum Lift of a Small Model, NACA TN 2061 (1949)

24. B. L. Gadeberg, The Effect of Rate of Change of Angle of Attack on the Maximum Lift Coefficient of a Pursuit Airplane, NACA TN 2525 (1951)

25. P. W. Harper and R. E. Flanigan, Investigation of the Variation of Maximum Lift for a Pitching Airplane Model and Comparison with Flight Results, NACA TN 1734 (1948)

26. J. R. Spreiter, G. M. Galster, and W. K. Blair, Effect of Mach and Reynolds Number on the Maximum Lift Coefficient Obtainable in Gradual and Abrupt Stalls of a Pursuit Airplane Equipped with a Low-Drag Wing, NACA RM A5G06, 1945

27. L. E. Ericsson, "Comment on Unsteady Airfoil Stall," Journal of Aircraft, Vol. 4, No. 5, Sep–Oct 1967, pp. 478–480

28. L. S. Shivers, Jr., Effects of Subsonic Mach Number on the Forces and Pressure Distributions on Four NACA 64A-series Airfoil Sections at Angles of Attack as High as 28°, NACA TN 3162 (1954)

29. L. E. Ericsson, Steady and Unsteady Terminal Shock Aerodynamics on Cone-Cylinder Bodies, LMSC L-87-67-2, Contract NAS 8-20354, Sunnyvale, Calif., Oct 1967

30. -----, "Aeroelastic Instability Caused by Slender Payloads," J. Spacecraft and Rockets, Vol. 4, No. 1, Jan 1967, pp. 65–73

31. J. M. McCloud III and G. B. McCullough, Comparison of Calculated and Measured Stall Boundaries of a Helicopter Rotor at Advance Ratios 0.3 to 0.4, NASA TN D-73 (1959)

32. F. O. Carta, "An Analysis of the Stall Flutter Instability of Helicopter Rotor Blades" with comment by N. D. Ham, "Stall Flutter of Helicopter Rotor Blades – A Special Case of the Dynamic Stall Phenomenon," Paper No. 130, Proceedings 23rd Annual National Forum of the American Helicopter Society, Washington, D.C., May 10–12, 1967

33. H. L. Studer, "Experimentelle Untersuchungen Ueber Fleugel Schwingungen," Mitteilungen aus dem Institut fuer Aerodynamik der Technischen Hochschule, Zurich, 1936

34. A. Mendelson, "Aerodynamic Hysteresis as a Factor in Critical Flutter Speed of Compressor Blades at Stalling Conditions," J. Aero. Sci., Vol. 16, No. 11, Nov 1949, pp. 645–652

35. N. D. Ham and M. T. Young, "Torsional Oscillation of Helicopter Blades due to Stall," Journal of Aircraft, Vol. 3, No. 3, May–June 1966, pp. 218–224

36. J. Liiva and F. J. Davenport, "Dynamic Stall of Airfoil Sections for High Speed Rotors," Paper No. 206, Proceedings 24th Annual National Forum of the American Helicopter Society, Washington, D.C., May 8–10, 1968

37. Th. von Karman and W. R. Sears, "Airfoil Theory for Non-Uniform Motion," Aero. Sci., Vol. 5, No. 10 Aug 1938, pp. 379–390

38. H. Multhopp, "Die Berechnung der Auftriebsverteilung von Tragfluegeln," Luftfahrt Forschung, Bd 15, 1938, p. 153

39. N. D. Ham and M. S. Garelick, "Dynamic Stall Considerations in Helicopter Rotors," American Helicopter Society, Journal, Vol. 13, Apr 1968, pp. 49–55

40. T. Sarpakaya, "Separated Unsteady Flow About a Rotating Plate," pp. 1485–1499

41. W. P. Jones, "Research on Unsteady Flow (The Sixth Minta Martin Lecture)," Journal Aero. Sci., Vol. 29, No. 3, Mar 1962, pp. 249–263

42. R. M. Scruggs and A. W. Morris, Axial Stability in Vortices, Research Report ER-9098, Lockheed-Georgia Company, 1968

43. N. D. Ham, "Aerodynamic Loading on a Two-Dimensional Airfoil During Dynamic Stall," AIAA Journal, Vol. 6, No. 10, Oct 1968, pp. 1927–1934

44. W. G. Molyneaux and F. Ruddlesden, A Technique for the Measurement of Pressure Distribution on Oscillating Airfoils with Results for a Rectangular Wing of Aspect Ratio 3.3, Great Britain RAE Struc. TN-164 (1955)

45. J. H. Greidanus, A. I. von de Vooren, and H. Bergh, Experimental Determination of the Aerodynamic Characteristics of an Oscillating Wing with Fixed Axis of Rotation, NLL Report F101 (Jan 1952)

46. L. E. Ericsson, "Effect of Boundary Layer Transition on Vehicle Dynamics," Paper 69-106, AIAA 7th Aerospace Sciences Meeting, New York, N.Y., Jan 20–22, 1969

47. W. Bollay and C. D. Brown, "Some Experimental Results on Wing Flutter," Journal Aero. Sci., Vol. 8, No. 8, June 1941, pp. 313–318

48. H. L. Runyan, D. S. Woolston, and A. G. Rainey, Theoretical and Experimental Investigations of the Effect of Tunnel Walls on an Oscillating Airfoil in Two-Dimensional Subsonic Compressible Flow, NACA TN 3416 (1955)

49. J. Liiva, F. J. Davenport, L. Gray, and I. C. Walton, Two-Dimensional Tests of Airfoils Oscillating Near Stall, USAAVLABS Technical Report 68-13A, Vol. 1, Summary and Evaluation of Results, Apr 1968

Appendix A
NOMENCLATURE

A	nose bluntness parameter, $A = \alpha \Big/ \sqrt{r_n/c}$ (Fig. 8)
AR	aspect ratio, $AR = b^2/S$
A/A_o	amplitude ratio, Eq. (2)
B/B_o	amplitude ratio, Eqs. (7) – (10)
b	wing span, m
C	general aerodynamic coefficient, Eq. (4)
c and $\bar{c}$	reference length, m c = 2-dim. cord length $\bar{c}$ = S/b, mean aerodynamic chord
f	frequncy, CPS
H	total pressure, kg/m^2
h	airfoil camber, m
L	lift, kg: Coefficient $C_L = L \Big/ \left(\rho_\infty U_\infty^2/2\right) S$
l	lift, kg/m: Coefficient $c_l = l \Big/ \left(\rho_\infty U_\infty^2/2\right) c$
M	Mach number
M_p	pitching moment, kg-m: Coefficient $C_m = M_p \Big/ \left(\rho_\infty U_\infty^2/2\right) Sc$
m_p	pitching moment, kg-m/m: Coefficient $c_m = m_p \Big/ \left(\rho_\infty U_\infty^2/2\right) c^2$
N	normal force, kg: Coefficient $C_N = N \Big/ \left(\rho_\infty U_\infty^2/2\right) S$
n	normal force, kg/m: Coefficient $c_n = n \Big/ \left(\rho_\infty U_\infty^2/2\right) c$
p	static pressure, kg/m^2: Coefficient $C_p = (p - p_\infty) \Big/ \left(\rho_\infty U_\infty^2/2\right)$
q	pitch rate, rad/sec
R	radius, m (Fig. 20)
R_c and $R_{\bar{c}}$	Reynolds number based on cord length
R_{r_n}	Reynolds number based on nose radius r_n
R_{eff}	Reynolds number R_c corrected for wind tunnel turbulence

r	radius, m
r_n	nose radius, m
S	reference area, m^2
t	time, sec
U	velocity, m/sec
V	helicopter forward speed, m/sec
x	horizontal coordinate, m
y	airfoil surface height, m (Fig. 7)
z_{CG}	translatory coordinate (Fig. 32)
α	angle of attack, radian or deg
α_o	trim angle of attack, radian or deg (Fig. 32)
α (q)	pitch rate induced angle of attack, radian or deg (Fig. 32)
α ($\dot{z}$)	translation induced angle of attack, radian or deg (Fig. 32)
Δ	increment
ϵ	downwash factor, Eq. (1)
ζ	dimensionless coordinate $\zeta = z_{CG}/c$ (Fig. 32)
θ	angle of attack perturbation, radian or deg (Fig. 32)
ξ	dimensionless x-coordinate, $\xi = x/c$ (Fig. 32)
ξ_o	center of oscillation (Fig. 32)
ρ	air density, kg-sec^2/m^4
σ (q)	pitch rate induced camber angle, radian
Γ	airfoil circulation, m^2/sec (Fig. 30)
τ	dimensionless time, $\tau = t/\frac{c}{U_\infty}$
ν	camber line slope, radian or deg (Fig. 14)
ϕ	phase lag, radian or deg Eq. (2)
$\Delta\phi$	wake lag, radian or deg Eq. (2)
ψ	total phase angle, radian or deg Eqs. (7) – (10)
Ω	helicopter rotor angular velocity, radian/sec (Fig. 20)
ω	oscillation frequency, radian/sec Eqs. (1) – (10)
$\bar{\omega}$	reduced frequency, $\bar{\omega} = \omega\, c/U_\infty$

Subscripts

a	accelerated flow effect
AC	aerodynamic center
CG	center of gravity
e	boundary layer edge conditions
E and eff	effective
LE	leading edge
i	in phase
n	nose
o	out of phase
R	rotor section characteristics
s and stall	stall
TE	trailing edge
tr	boundary layer transition
w	wake lag effect
∞	undisturbed flow
o	oscillation center and trim angle
1, 2	transition induced effects (Fig. 43)

Superscripts

i	induced, e.g., $\Delta^{i}C_{L}$ = separation induced lift
-	delayed pressure gradient giving decreased effective α on "upstroke"
+	delayed pressure gradient giving increased effective α on "downstroke"

Differential Symbols

$$\dot{\theta} = \frac{\partial \theta}{\partial t} \; ; \; \ddot{\zeta} = \frac{\partial^2 \zeta}{\partial t^2}$$

$$C_{L_\alpha} = \frac{\partial C_L}{\partial \alpha} \; ; \; \epsilon_\alpha = \frac{\partial \epsilon}{\partial \alpha}$$

$$C_{m_{\dot{\theta}}} = \frac{\partial C_m}{\partial \frac{c\dot{\theta}}{U_\infty}}$$